UNESCO Chair on Coastal Geo-Hazard Analysis

Research Institute for Earth Sciences
Geological Survey of Iran

unesco Chair

Geological Mapping in the Era of AI: Leveraging Innovation for Precision and Speed

SUTGMM PROGRAMME

Server based Unified Thematic Geological Mapping in Makran

UCCGHA 033

2025

SUTGMM PROGRAMME

Server based Unified Thematic Geological Mapping in Makran

Geological Mapping in the Era of AI: Leveraging Innovation for Precision and Speed!

سرشناسه : نظری، حمید، ۱۳۴۶-
-Nazari, Hamid, 1968
عنوان و نام پدیدآور : Geological Mapping in the Era of Al: Leveraging Innovation for Precision and Speed! [Book] / author Hamid Nazari...[et al.]; employer Research Institute for Earth Sciences; supervisors Hamid Nazari; summarized and translated in to English Aram Fathian Baneh; with cooperation UNESCO Chair on Coastal Geo-Hazard Analysis.
مشخصات نشر : تهران: نشر خزه، ۱۴۰۳= ۲۰۲۵م.
مشخصات ظاهری : ۱۶۴ص.؛ ۱۴ × ۲۱ س‌م.
شابک : 978-622-8423-35-7
وضعیت فهرست نویسی : فیپا
یادداشت : زبان: انگلیسی.
یادداشت : author Hamid Nazari, Jalal Karami, Saied Arefipour, Aram Fathian.
یادداشت : عنوان به فارسی: نقشه‌برداری زمین‌شناسی در عصر هوش مصنوعی: استفاده از نوآوری برای دقت و سرعت
موضوع : زمین‌شناسی -- نقشه‌ها – سرورپایه – هوش مصنوعی
موضوع : Geology -- Maps -- Server Base -- Artificial intelligence
شناسه افزوده : نظری، حمید، ۱۳۴۶-
شناسه افزوده : Nazari, Hamid, 1968-
شناسه افزوده : کرمی، جلال، ۱۳۵۱-
شناسه افزوده : Karami, Jalal, 1972-
شناسه افزوده : عارفی‌پور، سعید، ۱۳۵۸ -
شناسه افزوده : Arefipour, Saied, 1979-
شناسه افزوده : فتحیان، آرام، ۱۳۶۲-
شناسه افزوده : Fathian, Aram, 1983-
شناسه افزوده : پژوهشکده علوم زمین، سازمان زمین‌شناسی و اکتشافات معدنی کشور، دانشگاه تربیت مدرس
شناسه افزوده : Research Institute of Earth Sciences, Geological Survey of Iran, Tariat Modares University
شناسه افزوده : کرسی یونسکو در مخاطرات زمین شناختی ساحلی
شناسه افزوده : UNESCO Chair on Coastal Geo-Hazard Analysis
رده بندی کنگره : QE۳۶
رده بندی دیویی : ۲۲۳/۵۵۰
شماره کتابشناسی ملی : ۹۹۱۸۹۰۹

Geological Mapping in the Era of AI: Leveraging Innovation for Precision and Speed!

Author:

Hamid Nazari, Jalal Karami

Saied Arefipour, Aram Fathian

نشر خزه

اطلاعات گزارش

عنوان: نقشه‌برداری زمین‌شناسی در عصر هوش مصنوعی: استفاده از نوآوری برای دقت و سرعت

مجری: پژوهشکده علوم زمین!

زبان مرجع: فارسی - انگلیسی

خروجی: گزارش، نقشه، مقاله، داده های الکترونیکی

ناظران علمی: حمید نظری

نویسندگان: حمید نظری، جلال کرمی، سعید عارفی پور، آرام فتحیان بانه

رئیس کرسی یونسکو در مخاطرات زمین شناختی ساحلی: حمید نظری

مسئول شورای اجرایی: راضیه لک

خلاصه‌نویسی و ترجمه به انگلیسی: آرام فتحیان بانه

ناشر: نشر خزه

با همکاری کرسی یونسکو در مخاطرات زمین شناختی ساحلی

چاپ اول: ۱۴۰۳

شمارگان: ۵۰ نسخه

صفحات: ۱۶۴

شابک: ۹۷۸-۶۲۲-۸۴۲۳-۳۵-۷

khazepub@gmail.com

Report Information

Title: Geological Mapping in the Era of Al: Leveraging Innovation for Precision and Speed!

Employer: Research Institute for Earth Sciences

Original language: Persian - English

Output: Report, Map, Paper, Digital Meta Data

Supervisors: Hamid Nazari

Authors: Hamid Nazari, Jalal Karami, Saied Arefipour, Aram Fathian Baneh

Chairholder in the UNESCO Chair on Coastal Geo-Hazard Analysis: Hamid Nazari

Head of the Executive Council: Razyeh Lak

Summarized and translated into English: Aram Fathian Baneh

Publisher: Khazeh Publication

with cooperation UNESCO Chair on Coastal Geo-Hazard Analysis

First Edition: 2025

Edition number: 50

Page: 164

Shabak: 978-622-8423-35-7

khazepub@gmail.com

Scientific Council	
Name	**Affiliation**
Behrouz Abtahi	Shahid Beheshti University (SBU)
Philippe Agard	University of Sorbonne
Justin Ahanhanzo	Intergovernmental Oceanographic Commission of UNESCO (IOC-UNESCO)
Hamid Alizadeh Lahijani	Iranian National Institute for Oceanography and Atmospheric Science
Ryo Anma	Tokushima University
Franck A. Audemard	Department of Geology, Central University of Venezuela
Alice Aurelie	UNESCO Water Sciences Division
Ara Avagyan	IGS: Institute Geological Sciences
Yeong Bae Seong	Korea University
Rick J Bailey	IOC-UNESCO Indian Ocean Tsunami Warning and Mitigation System/ UNESCO
Abbas Banj Shafiei	Urmia University
Eric Barrier	University of Sorbonne
Yahya Djamour	Shahid Beheshti University (SBU)
Issa El-Hussain	Sultan Qaboos University
Aram Fathian Baneh	University of Calgary

Hassan Fazeli Nashli	University of Tehran
Magdi Guirguis	Institut français d'archéologie orientale du Caire
Martin Hanz	German under water archaeology association
Ekkehard Holzbecher	German University of Technology in Oman
Egor Krasinskiy	Underwater research center Russian Geographical Society
Razyeh Lak	Research Institute for Earth Sciences
John Lambert	Deltares, UNESCO
Mohammad Mokhtari	International Institute of Earthquake Engineering and Seismology
Hamid Nazari	Research Institute for Earth Sciences
Jafar Omrani	Geological Survey of Iran
Klaus Reicherter	Aachen University
Jean-François Ritz	University of Montpellier
Stefano Salvi	National Institute of Geophysics and Volcanology (INGV)
Morteza Talebian	Research Institute for Earth Sciences
Mohammad Tatar	International Institute of Earthquake Engineering and Seismology

Judith Thomalsky	German Archaeological Institute Tehran Branch
Richard Walker	University of Oxford
Wenjiao Xiao	Chinese Academy of Sciences
Alireza Zarasvandi	Iranian Research Organization for Science & Technology (IROST) – Ministry of Science, Research & Technology
Mahdi Zare	International Institute of Earthquake Engineering and Seismology
Executive Committee	
Name	**Affiliation**
Nasir Ahmadi	Environmental Protection Organization of Mazandaran Province
Arash Amini	Golestan University
Alireza Amrikazemi	Scientific Coordinator, Qeshm Island UNESCO Global Geopark
Parviz Armani	Imam Khomeini International University
Ataollah Dadashpour	Geological Survey of Iran, Sari branch
Asghar Dolati	Kharazmi University
Hasan Fazelinashli	**University of Tehran**
Fahimeh Foroghi	Iranian National Institute for Oceanography and Atmospheric Science

Abdolazaim Ghanghormeh	Golestan University
Habibolah Ghasemi	Shahrood University of Technology
Mohammad reza Ghasemi	Research Institute for Earth Sciences
Manouchehr Ghorashi	Research Institute for Earth Sciences
Ahmed Hadidi	German University of Technology in Oman (GUTECH)
Jafar Hassanpour	**University of Tehran**
Ataollah Kavian	Environmental Protection Organization of Mazandaran Province
Razyeh Lak	Head of RIES and Executive Manager
Mahmoudreza Majidifard	Research Institute for Earth Sciences
Majid Moghadam	Iranian Research Organization for Science & Technology (IROST)
Ali Akbar Momeni	Shahrood University of Technology
Babak Moradi	Iranian National Institute for Oceanography and Atmospheric Science
Seyed Mohsen Mortazavi	**Hormozgan University**
Hasan Nasrollah Zadeh	Caspian Sea Ecological Research Center
Ehsan Pegah	Kharazmi University
Abdolwahed Pehpouri	Qeshm Island UNESCO Global Geopark

Ahmadreza Rabani	University of Science and Technology of Mazandaran
Mahdi Rahmanian	Shargh Daily newspaper
Ahmad Rashidi	**International Institute of Earthquake Engineering and Seismology**
Masoud Sadri Nasab	**University of Tehran**
Mohammad Tatar	**International Institute of Earthquake Engineering and Seismology**
Alireza Vaezi	*Research Institute for Earth Sciences*
Mojtaba Yamani	**University of Tehran**
Secretariat	
Name	**Affiliation**
Elnaz Aghaali	Research Institute for Earth Sciences
Keivan Ajdari	Research Institute for Earth Sciences
Hourieh AliBeygi	Research Institute for Earth Sciences
Bahman Bahrami	Memaran Asr Ertebat Company
Hanieh Bakhshaei	Geological Survey of Iran
Reza Behbahani	Geological Survey of Iran
Javad Darvishi khatooni	Geological Survey of Iran
Mohammadreza Ensani	Geological Survey of Iran
Marziyeh Estrabi Ashtiyani	Geological Survey of Iran

Sedigheh Ghanipour	Research Institute for Earth Sciences
Elaheh Ghayoumi	Memaran Asr Ertebat Company
Gholamreza Hoseinyar	Geological Survey of Iran
Mojtaba Kavianpour Sangno	Geological Survey of Iran
Zeinab Kazeminia	Research Institute for Earth Sciences
Hamoon Memarian	Research Institute for Earth Sciences
Mehrnoosh Pour Saeid	Graphic Designer
Shirin Safavi	Research Institute for Earth Sciences
Aazam Takhtchin	Research Institute for Earth Sciences

SUTGMM PROGRAMME

Server based Unified Thematic Geological Mapping in Makran

Geological Mapping in the Era of AI:

Leveraging Innovation for Precision and Speed

January 2025

Geological Mapping in the Era of AI:
Leveraging Innovation for Precision and Speed

Geology by: *H. Nazari, S. Arefipour, and M. Fonoudi*

Structural balanced sections by: *H. Nazari and S. Arefipour*

Petrography by: *Gh. Hoseinyar*

Remote sensing and machine learning by: *J. Karami, S. and Arefipour*

Paleontology by: *J. Daneshian and M. R. Partoazar*

Final report and editing by: *A. Fathian*

Executive supervisors: *A. Zarasvandi and M. Moghadam*

Supervisor in chief: *H. Nazari*

GeoNexus

January 2025

Research Institute for Earth Sciences

UNESCO Chair on Coastal Geo-Hazards Analysis

SUTGMM PROGRAMME

Server based Unified Thematic Geological Mapping in Makran

UNESCO Chair on Coastal Geo-Hazard Analysis

Research Institute for Earth Sciences Geological Survey of Iran

unesco Chair

IGM

Datum

Server-Based Unified Thematic Geological Mapping of Makran (SUTGMM) employs the WGS 1984 datum for accurate georeferencing. The map projection used is the Universal Transverse Mercator (UTM), specifically UTM Zone 41N, which ensures precise positioning within the region. The map is provided at a scale of 1:50,000, referenced to Sheet No. 8141-4, ensuring consistency and accuracy in the spatial representation of geological features.

Abstract

The Server-Based Unified Thematic Geological Mapping of Makran (SUTGMM) is a comprehensive geospatial study conducted at a scale of 1:50,000, focusing on the Makran region, located in southeastern Iran along the northern margin of the Oman Sea. This region is characterized by diverse geological formations resulting from the collision of the Arabian and Eurasian plates, including volcanic and sedimentary sequences, turbidite basins, and Quaternary deposits. Makran's rich geological heritage, coupled with its historical importance, makes it a prime subject for advanced geoscientific research and mapping.

The SUTGMM project (Sheet No. 8141-4) aims to prepare detailed geological maps for the area covered by four previously published 1:100,000 geological sheets: Chabahar, Pir Sohrab, Konarak, and Kahir. Additionally, the project includes nine 1:50,000 geological sheets: Ab Sard, Chabahar, Gor, Gurdim, Kahir, Konarak, Kuh-e-kand Koruch, Park Bala, and Zirdan. A buffer zone ranging from 13 to 28 km has also been defined around the core area to facilitate better analysis of geological features that extend beyond the sheets. These maps integrate data from multiple remote sensing sources such as Sentinel-1, Sentinel-2, Landsat 8, and ASTER, as well as digital elevation models (DEMs) to capture spectral, geological, and topographical information at various resolutions.

Utilizing a novel approach combining cloud computing, machine learning, and object-based image analysis, the project leverages the power of *Google Earth Engine* for the processing and analysis of large datasets. The random forest algorithm, used for geological classification, has enabled the creation of a unified geological map with an accuracy of 85%, highlighting the effectiveness of this integrated approach.

This project has provided valuable insights into the complex geological context of the Makran region. The geological units mapped in SUTGMM represent a time range from the Oligocene to the Quaternary period. This includes older formations from the Oligocene and Miocene, as well as

more recent Pleistocene and Quaternary deposits. The units highlight the region's complex geodynamic evolution, influenced by both tectonic activity and sedimentary processes.

The GeoNexus geodatabase, as the final product of the SUTGMM project, represents a major advancement in geological mapping by using cloud computing, machine learning, field surveys, and multi-source data integration to enhance the accuracy, efficiency, and comprehensiveness of geological outputs. Ultimately, the findings from this study are expected to support sustainable development efforts and foster a deeper understanding of the Makran region's geodynamic processes.

Acknowledgment

We would like to express our deepest gratitude to Kor, Rezaie and Afarin from Iranian National Institute for Oceanography and Atmospheric Science, Chabahar Campus for their invaluable support and logistical assistance during the course of this project. Their contributions were instrumental in ensuring the success of our field operations.

We are also grateful to R. Mohtashamipour, R. Lak and M. Majidifar for their support that significantly advanced our project.

This project has been enriched by the cooperation of many individuals and institutions, and we sincerely appreciate their support.

Contents

List of Figures

List of Tables

1 Introduction

1.1 Historical and Geographical Context

Makran, a region with profound historical and geographical significance, spans the southeast of Iran and southwest of Pakistan. This area, defined by its characteristic east-west mountains and bordered by the Strait of Hormuz and the port of Karachi, is known both for its rugged terrain and strategic maritime significance. Historically, Makran derives its name from an ancient state, documented to have existed over 3000 years ago. This state extended from Kerman to the Mehran River along the Oman Sea, encompassing an area once under the rule of the Achaemenid Empire as its fourteenth state during the 6th century BC (Kent, 1953; Mayrhofer, 1978; Schmitt, 1991).

The stone inscriptions found in Bisotun and Persepolis refer to this ancient state, historically named Mecca, highlighting its significance during the era of Achaemenid rule. Notably, Makran played a pivotal role during Alexander the Great's return from India in 324–325 BC. Historical accounts suggest that as Alexander led his forces through the Makran desert towards Pura (present-day Iran), he encountered severe challenges including extreme conditions that led to significant losses among his troops due to fatigue, thirst, and malnutrition.

The growing wedge of Makran is characterized by its sparse population and predominantly nomadic lifestyle, juxtaposed against a backdrop of increasing urban development along the Oman Sea coast. This unique blend of historical richness and modern evolution presents a compelling area of study for geological and environmental research.

1.2 Scope and Data Collection

The focus of this report is the Server-based Unified Thematic Geological Mapping of the Makran (SUTGMM), conducted at a detailed scale of 1:50,000. The project aims to delineate and understand the complex geological framework and environmental dynamics of the region through comprehensive data collection and analysis.

The methodology employed in this project involves an extensive compilation of various data sources. These include high-resolution satellite images, existing topographical and geological maps, peer-reviewed articles, theses, and other scholarly publications, all of which have been accessed through open sources. The collected data were meticulously classified, ranked, and integrated into various informational layers crucial for the mapping project.

A specialized location database was developed to house all georeferenced data extracted from the compiled sources. This database includes detailed records of sample points, dating data, field measurement locales, and earthquake event data. It is important to note that while the primary data collection focused on the mapped area, relevant information from adjacent regions was also gathered to ensure a holistic understanding of the broader geological features.

Prior to the commencement of field investigations, extensive digital mapping of faults and geological structures was conducted to prepare for the detailed field assessments. The preparatory geodatabase comprises over 520 distinct points and linear features, all carefully georeferenced to enhance the accuracy and utility of the geological maps being produced.

The mapping of Makran not only serves to enrich our understanding of its complex geological context but also aids in assessing the region's natural resources, potential geohazards, and environmental challenges. The insights gained through this project are expected to inform future developmental planning and conservation efforts, ensuring that the region's growth is sustainable and cognizant of its rich historical and geological heritage.

This initiative underscores the importance of integrating historical data with contemporary scientific research to foster a holistic understanding of geologically significant regions like Makran. Through the meticulous gathering and analysis of geospatial and geological data, this project contributes significantly to our knowledge of the earth's dynamic processes in one of the world's most historically rich regions.

In the dynamic landscape of Earth sciences development, a pioneering project was defined from the perspective of knowledge and technology in the Makran region. This innovative endeavor, which sits at the intersection of cloud computing, machine learning, artificial intelligence, and remote sensing, marks a significant leap in the ability to understand and map a geologically complex area. The Makran region, part of the Sistan and Baluchestan province, presents a geological collection with diverse trends and geological periods. This area, shaped by the ongoing collision of the Arabian and Eurasian plates, includes a diverse array of geological formations, ranging from ophiolite sequences and turbidite basins to Quaternary sediments. While this complexity offers a treasure trove for geological study, it has long posed significant challenges to traditional mapping methods.

With the advent of cloud computing, big data analysis, and the rapid development of cloud infrastructures, a new era of distributed data processing has begun. The rise and development of cloud computing in spatial science fields, such as the *Google Earth Engine* processing system, have revolutionized the accessibility, processing, and analysis of remote sensing data. This case study represented an ambitious project aimed at demonstrating the power of *Google Earth Engine* in object-based image processing and machine learning techniques. The goal of this project was to create a unified, high-precision geological map of the Makran region, capturing the intricate details of the region's geological landscape.

1.3 Objectives

The objective of this project is to prepare an integrated geological map using cloud computing and machine learning for an area covered by the

four 1:100,000 geological sheets of Chabahar, Pir Soharab, Konarak, and Kahir (Figure 1-1). This will be achieved by utilizing various and diverse remote sensing images—including Sentinel-1, Sentinel-2, Landsat 8 (OLI), ASTER emissivity images—and digital elevation data (DEM, Aspect, Slope, and Hillshade) within a cloud environment and cloud computing platforms.

In this plan, a completely different approach will be adopted: instead of using one or two images, an attempt will be made to utilize a diverse archive of existing images as mentioned above. Additionally, thanks to the processing capabilities of supercomputers available on *Google Earth Engine* servers, all processing will be carried out in this cloud environment. Among other significant differences of this project compared to other mapping studies will be the use of various advanced image processing and data mining algorithms, such as mathematical transformations and machine learning on data and images, which largely eliminates errors resulting from traditional mapping methods.

1.4 Data Sources and Accessibility

The thematic geological mapping of Makran has been conducted exclusively with unclassified, publicly available data. This approach ensures transparency and broad accessibility, making it a valuable resource for academic researchers, policymakers, and the general public interested in the geological characteristics of Makran. The reliance on freely available data also highlights the project's commitment to utilizing open-source information to foster a collaborative and inclusive research environment. This approach aligns with global scientific standards for data sharing and accessibility, ensuring that the findings and insights from this project contribute to the collective understanding of regional geology without the constraints of classified or proprietary data barriers.

In alignment with the project's objectives, previous geological maps used within this study undergo a meticulous process of georeferencing to ensure accuracy and reliability across various information layers. These maps, once processed, will be publicly accessible, contributing to the

body of open-access resources available to the scientific and public community. This deliberate approach not only supports the study's comprehensive bibliographic compilation but also leverages digitized data and previously published reports. By doing so, the project enhances the robustness of its research framework and facilitates a deeper understanding of the geological intricacies of the Makran region.

The compilation of geological data for this project is grounded in the systematic use of both previous and current maps and reports. These data, essential for the thorough analysis and scope of our study, encompass various information layers, each tailored to specific aspects of the geological features under investigation. By integrating these layers, we achieve a multidimensional understanding of the geological and structural complexities of the area.

1.4.1 Unlocking Trapped Data

Geological maps provide invaluable insights into the surface conditions and composition of different regions. For this project, maps published by the Geological Survey of Iran serve as the primary sources. These maps have been meticulously georeferenced, ensuring precise alignment of the data, which enhances their utility in digital GIS platforms. The georeferencing process not only facilitates the overlay and integration with other spatial data but also improves the accuracy of our geological interpretations.

Each map is categorized by its distinct type—primarily Geological Quadrangle Maps—which detail the geological boundaries, fault lines, and lithographic characteristics of the study area. These maps are published at scales conducive to detailed analysis, typically at 1:250,000 for broad regional assessments and 1:100,000 for more focused, local studies. This scale diversity is critical, allowing us to tailor our investigations to the appropriate geographic extents and resolutions necessary for detailed field studies versus broader regional planning and analysis.

1.4.2 Contribution to the Bibliography and Digital Resources

The digitized data from these maps significantly contribute to our project's bibliography, providing a foundation upon which further studies and reports are built. The conversion of these analog maps into digital formats makes them accessible for modern geospatial analyses, and remote sensing integration. Table 1-1 lists the maps used in this project, illustrating the range and depth of the resources employed.

Each map entry includes crucial details such as the type of map, publication date, scale, and specific features highlighted (e.g., folds, faults), underscoring the rich geological diversity and complexity of the regions studied. This detailed cataloging ensures that all data sources are accurately attributed and readily available for review and further research, adhering to scientific rigor and integrity in the documentation.

By leveraging these comprehensive and meticulously prepared sources, our project stands on a robust platform of verified data, enhancing both the credibility and reliability of our geological assessments.

Table 1-1. List of the maps used in the project.

Publisher	Date	Map Type	No.	Title	Scale	Unlocking Data
Geological Survey of Iran	1983	Geological Quadrangle Map of Iran	M14	Pishin	1:250,000	Map
Geological Survey of Iran	1983	Geological Quadrangle Map of Iran	M13	Saravan	1:250,000	Map
Geological Survey of Iran	1983	Geological Quadrangle Map of Iran	K14	Fannuj	1:250,000	Map
Geological Survey of Iran	1989	Geological Quadrangle Map of Iran	L14	Nikshahr	1:250,000	Map
Geological Survey of Iran	1994	Geological Quadrangle Map of Iran	8041	Kahir	1:100,000	Fold, Fault, Legend, etc.
Geological Survey of Iran	1995	Geological Quadrangle Map of Iran	8042	Nik Shahr	1:100,000	Map
Geological Survey of Iran	1996	Geological Quadrangle Map of Iran	8140	Chabahar	1:100,000	Fold, Fault, Legend, etc.
Geological Survey of Iran	2004	Geological Quadrangle Map of Iran	8142	Qasr-e-Qand	1:100,000	Map
Geological Survey of Iran	2004	Geological Quadrangle Map of Iran	8141	Pirsohrab	1:100,000	Fold, Fault, Legend, etc.

1.5 Study Area and Area of Interest (AOI)

The goal of this project was to prepare a geological map for an area covered by the four 1:100,000 geological sheets of Chabahar, Pir Soharab, Konarak, and Kahir (Figure 1-1). An additional buffer zone of approximately 13 to 28 km was defined around the AOI (Figure 1-2). This buffer was included for two reasons:

1. Better analysis and interpretation: to analyze and interpret geological trends that sometimes extend beyond the boundaries of the sheets.
2. Integrated mapping: to prepare unified maps of the rock units within these sheets and their surrounding areas.

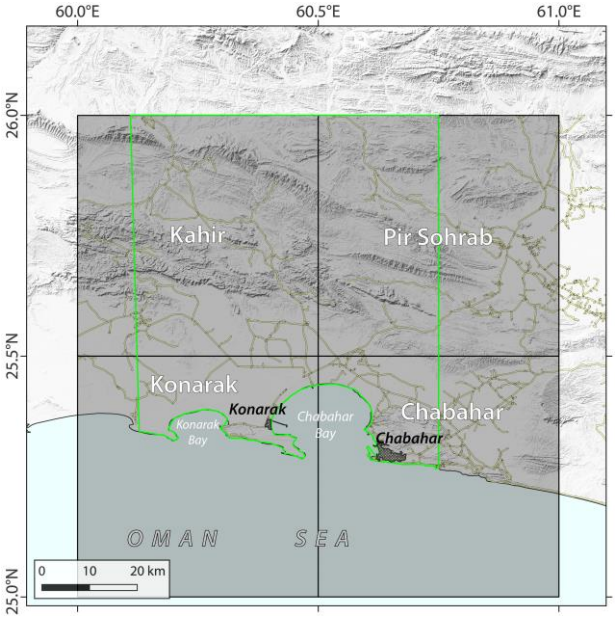

Figure 1-1. The Area of Interest (AOI) for the SUTGMM highlighted with a green polygon. Dark shaded rectangles indicate the four 1:100,000 geological sheets of Kahir, Pir Sohrab, Konarak and Chabahar.

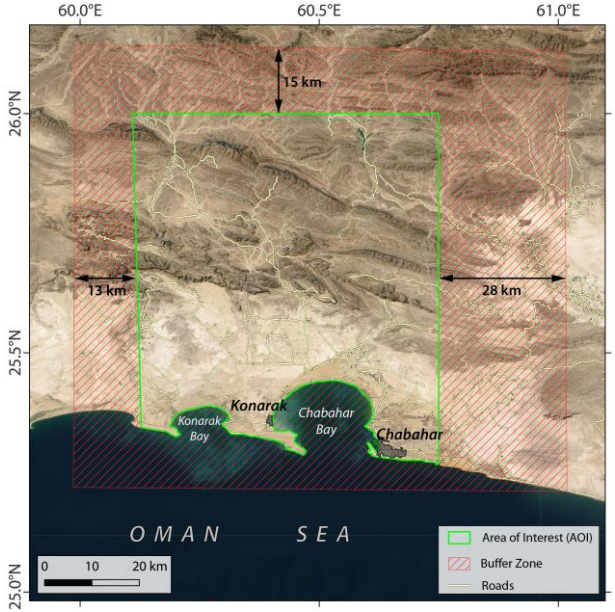

Figure 1-2. Study area encompassing the area of interest (AOI) and the additional buffer zone.

2 Geological and Tectonic Setting

The tectonic setting of the Makran region has significant implications for understanding the broader geodynamic evolution of the Middle East and the closure of the Neo-Tethys Ocean. The northward subduction of the Arabian Plate beneath Eurasia contrasts with the continental collision in the Zagros Mountains to the west, highlighting the complex tectonic interactions along the plate boundary (Burg, 2018). The presence of Cretaceous and Quaternary volcanic arcs indicates a long history of subduction-related magmatism. The eroded or subducted remnants of older arcs provide insights into the tectonic evolution and fragmentation of the upper plate (Arthurton et al., 1982; Burg, 2018).

The recognition of Jurassic rift-related magmatism and Cretaceous arc magmatism suggests that the Central Iran block underwent significant fragmentation prior to the main collisional events, affecting reconstructions of the orogenic belt (Burg, 2018). The tectonic history of the Makran region can be correlated with that of the Oman Mountains on the subducting Arabian Plate, providing a more comprehensive understanding of regional tectonics (Burg, 2018).

The Makran region exemplifies a complex and evolving tectonic setting (Figure 2-1) shaped by the interplay of subduction, accretion, seismicity, uplift, and sedimentation. The shallow subduction of the Arabian Plate beneath Eurasia has led to the development of one of the world's largest accretionary wedges, characterized by significant sediment accumulation, complex structural deformation, and varied seismic behavior. Understanding the tectonic setting of Makran is crucial for assessing seismic hazards, reconstructing regional geodynamic evolution, and exploring the interactions between tectonics and surface processes. Ongoing research and integration of geological, geophysical, and

geomorphological data continue to enhance our knowledge of this dynamic region.

2.1 Tectonic Setting of Makran

The Makran region, located in southeastern Iran and southwestern Pakistan along the northern margin of the Gulf of Oman, is a geologically complex area characterized by an extensive accretionary wedge formed due to the northward subduction of the Arabian Plate beneath the Eurasian Plate (Figure 2-1 and Figure 2-2). This accretionary wedge, known as the Makran accretionary wedge, extends approximately 1,000 km along strike and is bounded by significant fault systems to the east and west (Arthurton et al., 1982; McCall, 1985; Dolati, 2010; Haghipour and Burg, 2014; Gharibreza, 2016; Burg, 2018).

Geodetic measurements and tectonic reconstructions reveal that the Arabian Plate is actively converging with the Eurasian Plate at rates varying along the strike of the Makran subduction zone (Figure 2-2). Measurements between Muscat in Oman and Chabahar on the Iranian coast indicate a convergence rate of approximately 19 mm/yr (Vernant et al., 2004; Khorrami et al., 2019). This convergence is part of the larger-scale motion of the Arabian Plate as it moves northward, subducting beneath the Eurasian Plate along the Makran Trench (Figure 2-2).

Further geodetic data show that the present-day convergence rate between the Makran coast (e.g., Chabahar GPS station) and stable Eurasia is about 8 mm/yr (Vernant et al., 2004). However, other studies suggest that the convergence rates increase eastward, reaching up to 35.5–42 mm/yr in eastern Makran due to the anticlockwise rotation of the Arabian Plate relative to Eurasia (DeMets et al., 2010; Hatzfeld and Molnar, 2010; Burg, 2018).

The variation in convergence rates along the subduction zone has significant implications for the tectonic evolution and seismicity of the region. The increasing convergence rates from west to east are consistent with the anticlockwise rotation of the Arabian Plate and are corroborated

by seafloor spreading rates and fault azimuths for the major plates involved (DeMets et al., 2010).

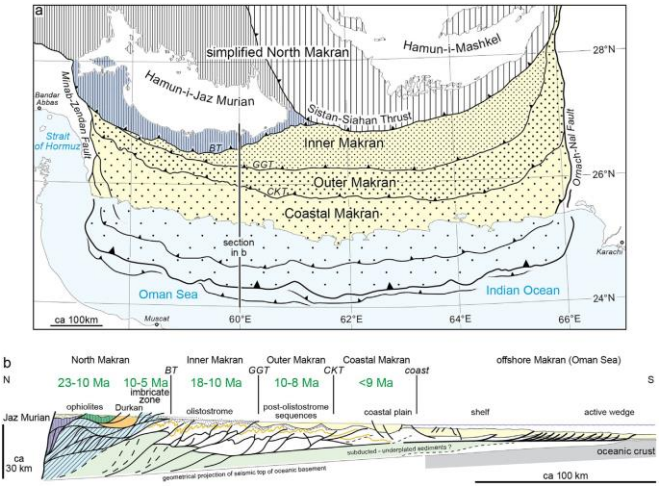

Figure 2-1. Tectonic setting of the Makran region, showing tectonostratigraphic zones and major structures, including the accretionary wedges and pull-apart basins (Haghipour and Burg, 2014; Burg, 2018).

The Makran accretionary wedge is bounded by two major fault systems that play crucial roles in its tectonic configuration (Figure 2-1 and Figure 2-2). To the west lies the dextral (right-lateral) Minab–Zendan Fault System. Specifically, the Minab Fault separates the Makran subduction zone from the Zagros continent-continent collision zone (Stöcklin, 1968; Bird et al., 1975; Dolati, 2010; Haghipour and Burg, 2014). This fault system accommodates the differential motion between the converging plates and acts as a structural boundary between distinct tectonic regimes.

To the east, the sinistral (left-lateral) Chaman–Ornach–Nal Fault System and its offshore continuation, the Owen Fracture Zone, separate Makran and the Arabian Plate from the Indian subcontinent (Figure 2-2). The Indian Plate moves northward at a rate of 40–50 mm/yr relative to Eurasia, significantly faster than the convergence rate along the Makran

subduction zone (Paul et al., 2001; Molnar and Stock, 2009; Dolati, 2010; Haghipour and Burg, 2014; Burg, 2018).

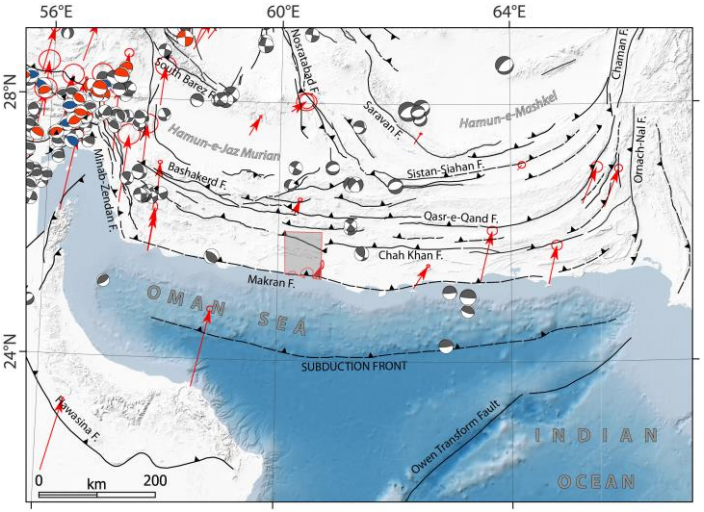

Figure 2-2. Seismotectonic configuration of Makran and surrounding areas. The subduction front in the Oman Sea marks the convergence between the Arabian and Eurasian plates. Fault traces are compiled and modified after Fathian (2022). Red shaded polygon mark the AOI. Grey, red, and blue beachballs represent fault plane solutions from the the Global Centroid Moment Tensor (GCMT; https://www.globalcmt.org), body waveform, and the first motions catalogs (see Fathian, 2022 and the references therein). Red arrows represent GPS velocity vectors relative to a stable Eurasian plate (Khorrami et al., 2019). Background is the shaded relief from SRTM 90m (Farr et al., 2007) and GEBCO Global Bathymetry 15 arc-sec (GEBCO Compilation Group, 2023) visualizing surface topography and bathymetry.

Within the Makran region, the structural configuration is further complicated by several parallel accretionary wedges and pull-apart basins (e.g., Haghipour and Burg, 2014; Gharibreza, 2016). The Coastal Makran forms the onshore part of the accretionary wedge, comprising deformed Cenozoic terrigenous and mud sediments (Figure 2-1). Seaward of the Coastal Makran lies the Outer Makran, characterized by active sediment accretion and deformation. Further inland, the Inner Makran and North Makran represent more distal parts of the accretionary wedge, with complex sedimentary and structural histories (Figure 2-1b). Inner Makran

consists of a thick sequence of upper Eocene to lower Miocene turbidites showing a general thickening- and coarsening-upward trend (e.g., Dolati, 2010; Haghipour and Burg, 2014). North Makran comprises tectonically imbricated upper Cretaceous to Eocene igneous rocks, ophiolites, and associated deep marine sediments (McCall, 1983; Haghipour and Burg, 2014). Additionally, Hamun-e-Jaz Murian and Hamun-e-Mashkel (Figure 2-2) are significant depressions (pull-apart basins) interpreted as forearc basins (Farhoudi and Karig, 1977; Dolati, 2010; Haghipour and Burg, 2014).

The northern boundary of the Makran is delimited by the Quaternary cover of the Jaz Murian depression in Iran and the equivalent Mashkel depression in Pakistan (Burg, 2018). These structural features contribute to the complex tectonic setting and influence sedimentation patterns, seismicity, and surface deformation.

2.1.1 Subduction Characteristics and Volcanic Arcs

The subduction of the oceanic lithosphere of the Arabian Plate beneath the Iranian Lut Block and the Afghan/Helmand Block (Figure 2-3) has been ongoing since the late Cretaceous (Stoneley, 1974; Jacob et al., 1979; McCall and Kidd, 1982; Arthurton et al., 1982; Berberian et al., 1982; Dercourt et al., 1986; Burg, 2018). The initiation of subduction is evidenced by the age of the Makran volcanic arcs, such as Bazman in Iran and the Chagai Hills in Pakistan (Figure 2-3), which date back to the late Cretaceous (Arthurton et al., 1982; Berberian et al., 1982).

The Quaternary Baluchistan volcanic arc, extending from north of the Chagai Hills at the Pakistan–Afghanistan border into southeastern Iran, is associated with the ongoing subduction along the Makran zone (Jacob et al., 1979; Berberian et al., 1982; Dolati, 2010). This volcanic arc comprises three major volcanic centers: Bazman, Taftan, and Koh-i-Sultan. Bazman and Taftan are significant volcanic centers located in southeastern Iran, contributing to the volcanic activity along the arc. Koh-i-Sultan, situated near the Pakistan–Afghanistan border, completes the approximately 300-km-long belt of volcanic centers (Jacob et al., 1979; Berberian et al.,

1982). The presence of these volcanic centers indicates active magmatism associated with the subduction process.

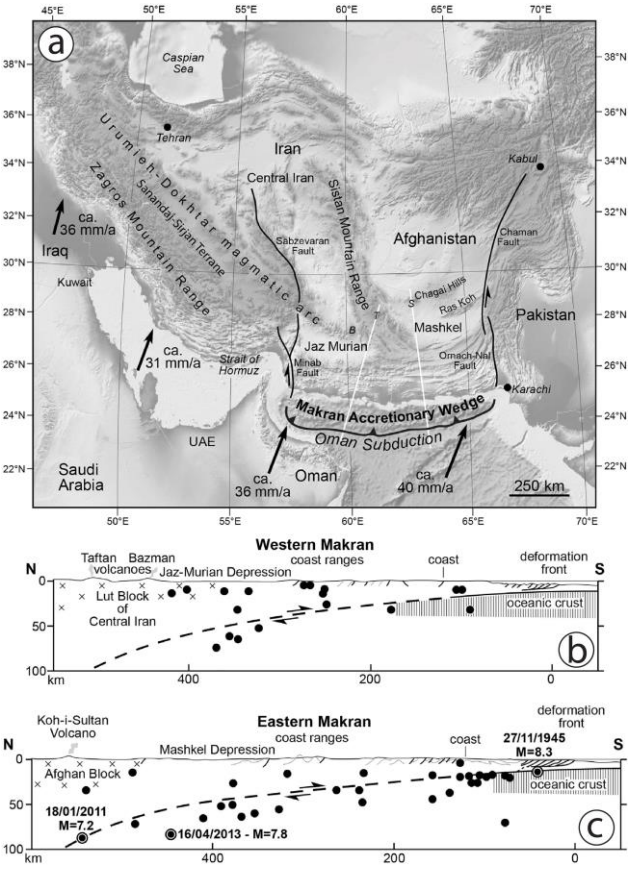

Figure 2-3. a) Regional overview of the Makran accretionary wedge and surrounding tectonic features (Burg, 2018). Italic B, T, and S represent the Bazman, Taftan, and Koh-i-Sultan volcanoes, respectively. White lines represent the locations of cross-sections shown in panels b and c. b, c) Lithospheric-scale cross-sections across the Western (b) and Eastern (c) Makran. These cross sections illustrate the primary geological structures and seismicity, with solid black circles representing focal mechanisms for seismic events, modified after Byrne et al. (1992) and updated with magnitude M4 events up to the present (Burg, 2018).

A notable feature of the Makran subduction zone is the relatively large gap of 400–600 km between the trench and the volcanic arc. This unusually wide accretionary wedge suggests that the subducting plate dips at a very shallow angle of about 1–2 degrees to the north (e.g., Dolati, 2010). This shallow subduction angle is supported by several lines of evidence. Seismic reflection and refraction studies indicate a gently dipping subducting slab beneath the Makran region (e.g., White and Klitgord, 1976; White and Louden, 1982). Analyses of earthquake hypocenters and focal mechanisms show that seismicity is concentrated at shallow depths, consistent with a shallow subduction angle (Figure 2-3b, c) (Jacob et al., 1979; Byrne et al., 1992; Engdahl et al., 2006; Alinaghi et al., 2007). Additionally, tomographic imaging reveals a shallow slab beneath the Eurasian continent (Figure 2-4), further confirming the low-angle subduction (Bijwaard et al., 1998; Hafkenscheid et al., 2006). The shallow subduction geometry has significant implications for the tectonic evolution, sediment accretion, and seismic behavior of the Makran region.

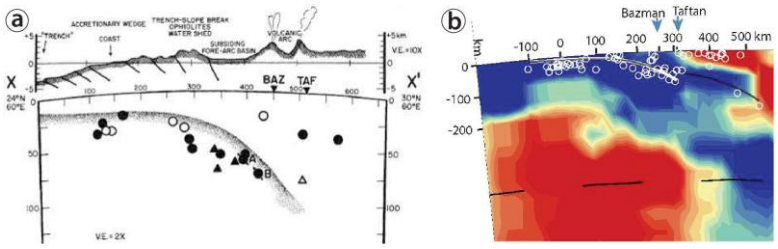

Figure 2-4. a) N–S section across Western Makran (60°E) showing the subduction of the Arabian plate beneath the Eurasian plate, with seismic events projected along the profile, highlighting the steepening subduction slope beneath the Jaz Murian depression (Jacob et al., 1979). b) Seismic tomography (Hafkenscheid et al., 2006) and earthquakes with the subducting slab beneath the Makran region (Dolati, 2010).

2.1.2 Accretionary Wedge

The Makran accretionary wedge is one of the largest in the world, characterized by significant sediment supply from the Indus and other river systems, as well as the shallow subduction angle. It is approximately 300–350 km wide from the submarine deformation front to the Hamun-

e-Jaz Murian and Hamun-e-Mashkel depressions (Haghipour and Burg, 2014). The wedge is divided into two main parts. The active submarine wedge, a 100–150-km-wide zone located offshore, is where active sediment accretion and deformation occur as sediments are scraped off the subducting plate and added to the wedge (Burg, 2018). The onshore wedge, a 150–200-km-wide zone on land, comprises deformed sediments that have been uplifted and exposed due to ongoing tectonic processes. These two parts are separated by a narrow coastal belt, only a few km wide, characterized by prominent normal faults and mud volcanoes both onshore and offshore (Von Rad et al., 2000; Back and Morley, 2016; Burg, 2018). This coastal belt represents the transition zone between the active submarine accretion and the uplifted onshore wedge.

Wide-angle seismic lines indicate that the oceanic crust south of the trench has a thickness of approximately 9 km and is overlain by more than 7,000 m of undeformed sediments at the front of the wedge (Figure 2-5) (White and Louden, 1982; Harms et al., 1984; Kopp et al., 2000; Dolati, 2010). The combined thickness of deformed and undeformed sediments reaches over 10 km near the coastline, reflecting significant sediment accumulation due to high sedimentation rates and tectonic convergence (White and Louden, 1982; Harms et al., 1984; Kopp et al., 2000). Interpretations of seismic data place a décollement (detachment) at a depth of approximately 3–4 km (Figure 2-5) near the deformation front (Kopp et al., 2000). Above the décollement, sediments are intensely folded and thrust, contributing to the growth and deformation of the accretionary wedge (Figure 2-6) (White and Klitgord, 1976; Harms et al., 1984; Grando and McClay, 2007; Ellouz-Zimmermann et al., 2007). Sediments below the décollement continue to subduct with the oceanic crust, a process known as underplating (e.g., Platt et al., 1985), which contributes to crustal thickening and may play a role in uplift and exhumation processes (Figure 2-6).

The main accretion phase of the emerged wedge produced growth structures dating from the late Miocene to early Pliocene (Dolati, 2010). Since the late Pliocene, the coastal Makran and mid-slope areas have

experienced surface uplift, normal faulting, shale extrusion, and shortening (Harms et al., 1984; Grando and McClay, 2007; Dolati, 2010). These processes contribute to the complex structural architecture of the Makran accretionary wedge and influence seismicity, sedimentation, and surface processes.

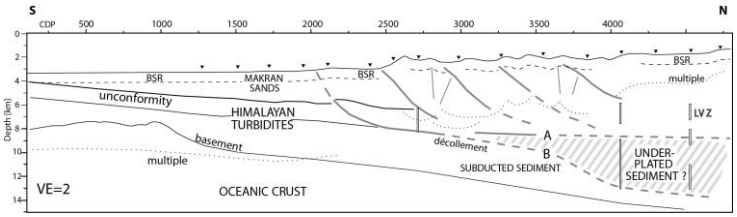

Figure 2-5. The structure of the Makran accretionary wedge, illustrating underplated sediments beneath a gently dipping décollement (Kopp et al., 2000).

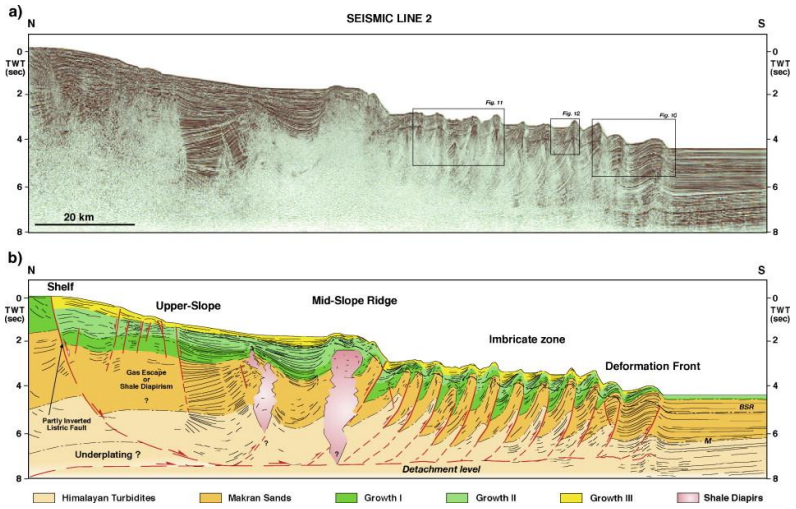

Figure 2-6. Seismic profile (a) and the interpretation (b) across the western offshore Makran accretionary prism, showing the shelf, slope basins, and accretionary prism. The M unconformity separates Himalayan turbidites from Makran Sands. The interpretation highlights growth strata, shale diapirs, the imbricate zone, and the deformation front, with potential underplating and a detachment level identified (Grando and McClay, 2007).

2.1.3 Accretionary Wedge Stratigraphy

The sedimentary architecture of the Makran region is intricately structured within the accretionary wedge and is categorized into four distinct zones (Figure 2-1) from south to north: Coastal Makran, Outer Makran, Inner Makran, and North Makran (e.g., Dolati, 2010; Haghipour and Burg, 2014; Burg, 2018). Each zone exhibits unique sedimentary and igneous characteristics that reflect the evolutionary stages of the accretionary processes in the region (Figure 2-7).

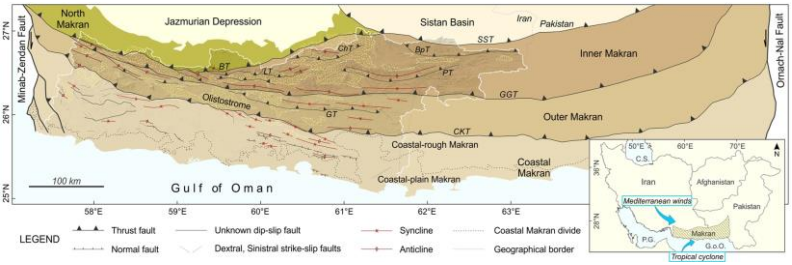

Figure 2-7. Tectonostratigraphic zones of the Makran accretionary wedge (Kaveh-Firouz et al., 2023). BT: Bashakerd thrust fault, SST: Sistan-Siahan Thrust, BpT: Bamposht thrust fault, ChT: Chanf thrust fault, LT: Lashar thrust fault, PT: Pishamak thrust fault, GGT: Qasr-e-Qand thrust fault, GT: Gativan thrust fault, and CKT: Chah Khan thrust fault.

2.1.3.1 Coastal Makran:

To the south of the Outer Makran lies the Coastal Makran zone (Figure 2-7), which represents a wedge-top basin setting. This area showcases a shallowing-upward sequence transitioning from late Miocene slope marls to Pleistocene coastal and continental deposits. The Coastal Makran records the transition from marine to terrestrial environments, influenced by both tectonic uplift and sea-level fluctuations. This province captures the final stages of sedimentary deposition within the accretionary wedge, highlighting the interplay between sediment supply and tectonic forces (Dolati, 2010; Haghipour and Burg, 2014).

2.1.3.2 Outer Makran:

Located between the Qasr-e-Qand and Chah Khan thrust faults (Figure 2-7), the Outer Makran zone comprises lower to middle Miocene siltstones and marls, which include calcareous sandstones that grade up-section into shallower facies indicative of a shelf environment. These sediments include Burdigalian-age deposits and shallow-water carbonate facies that transition upward, indicating a progression towards shallower marine environments. The Outer Makran records a significant phase of sedimentation that reflects changes in sea level and tectonic uplift, contributing to the complex stratigraphic layering observed in this province (Dolati, 2010; Haghipour and Burg, 2014).

2.1.3.3 Inner Makran:

Situated north of the Qasr-e-Qand fault (Figure 2-7), the Inner Makran zone exposes a thick sequence of upper Eocene to lower Miocene terrigenous sandstone and shale sequences, characteristic of "flysch"-type deposits. These sediments are interpreted as part of a proto-Indus fan system, which records the ongoing Himalayan orogeny and the associated sedimentary influx (Kopp et al., 2000; Ellouz-Zimmermann et al., 2007). Syn-sedimentary deformation is evident in this region, marked by growth structures and an upward shallowing trend in sedimentary facies (Dolati, 2010), which reflect active tectonic loading and sedimentation dynamics during deposition.

2.1.3.4 North Makran:

Located to the north of Bashakerd thrust fault (Figure 2-7), the North Makran zone is predominantly characterized by mafic to intermediate igneous rocks. This area features tectonic mélanges, which are complex mixtures of igneous rocks and deep-water sediments, indicative of intense tectonic activity. The sedimentary record here includes Cretaceous deep-water sediments, providing insights into the region's ancient marine environments. Additionally, there are localized occurrences of upper Cretaceous shallow-water limestones. Along the Jaz Murian depression, Paleogene limestones are found unconformably

overlying deformed Cretaceous sediments and igneous rocks, illustrating periods of uplift and erosion. Near Espakeh, Eocene sandstone formations are present, adding to the sedimentary diversity of this province (Dolati, 2010; Haghipour and Burg, 2014; Burg, 2018).

An extensive Tortonian olistostrome, dated between 7 and 11 million years ago, plays a significant role in the sedimentary history of the Makran region. This olistostrome comprises giant blocks of both igneous and sedimentary rocks sourced from the North Makran and Inner Makran provinces. Emplaced predominantly over much of the North and Inner Makran areas, the olistostrome was later subjected to partial erosion, shaping the current geological landscape (Burg et al., 2008; Haghipour and Burg, 2014). The presence of this large-scale mass transport deposit underscores the dynamic tectonic environment and the processes of sedimentary deformation that have been active in the Makran accretionary wedge.

2.1.4 Uplift along the Coast

The Coastal Makran (Figure 2-8) is an active morphodynamic zone influenced by a combination of tectonic uplift, eustatic sea-level changes, sediment supply, and coastal processes (Gharibreza, 2016). The coastline features multiple marine terraces and raised beaches, indicating phases of uplift and relative sea-level change (Vita-Finzi, 1979, 1987; Gharibreza, 2016). Studies have identified up to 19 marine terraces between the present sea level and elevations of 246 m near Chabahar (Vita-Finzi, 1979). The mean uplift rate along the Iranian coastline is estimated at 1.1–2.6 mm/yr since the mid-Holocene (approximately 6 ka), when sea levels were 2–3 m higher than present (Falcon, 1974; Lambeck, 1996; Gharibreza, 2016).

Radiocarbon dating (^{14}C) of shells and corals from marine terraces provides chronological constraints on uplift and sea-level changes (Vita-Finzi, 1979, 1987; Snead, 1993). For example, shells at 4 m above sea level near Chabahar were dated to 3,670 ± 50 years before present (BP), while higher elevations yielded ages between 28 and 30 kaBP (Vita-Finzi, 1979).

The morphology of the coastline (Figure 2-8), including omega-shaped bays and curved bays, reflects the interplay between tectonic uplift, sediment dynamics, and sea-level fluctuations (Gharibreza, 2016). Paleoshorelines serve as indicators of past sea levels and sedimentary environments.

The coastal plain exhibits evidence of progradation due to high sediment supply from rivers and coastal erosion of uplifted terraces. This results in the formation of beach ridges, cheniers, and other coastal landforms. The sorting of sediments along the littoral drift leads to the accumulation of sand and shell-rich ridges, influencing the development of paleoshorelines and the coastal sedimentary record (e.g., Gharibreza, 2016). Eustatic sea-level fluctuations during the late Quaternary, combined with tectonic uplift, have shaped the coastal geomorphology and sedimentation patterns (Lambeck, 1996; Gharibreza, 2016).

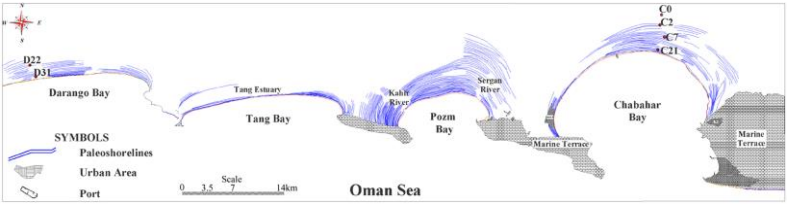

Figure 2-8. Morphological setting of the Coastal Makran, showing paleoshorelines along the Chabahar, Pozm, Tang and Darango bays (Gharibreza, 2016).

2.2 Structural Features of Makran

The Makran accretionary wedge exhibits a complex structural framework resulting from the ongoing northward subduction of the Arabian Plate beneath the Eurasian Plate (e.g., Dolati, 2010). The deformation within the Makran accretionary wedge is manifested through various structural features, predominantly folds and faults, which reflect the intricate interplay of tectonic processes. This section provides an in-depth analysis of these structural features, focusing on their types, distributions, orientations, and the tectonic processes shaping the region.

2.2.1 Folds

Folding is a significant deformation feature within the Makran accretionary wedge, arising from compressional forces associated with subduction and accretion processes (Jacob et al., 1979; McCall and Kidd, 1982; Berberian et al., 1982). The folds exhibit considerable variation in style, scale, and intensity across different structural units, reflecting the heterogeneity of lithologies, and the differences in structural levels, and the evolution of the tectonic regime (Dolati, 2010).

In the northern parts of the Makran accretionary wedge, particularly within the Inner Makran, folding is intense, characterized by tight to isoclinal folds prevalent in the upper Oligocene turbidites of the Pishamak and Kajeh Thrust Sheets (Dolati, 2010). These folds exhibit steeply dipping to overturned limbs and have wavelengths ranging from centimeters to kilometers. The hinge zones often display well-developed axial plane cleavage, indicative of high strain (Alvarez et al., 1978; Powell, 1979). For instance, in the sandstone-dominated Pirdan Unit of the Pishamak Thrust Sheet, chevron folds are common due to the alternation of competent sandstone layers and weaker shales (Dolati, 2010).

Conversely, in the Coastal Makran and Outer Makran zones, folds are generally open to gentle, with large wavelengths often exceeding 1,000 m and low amplitudes (Harms et al., 1984). These folds are typically symmetric, with rounded to blunt hinge zones, and lack significant axial plane cleavage, suggesting weaker deformation. In the Gativan Thrust Sheet, large box folds with wavelengths greater than 4 km are observed, particularly in lower Miocene sequences (Dolati, 2010).

The Imbricate Zone, located between the Bashakerd Thrust Sheet and the Inner Makran, also exhibits folding but to a lesser degree. Here, open and rounded folds with wavelengths over 100 meters are present, reflecting moderate deformation. These folds have a general east-west trend, consistent with regional tectonic forces, and the axial planes are often weakly developed (Dolati, 2010).

2.2.2 Faults

Faulting is a critical component of the structural framework of the Makran accretionary wedge, accommodating deformation through thrusting, normal faulting, and strike-slip movements. The intricate fault networks contribute to the complex tectonic evolution of the region.

2.2.2.1 Thrust Faults

Thrust faulting is the primary mechanism for accommodating convergence within the Makran accretionary wedge, resulting in the stacking of thrust sheets and the development of the accretionary wedge (Jacob et al., 1979; McCall and Kidd, 1982; Harms et al., 1984; Dolati, 2010).

2.2.2.2 Flat and Ramp Systems

Thrust faults in the Makran accretionary wedge commonly display flat and ramp geometries, where thrust planes follow bedding planes (flats) and cut across layers (ramps) (McClay, 1992; Dolati, 2010). This geometry is evident in the Lashar Thrust Zone, where strata-parallel faults and ramp faults are observed, leading to the development of fault-propagation folds in the hanging wall (Dolati, 2010). These structures are indicative of thin-skinned tectonics prevalent in turbidite sequences.

2.2.2.3 Backthrusts

Backthrusts, or south-dipping reverse faults, are present in the northern parts of the Makran accretionary wedge, particularly in the Imbricate Zone. For example, to the north of Fannuj, the Bashakerd Thrust Sheet is thrust northwestward onto the Imbricate Zone along backthrusts (Dolati, 2010). These structures reflect complex stress regimes within the accretionary wedge and contribute to the intricate structural architecture (Dolati, 2010).

2.2.2.4 Normal Faults

Normal faulting in the Makran accretionary wedge is less extensive but plays a significant role in accommodating extensional stresses, particularly in the Coastal Makran. In the Coastal Makran, normal faults are widespread, cutting through sediments younger than upper Miocene (Dolati, 2010). These faults are typically planar and non-rotational, with displacements ranging from a few meters to several meters (Dolati, 2010). They are associated with extensional tectonics, possibly related to gravitational collapse or regional stress relaxation (Harms et al., 1984; Grando and McClay, 2007).

Conjugate sets of normal faults are observed, indicating a complex extensional stress field. For instance, conjugate north-northeast- and south-southeast-dipping planes suggest sub-radial extension, while sediment-filled fissures and bookshelf faulting patterns indicate localized extensional regimes (Dolati, 2010).

The presence of normal faults in the Coastal Makran has implications for seismic hazards. Extensional structures can influence stress distribution and may contribute to seismic events (Khan et al., 1991; Dolati, 2010). The normal faulting observed in Pliocene–Pleistocene sediments suggests that extensional tectonics are relatively recent and possibly ongoing.

2.2.2.5 Strike-Slip Faults

Strike-slip faulting is a significant deformation mechanism within the Makran accretionary wedge, accommodating lateral movements and contributing to the complex tectonic fabric.

Two main sets of conjugate strike-slip faults are dominant (Dolati, 2010). Northeast–Southwest sinistral (left-lateral) faults: These faults are widespread across the Makran accretionary wedge and often offset major thrusts and folds, indicating a younger deformation phase. Displacements range from a few meters to over 2,000 m, and they significantly influence the topography and river patterns (Dolati, 2010). Northwest–Southeast dextral (right-lateral) faults: These faults are conjugate to the sinistral faults, and together they form a pattern

consistent with bulk north-northeast–south-southwest compression (Dolati, 2010).

Strike-slip faults cut through Pliocene–Pleistocene sediments and are evident in satellite imagery due to their offsetting of resistant lithologies like sandstone (Dolati, 2010). The youngest strike-slip faults affect the topography and are considered active structures contributing to the ongoing deformation of the Makran accretionary wedge. Similar strike-slip faults have been recognized offshore Pakistan across the active front of the Makran (e.g., Kukowski et al., 2002).

2.2.3 Deformation Gradient

There is a discernible deformation gradient from north to south within the Makran accretionary wedge. The Inner Makran exhibits intense deformation with tight folding and significant thrusting, reflecting strong compressional forces near the subduction zone (Harms et al., 1984; Platt et al., 1985; Dolati, 2010). Towards the south, deformation decreases, with the Outer Makran and Coastal Makran displaying open folds and normal faulting indicative of weaker deformation and extensional regimes.

2.2.4 Strain Partitioning

The coexistence of compressional, extensional, and strike-slip structures indicates strain partitioning within the accretionary wedge. This partitioning may be influenced by factors such as variations in sediment thickness, mechanical stratigraphy, rheological contrasts between lithologies, and spatial changes in convergence rates along the subduction zone (Farhoudi and Karig, 1977; Byrne et al., 1992; Dolati, 2010).

2.3 Seismicity

The recorded seismicity in the Makran region is notably low compared to adjacent areas and most other subduction zones, a phenomenon that has intrigued geoscientists (Dolati, 2010). The seismic behavior of the Makran

subduction zone is characterized by distinct segments. The western part of the Makran subduction zone is considered relatively aseismic. Historical records do not indicate any large seismic events, and modern instrumentation has not detected significant shallow seismicity over the past few decades (e.g., Byrne et al., 1992). Most earthquakes in this segment occur at depths of about 70 km within the subducting plate.

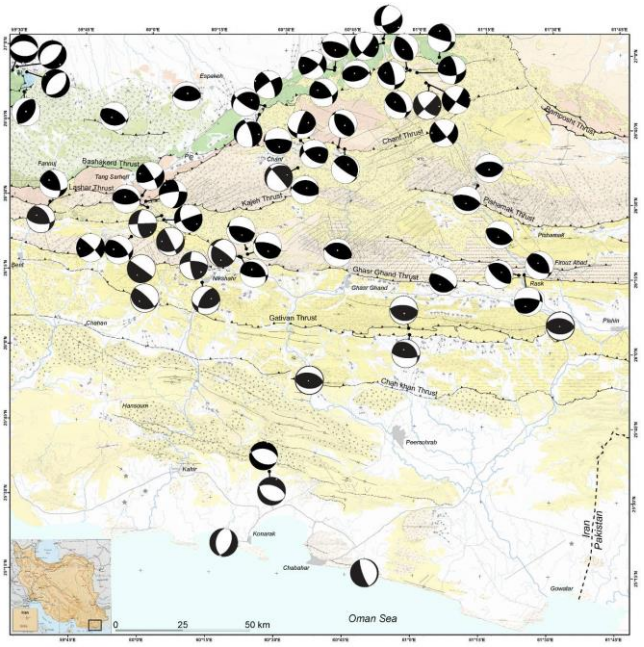

Figure 2-9. Major focal mechanisms over the Makran accretionary wedge and adjacent areas, illustrating the segmentation and seismicity patterns (Dolati, 2010).

In contrast, the eastern segment exhibits higher seismic activity. The most significant event was the M_w 8.1 earthquake of November 1945, which occurred at a depth of 30 km and generated a tsunami that affected the coastlines of Pakistan, Iran, Oman, and India (Page et al., 1979; Byrne et al., 1992; Heidarzadeh et al., 2008). This earthquake ruptured approximately 200 km of the subduction zone. Segmentation of the subduction zone is further evidenced by two seismic events in central

Makran that displayed dextral strike-slip motion, suggesting complex stress regimes and potential transform faulting within the subduction zone (Byrne et al., 1992; Dolati, 2010).

Table 2-1. Earthquake fault plane solutions within the study area (see Figure 2-9). M, s, d, and r represent magnitude, strike, dip, and rake, respectively. Depths are in km.

No.	Date	Long	Lat	Depth	M	s1	d1	r1	s2	d2	r2	References
1	27.11.1945	63.48	26.15	27.00	7.9	246	7	89	67	83	90	Byrne et al. (1992)
2	05.08.1947	63.49	25.04	20.00	6.8	236	7	68	78	84	93	Byrne et al. (1992)
3	10.01.1979	60.95	26.55	3.00	5.8	256	61	13	160	77	150	Byrne et al. (1992)
4	10.01.1979	61.02	26.48	2.00	5.9	230	82	-4	321	86	-17	Byrne et al. (1992)
5	08.08.1972	61.22	25.14	18.00	5.0	334	15	148	95	82	77	Byrne et al. (1992)
6	03.08.1968	62.87	25.19	26.00	4.7	290	49	-50	58	55	-126	Byrne et al. (1992)
7	13.02.1969	62.75	24.99	18.00	5.1	279	9	84	105	81	91	Byrne et al. (1992)
8	06.08.1972	61.22	25.04	20.00	5.4	321	17	134	96	78	78	Byrne et al. (1992)
9	08.08.1972	61.22	25.14	18.00	5.4	334	15	148	95	82	77	Byrne et al. (1992)
10	18.08.1972	63.14	24.83	20.00	4.6	277	9	84	103	81	91	Byrne et al. (1992)
11	02.09.1973	63.21	24.88	18.00	5.2	281	23	70	123	68	98	Byrne et al. (1992)
12	29.07.1975	63.09	25.22	18.00	5.0	278	27	88	100	63	91	Byrne et al. (1992)
13	10.02.1978	62.40	25.33	18.00	5.1	214	16	19	106	85	105	Byrne et al. (1992)
14	29.05.1963	59.40	27.00	52.00	5.2	46	18	-90	226	72	-90	Chandra (1984)
15	12.08.1963	63.14	25.32	5.00	5.4	190	30	0	100	90	120	Quittmeyer et al. (1984)
16	06.08.1972	61.22	25.04	33.00	5.5	292	22	114	86	70	81	Chandra (1984)
17	08.08.1972	61.22	25.14	30.00	5.5	280	5	90	100	85	90	Chandra (1984)
18	02.09.1973	63.21	24.88	30.00	5.3	270	30	90	90	60	90	Quittmeyer et al. (1984)
19	10.01.1979	60.95	26.55	33.00	5.9	300	40	90	120	50	90	Jackson and McKenzie (1984)
20	10.01.1979	61.02	26.48	33.00	5.9	300	34	90	120	56	90	Jackson and McKenzie (1984)
21	01.01.1980	60.27	26.99	64.10	5.4	208	80	-	118	88	-10	GCMT
22	07.12.1991	62.94	25.08	15.00	5.6	309	8	133	85	84	85	GCMT
23	30.01.1992	62.88	24.25	15.00	5.8	298	10	126	82	82	84	GCMT
24	17.12.1992	61.43	25.68	37.00	5.7	8	54	142	123	60	43	GCMT
25	24.06.2003	60.91	27.00	72.40	5.5	97	45	-65	244	50	-112	GCMT
26	13.03.2005	62.00	26.73	58.00	6.0	253	37	-89	72	53	-90	GCMT
27	18.07.2006	61.23	26.07	30.80	5.3	107	67	-12	201	79	-157	GCMT
28	30.09.2013	60.18	26.72	16.20	4.7	87	44	-28	198	71	-131	GCMT
29	04.05.2015	61.23	26.12	36.30	5.1	308	83	4	218	86	173	GCMT
30	07.02.2017	63.25	25.01	14.00	6.4	249	6	64	95	84	93	GCMT
31	08.02.2017	63.25	24.79	23.40	5.3	300	19	101	108	71	86	GCMT
32	31.07.2022	63.55	25.05	26.30	5.6	162	39	104	324	52	79	GCMT
33	31.07.2022	63.53	25.01	29.10	5.0	3	46	102	166	46	78	GCMT
34	05.03.2024	59.34	26.89	88.50	5.2	35	71	164	131	75	19	GCMT

The low seismicity in the western segment has raised concerns about the potential for future large earthquakes due to the long seismic gap and accumulated strain (Byrne et al., 1992). The occurrence of the 1945 earthquake in the eastern segment highlights the possibility of megathrust earthquakes and associated tsunamis in the region (Heidarzadeh et al., 2008).

Factors contributing to the seismic behavior include sediment thickness, subduction angle, and thermal regime. The thick sediments in the subduction zone may influence the mechanical properties of the plate interface, potentially affecting seismic coupling and the occurrence of slow slip events or aseismic creep (Kopp et al., 2000; Smith et al., 2012). The shallow subduction angle may lead to a wider seismogenic zone but also complicate stress accumulation and release patterns. The low geothermal gradients measured in wells in the onshore Pakistani Makran (about 20°C per km) suggest a cooler subduction zone, which may affect the frictional properties of the plate interface (Harms et al., 1984; Khan et al., 1991).

3 Methods and data

This project serves as a beacon, charting a course toward a future of rapid, accurate, and large-scale geological mapping, even for the most complex and remote areas. Ultimately, the project demonstrated that with the right combination of data, technology, and expertise, we can achieve new levels of understanding in geological studies.

3.1 Converting Archived Paper Data into Digital Resources

In this study, two key activities were undertaken: (1) Documentary and Data Collection, and (2) Unlocking Data Trapped in Paper. The primary objective of these activities was to enhance the added value of the research and optimize the operational efficiency of the project.

The first activity focused on the systematic collection of data relevant to the project's scope. This was accomplished through extensive searches across various internal and external sources. The data gathered included base maps, project reports, academic theses, and scholarly articles. Each piece of information was carefully reviewed, analyzed, and selected based on its relevance and usefulness for the project's objectives.

The second activity aimed at addressing the limitations posed by the format of the collected data. Many of the sources were originally in non-digital forms—such as paper documents, text manuscripts, and images—which were not directly usable in their original state for advanced digital research. To overcome this challenge, the data was meticulously categorized and positioned based on its inherent value and credibility. Subsequently, a usable geodatabase was generated. This geodatabase includes a variety of digital assets, such as elevation data, images,

coordinate data, sampling points, structural sections, stratigraphic columns, as well as texts and tables associated with the selected data.

3.2 Remote Sensing

In the study of terrestrial resources, two general methods exist for collecting information: (a) field-based methods and (b) Remote Sensing (RS). One of the modern and effective tools now available in environmental studies, earth sciences, and mineral exploration is the use of remote sensing technology and the utilization of satellite data along with high-performance computer systems (Jensen, 2016; Sabins and Ellis, 2020).

Remote sensing plays a crucial role in modern geological mapping and mineral exploration by providing efficient and cost-effective methods for surveying large areas and identifying potential mineral deposits (Goetz et al., 1983). This technology involves collecting and analyzing images of the Earth's surface using satellite sensors or airborne platforms (Richards, 2013).

3.3 Cloud Computing

Cloud computing can be defined as an on-demand system based on computational capabilities, especially in storing massive amounts of data and processing power, which is not directly managed by users. Large cloud infrastructures usually have distributed functions in various locations other than the central core. These cloud systems can be limited to a single organization, in which case they are referred to as private clouds. Alternatively, they can be shared among multiple organizations, known as public clouds. The main philosophy behind such systems is to share information resources to achieve economies of scale and integration. In other words, these systems enable companies to minimize the staggering costs of IT infrastructure.

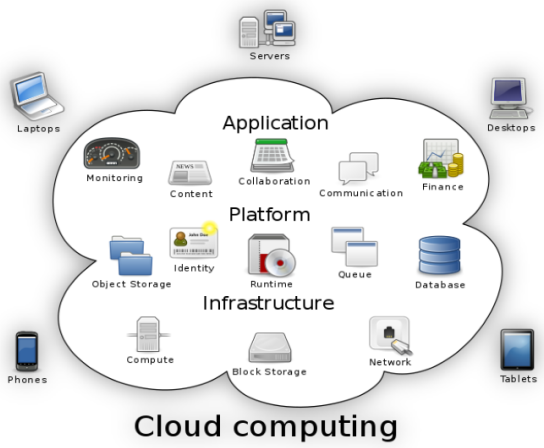

Figure 3-1. illustration of the main components of a cloud computing system.

3.3.1 Google Earth Engine

The *Google Earth Engine* system, as a cloud computing platform, enabled—for the first time in history—the rapid processing of vast amounts of satellite imagery (Gorelick et al., 2017). For example, without this system, monitoring changes in vegetation cover, water resources, and land on a global scale would not have been possible (Kumar and Mutanga, 2018). This platform has created a multi-petabyte (1015 or 250 bytes) database of satellite images and other geospatial information, along with processing functions and operators on a planetary scale. These two unique capabilities have provided scientists, researchers, and computer programmers with tools to examine environmental changes and trends (Amani et al., 2020). The three components that make up this powerful system are Satellite Imagery, Processing Algorithms, and Environmental Applications (Figure 3-2).

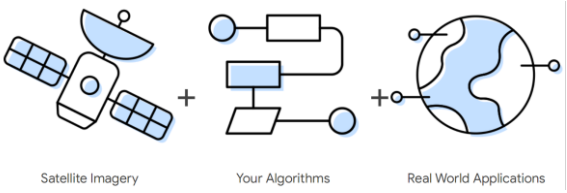

Figure 3-2. The three key components of the *Google Earth Engine* system as a Cloud Computing Platform.

3.4 Satellite Imagery and Digital Elevation Model (DEM)

This project utilized a wide range of information and images available in the *Google Earth Engine* database archive (Table 3-1). For satellite imagery, efforts were made to ensure that all images were from the same time period. However, for other data and information such as the emissivity from the ASTER sensor and Digital Elevation Model (DEM) data from the Shuttle Radar Topography Mission (SRTM), the existing archives were used. All of this information and data were processed using their respective algorithms, which are explained in detail in the following sections related to each dataset.

Table 3-1. List of satellite imagery and DEM used in the SUTGMM project.

No.	Data	Type	Acquisition Date	Level of Corrections	Spatial Resolution
1	Sentinel-2	MultiSpectral Instrument (MSI)	July 2019	Geometric correction, atmospheric correction, cloud cover <5%	10 and 20 m
2	Sentinel-1	Dual-polarization C-band Synthetic Aperture Radar (SAR)	July 2019	Calibrated, ortho-corrected product	10, 25, and 40 m
3	Landsat 8	Operational Land Imager (OLI)	July 2019	Atmospherically corrected surface reflectance	30 m
4	ASTER	ASTER (VNIR, SWIR, TIR)	2002	-	15, 30, and 100 m
5	NASA JPL	Shuttle Radar Topography Mission (SRTM)	2002	-	30 m

3.5 Object-Based Process for Geological Mapping of Mineral Potential

In extracting geological information—whether identifying lithological units or promising areas—two general approaches can be employed: pixel-based and object-based methods. In the pixel-based approach, the processing unit is the pixel, and the spectral information of the pixels is utilized. Advantages of this classification include low computational cost and the feasibility of applying it to large areas (Jensen, 2016). However, limitations and disadvantages of this method include its incompatibility with real-world entities and their behavior; in other words, on the ground, there is no entity called a pixel—we deal with land units (Blaschke, 2010). The second limitation pertains to the type and number of features used. In pixel-based methods, features must be homogeneous and from a single source (for example, all inputs are spectral bands), which restricts the use of pixel-based methods (Lu and Weng, 2007).

To mitigate this problem, the object-based classification technique is employed. In object-based classification, instead of using pixels as the smallest classification unit, image objects are used. An object in the image is a homogeneous region where pixels have similar characteristics and corresponds to a geographical entity in the real world (Blaschke et al., 2014). In object-based classification, features are calculated for each segment, and classification is performed at the object level.

In the object-based process of extracting geological maps (lithological units), the first step is to perform segmentation on the images. Typically, in the segmentation phase, the image with the highest spatial accuracy is used. Therefore, in this project, higher spatial resolution images are utilized (Drăguţ et al., 2014).

3.6 Image Segmentation

An object can be defined as an image entity consisting of a group of pixels that have similarity in grayscale values within a specific range and are connected in shape, geographical location, and size to real-world objects

(Blaschke et al., 2014). Spectrally, objects are homogeneous regions in the image with defined boundaries. Segmentation is used to identify these homogeneous regions. It is one of the most important parts of object-based classification, and the results greatly depend on how the image is segmented (Hay and Castilla, 2008).

In multiscale segmentation algorithm (Baatz and Schäpe, 2000), scale plays a crucial role in determining segments and influences characteristics like spectral texture and shape. Using region-merging techniques, for a certain number of image segments, average heterogeneity is minimized, and their homogeneity is maximized. As a result, the segmentation algorithm is controlled by a scale factor and a heterogeneity criterion. The scale factor indirectly relates to the average size of segments to be identified. The heterogeneity criterion controls the merging process and is calculated using spectral layers (e.g., multispectral images). It includes two distinct and unique features: color and shape. Color refers to spectral convergence, while shape considers the semantic features of objects and is divided into two unique features: smoothness and compactness. Optimal segmentation parameters depend on the scale and nature of the features to be identified. Once an appropriate scale is identified, the color and shape criteria are adjusted to refine the shape of image segments (Blaschke et al., 2014). Advantages of this method include its applicability to various data types and suitable performance with large image datasets (Blaschke, 2010).

3.7 Machine Learning

Machine learning is a growing technology that enables processing systems to automatically learn from historical data. It uses various algorithms to build mathematical models and make predictions based on existing data or observational information (Alpaydin, 2020). Currently, these algorithms are used for various tasks such as medicine, earth sciences, finance and business topics, face recognition, speech recognition, and many other areas (Jordan and Mitchell, 2015).

In the real world, humans can learn everything from their past experiences due to their ability to learn. Today, computational systems or machines work according to our instructions. But can a machine also learn from past experiences or historical data like a human? This is where the role of machine learning comes into play (Russell and Norvig, 2021).

Machine learning enables systems to continuously update and improve from new data, enhancing the accuracy and efficiency of predictions and decision-making (Kelleher and Tierney, 2018). These capabilities are of particular importance in today's world, especially in scientific and industrial fields, helping researchers and engineers tackle more complex problems.

3.7.1 Random Forest

Random forest is a widely used machine learning algorithm that belongs to supervised learning techniques. It can be used for classification and regression problems in Machine Learning (ML) (Breiman, 2001). This method is based on the concept of ensemble learning, which is a process of combining multiple classifiers to solve a complex problem and improve the model's performance (Zhou, 2012).

Random forest is considered a supervised learning algorithm. As its name suggests, this algorithm builds a forest randomly. The constructed "forest" is actually a group of decision trees (Figure 3-3). The work of building a forest using trees is often done by the bagging method. The main idea of the bagging method is that a combination of learning models increases the overall results of the model (Breiman, 1996). Simply put, random forest builds multiple decision trees and merges them together to obtain more accurate and stable predictions (Figure 3-3). One of the advantages of random forest is its applicability to both classification and regression problems, which constitute the majority of current machine learning systems (Liaw and Wiener, 2002).

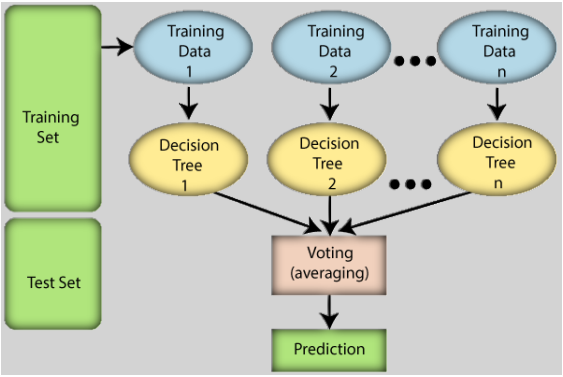

Figure 3-3. A schematic diagram of random forest structure.

Random forest can perform both classification and regression tasks. It can manage large datasets with high dimensionality. It increases the accuracy of the model and prevents the overfitting problem.

3.7.2 Deep Learning

Deep learning, as one of the most prominent branches of artificial intelligence and machine learning, has achieved remarkable success in recent decades and has transformed the structure of many modern technologies. This technology is based on multilayer artificial neural networks that, by mimicking the structure of human brain neurons, aim to process and analyze complex and multidimensional data (LeCun et al., 1998, 2015). Deep learning uses a layered architecture that processes data hierarchically, transferring information from simple layers to more complex ones. For this reason, it is known as "deep" because it includes a large number of hidden layers that sequentially process and extract information (Schmidhuber, 2015).

Depending on the type of data and application, various types of neural networks are used in deep learning. Each of these networks has specific features and structures that make them suitable for specific applications:

- Convolutional Neural Networks (CNNs): Specially designed for processing images and two-dimensional data, used in

applications such as face recognition, object detection, medical image analysis, and remote sensing (Simonyan and Zisserman, 2014) .

- Recurrent Neural Networks (RNNs): Designed for processing sequential data like text, speech, and time signals. For example, in machine translation, the network can better understand the semantic context by processing sentences in order (Sutskever et al., 2014).
- Advanced Neural Networks like LSTM and Attention Mechanisms: These networks solve the problems of RNNs in managing and learning long-term information and are used in various fields such as language translation, text summarization, and time series in geology like environmental hazards (Bahdanau et al., 2016).

One of the prominent advantages of deep learning is its ability to automatically extract features. Unlike traditional machine learning methods, where experts must manually extract and select features, in deep learning, networks automatically learn important and complex features from data. For this reason, deep learning has led to more accurate results in analyzing complex data such as images, audio, and text (LeCun et al., 2015).

3.7.2.1 Applications of Deep Learning in Geosciences

The use of deep learning in geosciences, especially in geology and mineral exploration, has brought about a fundamental transformation. This technology helps identify patterns and hidden features important for detecting areas with mineral potential by analyzing a vast volume of geophysical, geochemical, and satellite imagery data. In this section, we discuss some key applications of deep learning in geosciences that have aided in improving geological mapping processes and mineral exploration.

Traditionally, creating geological maps requires detailed field studies, sampling, and laboratory analyses, which are time-consuming and costly.

However, using deep learning models, especially Convolutional Neural Networks (CNNs), it becomes possible to automatically and accurately analyze remote sensing data like satellite images and LiDAR data. These models can identify various geological features such as rocks, earth layers, and structural changes based on spectral patterns, color, and texture (Gagnon, 2020).

For example, in a conducted study, CNNs were able to analyze satellite images to detect areas with specific geological features like fractures, faults, and soil types. These methods can be particularly useful in areas with limited access or challenging conditions, as they eliminate the need for costly field surveys and sampling (Rajabifard and Hunter, 2018).

3.7.2.2 Convolutional Neural Networks (CNNs)

Convolutional Neural Networks (CNNs) are one of the most important and prominent architectures of deep learning, which have found widespread applications especially in processing image, video, and other complex data. These networks, using a multilayer structure, automatically extract complex features from data and are used for various tasks such as object recognition, image classification, pattern recognition, and even prediction. In this section, we will provide a more detailed explanation of how CNNs work, their various components, and their applications.

The Convolutional Neural Network (CNN) was the main model for data classification. In this model, the extracted features were input into the CNN so that the network could learn various geological features and patterns.

3.7.3 Random Forest in Extracting Lithological Units

In this project, since the object-based approach was used in image processing and classification, the training samples were selected from among image segments. It should be noted that in the process of converting the Sentinel-2 image, the entire area was first segmented into about 9,000 homogeneous segments based on segmentation parameters. Then, based on Table 3-1 (the images used) and Error!

Reference source not found. (the variables extracted from them), 73 spectral, topographic, and shape variables were determined as input features for each segment.

In the classification process with the help of Random Forest, the goal was to extract 18 classes, including 16 lithological units and two classes of water and vegetation cover. Based on statistical criteria, usually 30% of the samples are used to train the algorithm, and then the algorithm classifies the remaining segments based on the training samples (Figure 3-3). Accordingly, out of 8,959 samples, 2,688 samples were randomly selected based on the frequency of each class (Figure 3-4).

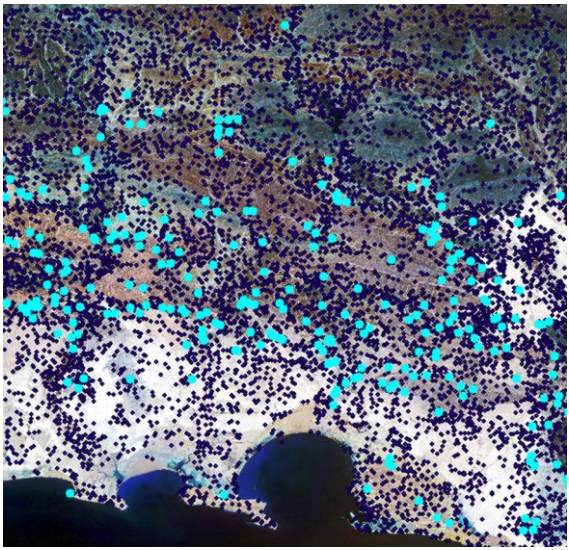

Figure 3-4. Examples of selected points (light blue circles) for the M-Pl^{m,s} lithological unit.

Then, in the process of training the random forest algorithm, 70% of these 30% samples were used for training and 30% for testing the method. For example, for the lithological unit M-Pl^{m,s}, out of 259 samples, 181 samples were used for training and 78 samples were used for evaluating the model. This process was carried out similarly for the remaining units. Below is the sample code executed for random forest machine learning:

```
% Load and prepare your data
% Assuming X is your feature matrix and Y is your target vector
with 18 classes
% X should be a matrix where each row is a sample and each column
is a feature
% Y should be a vector of class labels (1 to 18)

% Split data into training and testing sets
cv = cvpartition(size(X,1),'HoldOut',0.3);
X_train = X(cv.training,:);
Y_train = Y(cv.training);
X_test = X(cv.test,:);
Y_test = Y(cv.test);

% Train Random Forest model
nTrees = 100; % Number of trees in the forest
rf_model = TreeBagger(nTrees, X_train, Y_train, 'Method',
'classification');

% Make predictions on the test set
[Y_pred, scores] = predict(rf_model, X_test);

% Convert predictions from cell array to numeric array
Y_pred = str2double(Y_pred);

% Calculate accuracy
accuracy = sum(Y_pred == Y_test) / length(Y_test);

% Calculate confusion matrix
conf_matrix = confusionmat(Y_test, Y_pred);

% Calculate precision, recall, and F1-score for each class
num_classes = 18;
precision = zeros(num_classes, 1);
recall = zeros(num_classes, 1);
f1_score = zeros(num_classes, 1);

for i = 1:num_classes
    true_positives = conf_matrix(i,i);
    false_positives = sum(conf_matrix(:,i)) - true_positives;
    false_negatives = sum(conf_matrix(i,:)) - true_positives;

    precision(i) = true_positives / (true_positives +
false_positives);
    recall(i) = true_positives / (true_positives +
false_negatives);
    f1_score(i) = 2 * (precision(i) * recall(i)) / (precision(i) +
recall(i));
end
```

```
% Prepare results for Excel
results = table(Y_test, Y_pred, 'VariableNames', {'True_Class',
'Predicted_Class'});

% Add additional sheets for metrics
accuracy_table = table(accuracy, 'VariableNames', {'Accuracy'});
conf_matrix_table = array2table(conf_matrix, 'VariableNames',
cellstr(string(1:18)), 'RowNames', cellstr(string(1:18)));
metrics_table = table((1:18)', precision, recall, f1_score,
'VariableNames', {'Class', 'Precision', 'Recall', 'F1_Score'});

% Write results to Excel file
filename = 'random_forest_results.xlsx';
writetable(results, filename, 'Sheet', 'Predictions');
writetable(accuracy_table, filename, 'Sheet', 'Accuracy',
'WriteRowNames', true);
writetable(conf_matrix_table, filename, 'Sheet',
'Confusion_Matrix', 'WriteRowNames', true);
writetable(metrics_table, filename, 'Sheet', 'Class_Metrics');

disp('Results have been written to random_forest_results.xlsx');
```

3.7.4 Evaluation of the Random Forest Model

After running the model, its performance was evaluated using metrics such as the confusion matrix, Kappa index, precision, Recall, and F1-score. Precision, recall, and F1-score are important metrics in evaluating machine learning models, especially classification models like Random Forest and CNN. These metrics help us accurately assess the model's performance in identifying different data classes and analyze its strengths and weaknesses.

3.7.4.1 Evaluation of the Model for the Entire Area (8,959 Polygons)

A Kappa value of 0.84 indicates a very strong agreement between the predicted classifications and the actual ones (Table 3-2). This means the model performs 84% better than what would be expected by random chance, which is excellent performance, especially for geological classes with inherent complexities. An overall accuracy of 85.6% means that 85.6% of all predictions across the entire area were correct. For a geological classification task with multiple classes, this is a very good accuracy rate.

This model demonstrates excellent performance in classifying geological features over a large and diverse area (8,959 polygons and 18 classes). With a Kappa of 0.84 and an overall accuracy of 85.6%, the model shows strong predictive power and reliability in distinguishing between different geological classes. The strong performance on such a large number of samples indicates good generalization capabilities.

Table 3-2. Accuracy assessment metrics for the entire dataset.

Row	Metric	Value
1	Kappa Index (Kappa)	0.84
2	Variance of Kappa	0.00005
3	Overall Accuracy (%)	85.6
4	Confidence Level	0.95

It appears that the model has effectively managed the diversity and complexity of geological features across the entire area. The high accuracy and reliability of the model make it suitable for practical applications in geological mapping and classification.

The model shows generally good performance across most classes with varying degrees of accuracy. The diagonal elements (blue cells) represent correct classifications, which are generally high for most classes.

- Class-by-class analysis:

  1- High-Performance Rock Units (High Precision and Recall):

  - Q^{a}: With a precision of 0.97 and recall of 0.98, the F1-score is close to 0.975, indicating very good model performance in identifying this class. The high number of samples in this class (958) has contributed to better model learning.

  - $Pl^{silt.cong}$ and $M^{s.silt}$: These units also have high precision and recall (0.929 and 0.902, respectively), which has helped the model achieve more accurate performance in identifying these units.

2- Moderate-Performance Rock Units (Precision or Recall Near Average):

- Q^{al} and Q^{f}: With precision around 0.79 and an F1-score close to 0.80, these classes indicate moderate model performance. This may be due to structural similarities with other classes or limitations in training data for certain features.

- $M\text{-}Pl^{m.s}$ and $M^{sh.s}$: With an F1-score close to 0.85, these units show relatively good performance in identifying rock units.

3- Low-Performance Rock Units (Low Precision or Recall):

- Q^{sd}: With a precision of 0.74 and recall of 0.39, the F1-score is only 0.515, indicating difficulties in correctly identifying this unit. This may be due to the small number of samples or the structural complexity of this unit compared to other classes.

- $Olig\text{-}M^{s.sh.cong}$: With a precision of 0.57 and recall of 0.29, the low F1-score (0.39) indicates the model's difficulty in identifying this unit. Likely, this class faces challenges due to the small number of samples and the complexity of the rocks.

4- Natural Classes (Vegetation and Water):

- Vegetation: With a precision of 0.92 and recall of 0.97, the F1-score is about 0.945, indicating accurate identification of this class by the model. Vegetation is well distinguished due to its structural differences from other units.

- Water: Precision of 0.93 and a lower recall (0.60) indicate that the model has not been successful in identifying some water samples, and the F1-score is 0.738. The lower performance may be due to limitations in the number of samples or feature overlap with other units.

Units with more samples, like Q^{a} and $M^{s.silt}$, perform better due to the availability of more data and sufficient diversity in their features. These units usually have higher precision and recall, indicating the model's success in identifying them. Units with few samples or high complexity,

like Q^{sd} and Olig-$M^{s.sh.cong}$, generally have low F1-scores, highlighting the need to improve training data or enhance the model for better differentiation of these units. Structural differences among classes affect identification. Vegetation is well identified due to its distinct structure, but water has been less successfully identified, possibly due to similarities with features of other units.

Overall, the results indicate acceptable model performance in identifying most rock units, but improvements are suggested for specific units with limited data or high complexity to increase overall accuracy.

The model's ability to maintain high performance over a large number of polygons suggests it could scale to even larger or more diverse geological datasets. In summary, this confusion matrix demonstrates a good geological classification model with varying performance across different classes. It performed well for most major geological formations. The model's strengths in distinguishing between many classes make it a useful tool for geological analysis, although there is room for refinement in some areas. The varying accuracies across classes indicate that while the model is generally reliable, results should be interpreted considering the specific status of some classes.

By utilizing the random forest model and thoroughly evaluating its performance across test samples, training samples, and the entire area, we have developed a robust geological classification. The integrated geological map reflects the model's effectiveness in capturing the geological diversity of the Makran study area (Figure 3-5).

3.7.5 Performance Overview of CNN and RF Methods

One of the objectives of this research is to compare the performance of the machine learning models RF and CNN in classifying geological units with diverse data and different structures. By evaluating and analyzing the metrics of precision, recall, and F1-Score for each model, a deeper understanding of the capabilities and limitations of each of these algorithms can be achieved. Each of these models has its own specific features and strengths; for example, CNN performs well in recognizing

textural features and complex patterns due to the special structure of convolutional layers, while RF, relying on a tree-based structure and using multiple decision trees, is more effective in identifying units with fewer samples and complex structures. This research, in addition to analyzing the overall performance of the two models, examines their performance in specific geological units that have different numbers of samples and diverse geological features.

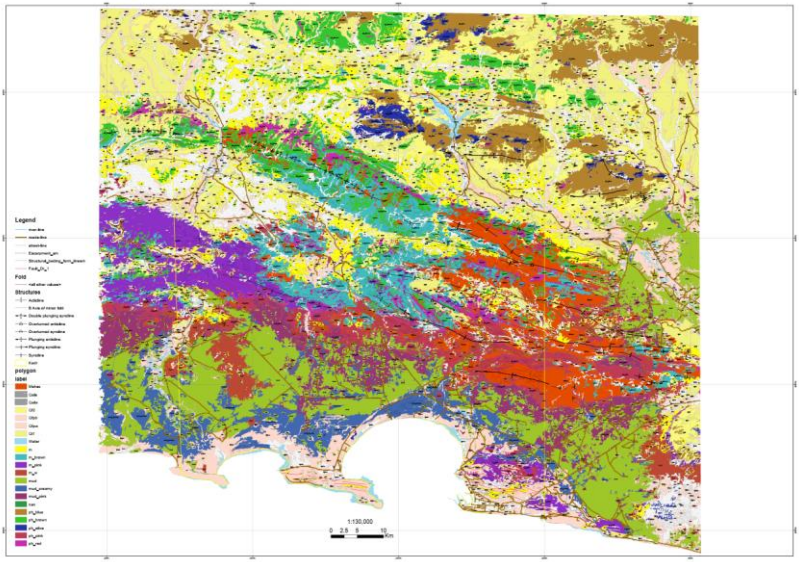

Figure 3-5. Integrated geological map of the Makran study area.

To analyze the performance of the two models, RF and CNN, in classifying geological units, it is necessary to comprehensively examine each of the metrics of Precision, Recall, and F1-Score. This analysis will help in better understanding the capabilities and limitations of these two methods in identifying different geological units and understanding the effects of training data on classification performance.

In this study, two powerful machine learning models, RF and CNN, were used to classify geological units in the study area, and their performance was evaluated based on precision, recall, and F1-Score. This comparative

analysis shows the strengths and weaknesses of each model in identifying different geological units (Table 3-3).

Table 3-3. Accuracy evaluation metrics for all data of the entire region (total of 8,959 segments) by classes using CNN and RF methods.

Order	Geological Unit	F1-Score CNN	F1-Score RF	Support
1	Q^{a}	0.96	0.98	958
2	Vegetation	0.91	0.95	177
3	$Pl^{silt.cong}$	0.83	0.93	409
4	$M^{s.silt}$	0.88	0.9	848
5	$M^{sh.s}$	0.86	0.89	1228
6	$Pl\text{-}Pe^{cong.s.silt}$	0.81	0.86	786
7	$M\text{-}Pl^{m.s}$	0.83	0.85	863
8	$M\text{-}Pl^{m.s.cong}$	0.81	0.85	593
9	$Olig\text{-}M^{sh.s}$	0.79	0.84	471
10	$Olig\text{-}M^{sh}$	0.81	0.82	220
11	Q^{al}	0.74	0.8	825
12	Q^{f}	0.7	0.8	637
13	Q^{b}	0.49	0.75	158
14	$Pl^{l.silt.s}$	0.71	0.74	330
15	Water	0.73	0.74	51
16	Pl^{silt}	0.63	0.7	288
17	Q^{sd}	0.51	0.52	66
18	$Olig\text{-}M^{s.sh.cong}$	0.51	0.39	51
	Total	**80.4%**	**84.7%**	**8959**

The comparison of the overall performance of the models indicates that the Random Forest (RF) model, with an average F1-Score of 0.85, has performed better than the Convolutional Neural Network (CNN) model, which has an average F1-Score of 0.80. RF outperformed CNN in 16 out of the total 18 classes. The greatest performance difference between the two models pertains to class Qb, where RF achieved an F1-Score of 0.75 while CNN scored 0.49.

3.7.5.1 Performance Based on Sample Size

- Classes with a Large Number of Samples (>800 samples):

In these classes, where sufficient samples are available for model training, RF has shown better performance:

$M^{sh.s}$: RF (0.89) > CNN (0.86)

Q^{a}: RF (0.98) > CNN (0.96)

Q^{al}: RF (0.80) > CNN (0.74)

- Classes with a Small Number of Samples (<200 samples):

Both models have weaker performance in small classes:

For the Water class, both models performed almost equally (RF: 0.74 ≈ CNN: 0.73).

In class Olig-$M^{s.sh.cong}$, CNN (0.51) performed better than RF (0.39).

In class Q^{sd}, both models have almost similar performance (RF: 0.52 ≈ CNN: 0.51).

3.7.5.2 Detailed Performance Analysis

- Exceptional Performance (F1 > 0.90):

RF: Classes Q^{a} (0.98), $Pl^{silt.cong}$ (0.93), and Vegetation (0.95) showed the highest performance.

CNN: Classes Q^{a} (0.96) and Vegetation (0.91) have also performed very well.

- Poor Performance (F1 < 0.60):

RF: Showed poor performance in class Olig-$M^{s.sh.cong}$ (0.39).

CNN: Performance in class Q^{b} with an F1-Score of 0.49 has been relatively low.

3.8 Preparation of Integrated Database of SUTGMM

The developed Web-GIS system for the Server-based Unified Thematic Geological Mapping of Makran (SUTGMM) represents a significant advancement in the integration and visualization of diverse geological data. Built upon Leaflet, an open-source JavaScript library, this system provides a powerful yet user-friendly interface for displaying and analyzing the varied geological information collected and produced for the Makran region.

At its core, the WebGIS database acts as a centralized repository for a diverse array of spatial, satellite, multimedia (video and audio-visual), and documentary data, collected through advanced remote sensing techniques and extensive field surveys. The primary goal of this system is to provide geologists, researchers, and decision-makers with a comprehensive tool for visualization, analysis, and interpretation of geological results and patterns across the Makran region.

The spatial data component of the database houses satellite images from Sentinel-1, Sentinel-2, and ASTER. These imagery sources offer a wealth of information across various spectral bands, allowing for detailed analysis of surface features and composition. Complementing these satellite data are geological spectral indices that highlight specific mineral compositions and geological formations of interest.

Topographic information constitutes another important layer of the spatial database. Digital Elevation Models (DEMs), along with derived products such as slope, aspect, and hillshade, provide comprehensive data for understanding geological structures and landforms. Integrating these topographic layers with spectral data enables more precise interpretation of geological processes and formations.

A key strength of the database lies in the field data. Multimedia information meticulously collected using the specialized *Epicollect* platform includes a variety of information such as photos, audio files, videos, and other documents. These geotagged real-world data are

invaluable for validating remote sensing interpretations. Field notes and observations add a layer of expert interpretation to the raw data.

The segmentation results from the *eCognition* software and subsequent classification outputs from the Random Forest algorithm represent the analytical heart of the database. These layers provide a data-driven approach to geological mapping, marking a significant leap over traditional methods.

The database structure is carefully designed to facilitate the seamless integration of various data types. It allows for efficient querying and analysis across different data layers. The user interface, built using Leaflet in conjunction with custom JavaScript, CSS, and HTML, provides an intuitive and responsive platform for exploring the data. Users can easily switch between different data layers, perform spatial queries, and examine the relationships of various geological units with ease. The browser-based nature of the system ensures broad accessibility without the need for specialized software installation.

In summary, this WebGIS database is a powerful tool for geological research and decision-making in the Makran region. By integrating diverse data sources, utilizing advanced analytical techniques, and providing an accessible user interface, it sets a new standard for geological mapping and analysis.

3.8.1 JavaScript Programming Language

JavaScript is a high-level, versatile programming language that has become an integral part of web development and, increasingly, spatial data processing and analysis. Originally created to add interactivity to web pages, JavaScript has evolved into a powerful language capable of performing complex tasks, including spatial data processing and visualization. In the context of spatial applications, JavaScript offers several key advantages:

- Client-side processing: JavaScript runs in the user's browser, allowing for quick responses to user interactions and reducing server load for many spatial operations.

- Asynchronous operations: Through features like Promises and async/await, JavaScript can effectively handle the loading and processing of large spatial datasets without crashing the user interface.

- Support for JSON and GeoJSON: JavaScript natively supports JSON (JavaScript Object Notation), making it ideal for working with GeoJSON, a standard format for representing spatial data.

- Extensive Libraries: There are numerous JavaScript libraries specifically designed for spatial operations and mapping.

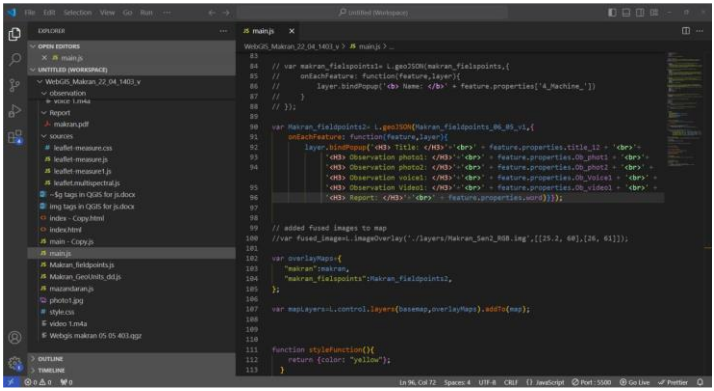

Figure 3-6. View of the Visual Studio Code programming environment and the JavaScript codes for the SUTGMM geodatabase.

With JavaScript's key spatial capabilities and data parsing and management, it can handle various spatial data formats, especially GeoJSON. It can programmatically manage spatial information and non-spatial attributes. When combined with HTML5 and CSS3, JavaScript forms a powerful combination for creating complex and responsive

applications in WebGIS. Figure 3-6 shows an example of a program written for loading, displaying, and analyzing database information.

3.8.2 Map Canvas - WebGIS Main Display Page

The primary and most prominent element of the WebGIS interface is the map canvas. This is where spatial data are rendered and displayed.

- Typically occupies most of the page space.
- Supports zooming and clicking on features.
- Ability to display multiple data layers simultaneously.
- Supports various base maps (e.g., topographic, satellite imagery, terrain maps).

In Figure 3-7, a view of the main page of the Makran Geological WebGIS is presented, which almost all the necessary tools for displaying and searching for desired information and data are included in this system.

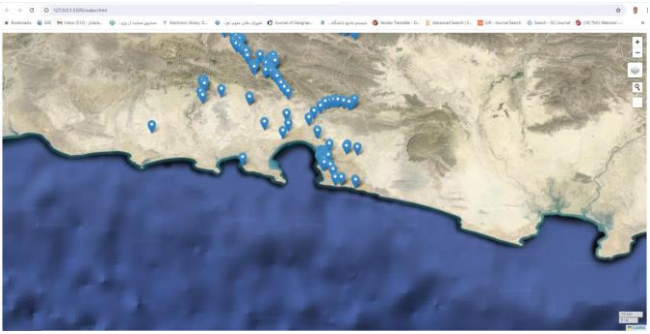

Figure 3-7. Main page of the Makran Geological WebGIS system, showing multiple georeferenced points overlaid on a satellite imagery basemap, allowing for spatial exploration and data interaction.

3.8.3 Layer Control

This interface element allows users to manage the visibility of different data layers (Figure 3-8).

- Usually presented as a list or tree structure.
- Checkboxes to toggle layer visibility.

- May include grouping of layers for different purposes.

For example, different base layers can be changed (Figure 3-9). In this project, in addition to base maps, the generated maps have also been loaded in GeoJSON format (Figure 3-10).

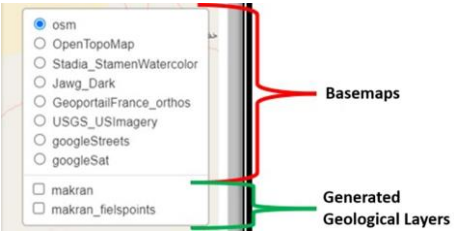

Figure 3-8. View of the layer control tool in the WebGIS environment.

Figure 3-9. A view Geoportail France Satellite Imagery layer.

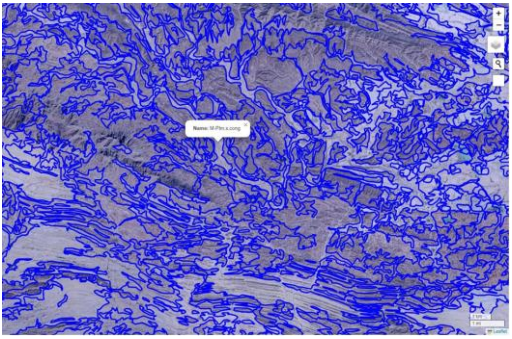

Figure 3-10. Generated geological layer with the ability to query features of each unit.

One of the prominent features of this database is the connection of various information to field surveys. This information includes photos, audio, videos, reports, and other non-spatial information that practically get spatial tagging with this system (Figure 3-11 to Figure 3-13). The following capabilities are briefly presented.

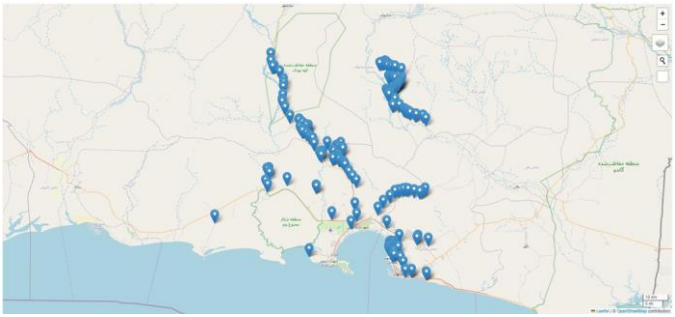

Figure 3-11. Display of the project field survey points.

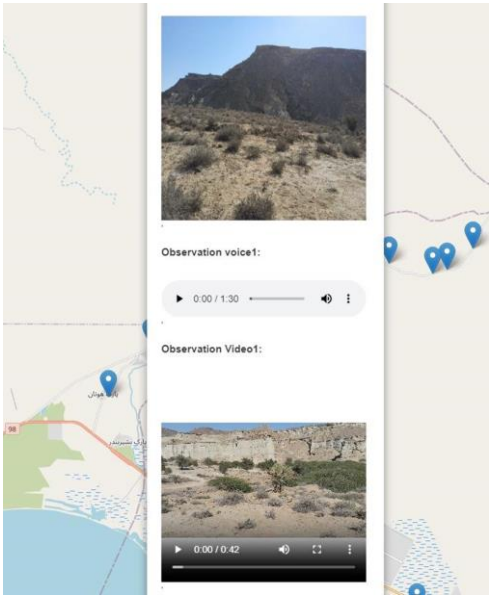

Figure 3-12. Online search and display of audio and video information for point 1168 on the map.

Figure 3-13. Online search and display of the report related to each field investigation point.

3.8.4 Navigation Controls

This plugin allows users to navigate around the map and change the view.

- Zoom in/out buttons: For changing the map scale.
- Pan controls: Often implemented as dragging the map canvas.
- Home button: To return to the initial map extent.
- Geolocation button: To center the map on the user's current location.

On the right side of the display, interactive and control capabilities are provided (Figure 3-14). At the top right, there is the ability to zoom in on the map. Below that, eight base maps are provided, allowing the user to turn on the desired base map according to their needs. This includes various satellite images and terrain maps (e.g., OpenStreetMap). Below that, a search capability is provided, enabling searching for different locations. Below the search tool, line and polygon measurement tools are provided for measuring length, perimeter, and area. Finally, the map scale tool is provided.

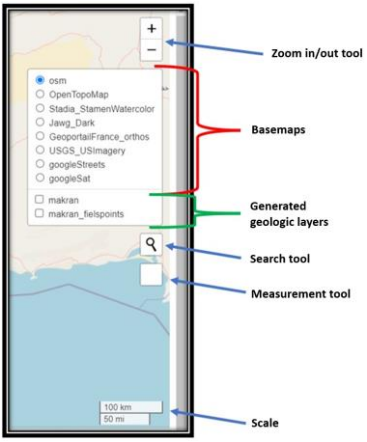

Figure 3-14. The interactive and control capabilities.

- Legend
  - Provides a key to interpret the symbology used on the map.
  - Explains the meaning of colors, shapes, and sizes used for features.
  - May be static or dynamically generated based on visible layers.
  - Often collapsible to save screen space.
- Scale Bar
  - Shows the map scale and helps users understand distances.
  - May be dynamic and update with zoom level changes.
  - Can provide multiple units (e.g., metric and imperial).
- Search Bar
  - Allows users to search for specific locations or features.
- Coordinate Display
  - Shows the coordinates of the current mouse position on the map.
  - May support multiple coordinate systems.

By integrating these features, the WebGIS system provides a comprehensive platform for users to interact with the geological data of the Makran region effectively. The combination of various data layers, interactive tools, and user-friendly design enhances the ability to analyze and interpret complex geological information.

3.9 Workflow and Protocol

The SUTGMM project represents a significant advancement in modern geological mapping, combining remote sensing, machine learning, and cloud computing to develop a unified, high-resolution geological map of the Makran region. This approach not only accelerates the mapping process but also reduces the number of personnel required to manage large-scale geological surveys. The protocol (Figure 3-15) leverages innovative technologies such as Object-Based Image Analysis (OBIA), machine learning algorithms like Random Forest (RF), and server-based cloud computing to extract and process geological data efficiently. These advances align the project with global trends in geospatial science, where modern workflows emphasize the rapid processing of complex data to produce accurate, data-driven geological maps.

This project aims to create a unified, high-resolution geological map of Makran through a multi-phase approach that integrates diverse datasets and advanced geospatial analysis techniques. The goal is to extract, process, and classify geological and geomorphological features to generate accurate and comprehensive geological outputs.

3.9.1 Phase 1: Data Acquisition and Extraction

The foundation of the project rests on the integration of multiple datasets, each contributing unique insights into the geological structure of the region. *Google Earth Engine* provides a robust platform for accessing and processing large volumes of satellite data. The project starts with the extraction of data from *Google Earth Engine*'s archive datasets, incorporating various satellite imagery, including Sentinel-1 (VV and VH polarization, 2 band images), Landsat-8 (30 m resolution, 6 band images), Sentinel-2 (10-20 m resolution, 9 band images), ASTER (VNIR, SWIR, and TIR, 14 bands), and SRTM DEM (30-m resolution). These datasets provide essential spectral, geological, and topographical information at various spatial resolutions, forming the foundation of the geological mapping.

Selected datasets for this project include:

- Sentinel-1 (VV and VH polarizations): This dataset plays a crucial role in detecting surface roughness, soil moisture content, and geomorphological variations through the use of synthetic aperture radar (SAR). The polarization data allow for the extraction of statistical features such as mean, minimum, and maximum values, which are essential for segmenting landforms and detecting subtle variations in terrain morphology.

- Sentinel-2 (10- and 20-m resolution, 9-band images): The multi-spectral capabilities of Sentinel-2 are vital for detecting vegetation indices, soil, and water bodies. Its fine spatial resolution enhances the detail of the multi-resolution, multi-scale segmentation, enabling accurate detection of surface features. The spectral bands from Sentinel-2 provide crucial information that supports the classification of geological units based on their unique spectral signatures.

- Landsat-8 (30-m resolution, 6 band images): Landsat-8 offers additional spectral diversity for geological analysis at a coarser resolution compared to Sentinel-2. The combination of mid-infrared and thermal bands contributes to identifying specific rock types and detecting thermal anomalies that may be linked to geothermal activity or subsurface processes. Despite its lower spatial resolution, Landsat-8 data remains integral for broad regional analyses.

- ASTER (VNIR, SWIR, TIR bands): With its fourteen spectral bands, ASTER data significantly enhances the identification of geological units, such as siltstone, travertine, basalt, and ignimbrite. The VNIR, SWIR, and TIR bands provide a multi-dimensional perspective on mineral composition, enabling the extraction of indices that differentiate between lithological units based on their thermal and spectral properties.

- SRTM DEM (30-m resolution): The SRTM DEM data serves as the backbone for topographical analysis, offering crucial information on landform characteristics. From slope to profile convexity and

sinuosity, the DEM data provides the essential geometrical parameters required for geomorphological and structural interpretation. This dataset helps in understanding tectonic activity, erosion patterns, and the landform analysis of the region.

3.9.2 Phase 2: Data Processing and Feature Extraction

After acquiring the datasets, the next phase involves feature extraction, where critical geological and geomorphological characteristics are derived from the various satellite imagery sources. In this step, statistical values (e.g., min, max, and mean) are extracted from Sentinel-1's polarization products to support landform segmentation. This phase also employs OBIA techniques, which are pivotal for segmenting the imagery into meaningful objects based on specific parameters such as texture, shape, and spectral properties. OBIA goes beyond pixel-based classification by considering the spatial context of features, allowing for more accurate segmentation of geological formations.

- Segmentation of Sentinel-2 Images: A multi-resolution and multi-scale segmentation process is applied to the Sentinel-2 data. This segmentation generates objects that are later classified into geological units based on spectral and textural properties. The resolution of Sentinel-2 images (10-20 m) provides the necessary detail for accurately delineating boundaries between rock units, vegetated areas, and geomorphological features.
- Shape Parameters: Shape parameters, such as asymmetry, border index, compactness, ellipticity, density, and roundness, are computed to further characterize geological segments. These parameters provide a quantifiable way to describe the geometry of geological units and are crucial for distinguishing between different rock formations, especially in regions where traditional spectral signatures might overlap (Nazari et al., 2023b; Nazari, 2024; Nazari et al., 2024a).

In this phase, a key innovation is the integration of cloud-based computing to handle vast volumes of data. This allows for faster processing times compared to desktop-based methods and enables the simultaneous extraction of multiple features from various datasets. The flexibility and scalability of cloud computing reduce the need for extensive on-site computational resources, making the process both efficient and cost-effective (Nazari et al., 2022, 2024a).

3.9.3 Phase 3: Machine Learning and Initial Classification

The extracted features from all datasets are aggregated into a comprehensive database, forming the basis for the first phase of supervised classification. In this phase, machine learning algorithms—specifically the Random Forest (RF) classifier—are employed to generate the Preliminary Geomap. The Random Forest algorithm is particularly suited for this task due to its ability to handle high-dimensional datasets and its robustness in processing heterogeneous data from multiple sources.

- Supervised Classification: The first phase of classification involves using a supervised learning model that trains the RF algorithm on labeled datasets, including previously geotagged geological formations and features. The machine learning model learns to recognize patterns in the data, which it then applies to classify segments into geological units.
- Clustering Techniques (Nazari et al., 2024a, 2024b): In parallel with the supervised classification, Fuzzy C-Means (FCM) clustering is applied to group the segmented objects into homogenous clusters based on their spectral and shape properties. This unsupervised method allows for the grouping of data points with partial membership in multiple clusters, which is useful for distinguishing between subtle variations in rock units. FCM is especially effective in geological applications where the spectral properties of adjacent rock types may overlap, making clear distinctions challenging.

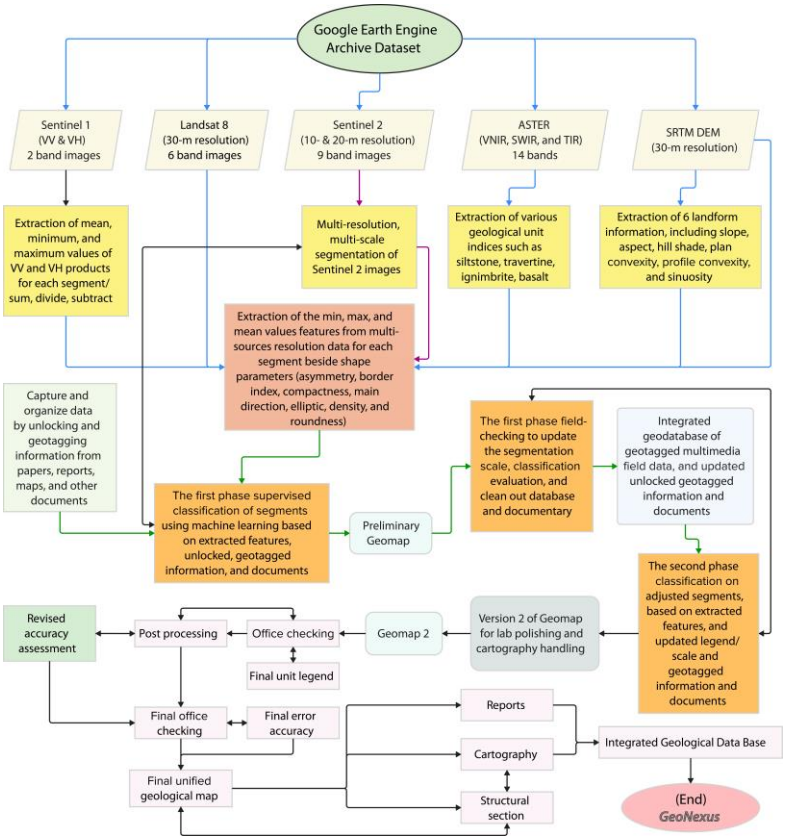

Figure 3-15. Workflow and protocol for Server-based Unified Thematic Geological Mapping of Makran (SUTGMM) using multi-source remote sensing data and machine learning. The process includes feature extraction from Sentinel-1, Sentinel-2, Landsat 8, ASTER, and SRTM DEM data, supervised classification, field-checking, and iterative refinement. The final outputs include a unified geological map, structural section, and integrated geodatabase.

3.9.4 Phase 4: Field Verification and Geodatabase Integration

Once the Preliminary Geomap is generated, the project enters the field-checking phase. This critical step involves ground-truthing the satellite-derived classifications by comparing them to actual geological formations observed in the field. Field teams collect data on rock types, mineral

compositions, and structural features, which are then used to refine the classification outputs.

- Field Verification: The first phase of field verification ensures that the segmentation and classification results align with real-world geological features. Any discrepancies are addressed by updating the segmentation scale, evaluating the classification accuracy, and cleaning out obsolete data from the geodatabase.
- Geodatabase Integration: The results from field verification are integrated into a unified geodatabase, which consolidates georeferenced field data, the unlocked trapped data (i.e., historical data from reports, maps, and documents), and satellite-derived features. This geodatabase becomes the core data repository for the project, providing a robust framework for further data refinement and future analyses (Nazari et al., 2023a, 2024a).

3.9.5 Phase 5: Iterative Refinement and Final Outputs

The second phase of classification refines the Preliminary Geomap by adjusting the segments and incorporating updated geotagged data from the field. This results in Geomap 2, which undergoes cartographic processing for lab-based polishing and cartographic handling. At this stage, the focus shifts to ensuring the highest degree of precision and consistency, particularly in how geological units are represented on the final map.

The final step—Post-Processing and Accuracy Assessment—involves a thorough accuracy assessment, where the classified segments are compared against known geological data. Post-processing includes office checks, error analysis, and revisions of the geological legend. These processes ensure that the final unified geological map is of the highest possible accuracy, suitable for research, land-use planning, and resource management applications.

The final outputs include detailed geological reports, a high-resolution geological map, and structural sections, all of which are integrated into a comprehensive GeoNexus geodatabase. This database supports the long-term monitoring and management of the region's geological resources and serves as a foundation for further research.

4 Geological and Stratigraphic Analyses

This section delves into the sedimentological characteristics and stratigraphic sequences observed within the mapped area. Each geological unit identified on the map is analyzed for its composition, depositional environment, and temporal succession. The aim is to provide a comprehensive understanding of the stratigraphic framework of the region and to relate these units to the broader tectonic and sedimentary history of the Makran region. The stratigraphy of this area records the long-term evolution of the subduction-related processes and the transition from deep marine to more terrestrial environments during different geological periods.

Detailed field mapping, combined with petrographic and micropaleontological analyses, allows for the characterization of each mapped unit in terms of its lithology, depositional environment, and diagenetic history. Moreover, absolute age dating, supplemented by paleontological data, has helped to establish a chronological framework for the sedimentary sequences. This temporal succession offers insights into the tectonic and paleoenvironmental changes that have shaped the region.

The fieldwork and sampling activities have been carefully designed and performed following the preliminary Geomap (see Chapter 3 for details), leading to a more accurate representation of the Server-Based Unified Thematic Geological Mapping of Makran (SUTGMM). The server-based approach allowed for a significant refinement in mapping workflows, enabling multi-resolution segmentation and classification of Sentinel-2, Landsat-8, ASTER, and SRTM data. These datasets formed the foundation

for identifying key sedimentological features, which were further validated and enhanced through micropaleontological, petrographic, and field-based studies.

Table 4-1. Geo-units' time table based on absolute age determination and paleontological studies.

Geo-unit	Absolute Age	Paleontological studies	Reference
Q^{a}	≤ 21.3 kyr		Dolati (2010); Gharibreza (2016)
Q^{b}	≤ 7.3 kyr		Shah-Hosseini et al. (2018); Normand (2019)
$PlPe^{c.s.si}$		Pliocene–Pleistocene	Dolati (2010)
Pl^{si}		Pliocene–Pleistocene	Dolati (2010)
$Pl^{l.si.s}$		Pliocene	Dolati (2010)
$MPl^{m.s.c}$		Middle Miocene (Serravallian) to Early Pliocene	This study
		Late Miocene–Early Pliocene	Dolati (2010)
$MPl^{m.s}$		Early Miocene (Burdigalian)–Early Pliocene	This study
		Late Miocene–Early Pliocene	Dolati (2010)
$M^{s.si}$		Early Miocene (Burdigalian)–Late Miocene (Tortonian)	This study
$M^{sh.s}$		Middle Miocene (Serravallian)–Late Miocene (Tortonian)	This study
		Middle–Late Miocene	Dolati (2010)
$M^{s.sh}$	13.7–6.0 Myr		This study
		Late Oligocene–Middle Miocene	Dolati (2010)
		Oligocene–Late Miocene	Dolati (2010)
$OlM^{s.sh.c}$		Oligocene	Dolati (2010)
$OlM^{sh.s}$		Late Oligocene	Dolati (2010)
		Early Miocene (Late Burdigalian)–Middle Miocene (Early Langhian)	This study

Key geological units were revised and reclassified based on their spectral, textural, and morphological features. The combination of satellite imagery, field observations, and laboratory analyses has allowed for the identification of depositional sequences spanning from the Oligocene to the present (Table 4-1 and Figure 4-1). Additionally, paleontological

dating and petrographic examinations of rock samples have refined the temporal succession of these units, allowing for more accurate age determinations and stratigraphic correlations across the mapped area. The output of this comprehensive analysis forms the basis for version 2 of the GeoMap, with final refinements captured in the GeoNexus database.

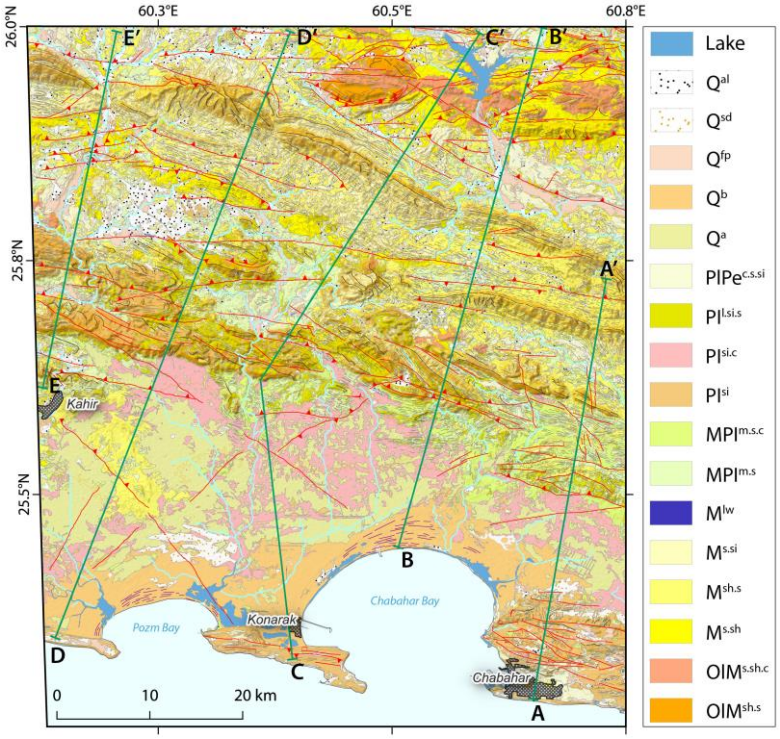

Figure 4-1. Server-based unified thematic geological units of the AOI. Solid green lines highlight the trajectory of the structural cross-sections in Chapter 5.

The output of this comprehensive analysis forms the basis for version 2 of the GeoMap, with final refinements captured in the GeoNexus database. Additionally, the SUTGMM project has published nine detailed 1:50,000 geological sheets (Figure 4-2), including Ab Sard, Chabahar, Gor, Gurdim, Kahir, Konarak, Kuh-e-kand Koruch, Park Bala, and Zirdan. These maps

offer an unparalleled level of detail, capturing essential geological features across the Area of Interest (AOI). Each sheet is designed to facilitate in-depth geological analysis at a scale of 1:50,000, ensuring the precise representation of stratigraphic units, structural elements, and surface processes. The high resolution and accuracy of these maps, derived from multi-source remote sensing data and rigorous field validation, provide a valuable resource for both academic research and practical applications in geology, tectonics, and environmental studies. These sheets are integral to understanding the geological evolution of the region, with each map sheet divided into nine distinct 1:150,000 segments for ease of interpretation and use in both research and industry.

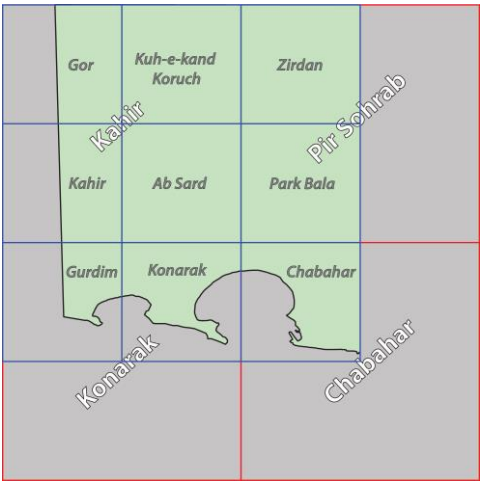

Figure 4-2. Mapping framework for the GeoNexus project (SUTGMM) in the Makran region.The green polygon marks the Area of Interest (AOI) for the Server-Based Unified Thematic Geological Mapping of Makran (SUTGMM) project. The solid grey rectangles with red outlines represent the extent of the previously published 1:100,000 geological maps that cover the study area. The rectangles with blue outlines correspond to the nine 1:50,000 geological sheets published as part of the GeoNexus geodatabase (SUTGMM), which include Ab Sard, Chabahar, Gor, Gurdim, Kahir, Konarak, Kuh-e-kand Koruch, Park Bala, and Zirdan.

4.1 $OlM^{sh.s}$ Unit (Late Oligocene Shale and Sandstone)

The $OlM^{sh.s}$ Unit represents the oldest geological formation within the study area, dating to the late Oligocene. The unit is represented by 54 mapped polygons within the study area. These outcrops vary in size, reflecting the complex nature of the terrain and the impact of tectonic processes. The individual areas of these outcrops range from approximately 0.0136 sq km to 14.64 sq km (OBJECTID_1: 6108). The cumulative area covered by the $OlM^{sh.s}$ Unit is ~ 38 sq km.

This 350-m thick unit is characterized by light grey to olive shales interbedded with moderate to thick-bedded silty sandstones. These rocks have undergone significant folding and faulting, reflecting the tectonic activities that have shaped the region.

The $OlM^{sh.s}$ unit consists predominantly of:

- Shale: Light grey to olive in color, these shales are fine-grained and display fissility. They suggest deposition in a relatively low-energy marine environment.
- Silty Sandstone: These are moderate to thick-bedded, ranging from 10 to 120 cm (Dolati, 2010) in thickness. The sandstones are coarse to fine-grained, green to dark grey, and often display tabular bedding planes. They are commonly volcaniclastic and lack calcareous clasts or cement.

4.1.1 Stratigraphy and Age

The unit is assigned to the late Oligocene based on biostratigraphic data, including nannofossils and foraminifera. Samples have yielded ages corresponding to the Chattian stage (approximately 27–23 Ma BP), with some samples indicating ages up to the Rupelian–Chattian boundary (30–27.5 Ma BP) (Dolati, 2010).

The lower boundary of the $OlM^{sh.s}$ Unit is typically obscured by thrust faults, making it difficult to observe directly. The upper boundary

transitions into overlying shale-dominated turbidite successions, indicating a shift from inner fan to more distal depositional environments.

4.2 $OlM^{s.sh.c}$ Unit (Oligocene Shale, Sandstone, and Conglomerate)

The $OlM^{s.sh.c}$ Unit represents a geological formation within the study area, dating to the Oligocene with a thickness of ~ 250 m. This unit is characterized by light grey thick-bedded sandstones with distinctive sedimentary features, interbedded with light grey to olive shales, and microconglomerates containing calcite veins and pyrite remnants in faulted zones. The unit exhibits significant tectonic deformation, reflecting the complex geological history of the region.

The $OlM^{s.sh.c}$ Unit is an Oligocene-aged geological formation within the study area, characterized by a sequence of interbedded sandstones, shales, and conglomerates. This unit is also equivalent to Pirdan Unit (e.g., Dolati, 2010); however, the unit exhibits distinct lithological features and structural complexities that have been refined and distinguished in our mapping through server-based unified thematic geological mapping. While previous studies have grouped similar formations under broader units, our detailed mapping efforts have identified the $OlM^{s.sh.c}$ Unit as a separate entity.

The unit is represented by 260 mapped polygons within the study area. The individual areas of these outcrops vary greatly, from as small as 0.0008 sq km to as large as 76.36 sq km. Notable large outcrops include OBJECTID_1: 6359 (76.36 sq km), 6305 (28.31 sq km), and 6328 (29.48 sq km). The cumulative area covered by the $OlM^{s.sh.c}$ Unit is ~ 350 sq km.

The $OlM^{s.sh.c}$ Unit comprises:

- Sandstone: Light grey, thick-bedded sandstones with notable sedimentary structures such as casts and worm burrows on bed tops. The sandstones are volcaniclastic, lacking calcareous clasts or cement, and exhibit features like graded bedding and ripple marks, indicative of deposition by turbidity currents.

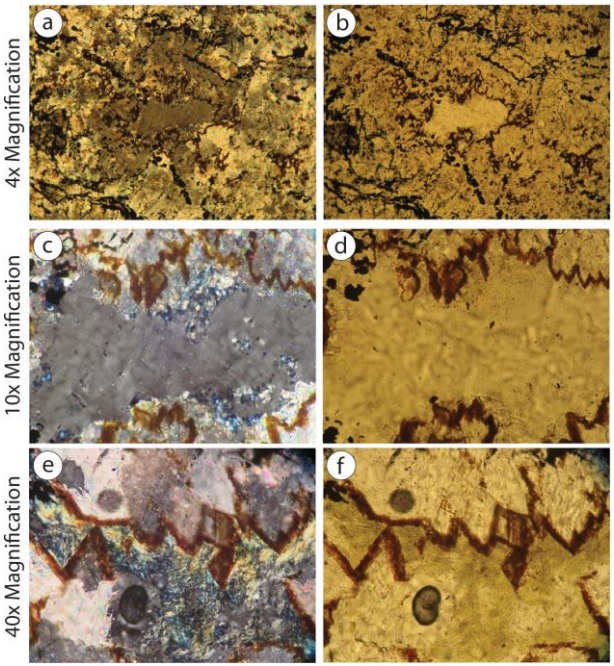

Figure 4-3. Photomicrographs of Sample 24M-42P in cross-polarized light (XPL) and plane-polarized light (PPL) at varying magnifications. Panels a, c, and e are in XPL, and panels b, d, and f are in PPL. The sample is identified as listvenite, a highly altered or metamorphosed rock resulting from hydrothermal alteration of ultramafic rocks.

- Shale: Moderate-bedded, light grey to olive shales interbedded with the sandstones, suggesting fluctuations in depositional energy and sediment supply.
- Microconglomerate: Occurs within the unit, containing clasts cemented by calcite veins. In faulted zones, pyrite remnants are observed, pointing to post-depositional mineralization processes.
- Calcite veins and pyrite remnants: The presence of calcite veins and pyrite in faulted parts indicates fluid flow and hydrothermal activity associated with tectonic movements.

4.2.1 Stratigraphy and Age

The $OlM^{s.sh.c}$ Unit is assigned an Oligocene age based on stratigraphic position and correlation with similar units identified in previous studies. This unit overlies the older $OlM^{sh.s}$ Unit and is succeeded by younger formations. The transition from thick-bedded sandstones to interbedded shales and conglomerates reflects changes in depositional environments and sediment supply during the Oligocene.

4.3 $M^{s.sh}$ Unit (Oligocene–Late Miocene Shale and Sandstone)

The $M^{s.sh}$ Unit represents an Oligocene to late Miocene geological formation within the study area, characterized by a complex assemblage of sedimentary rocks with volcanic influences. This unit, with a thickness of ~ 200 m, comprises grey, moderate to thick-bedded volcanogenic sandstone transitioning to limy sandstone, alternating with greenish-grey to bluish shale. On weathered surfaces, the rocks exhibit a brown coloration, while fresh surfaces range from light brown to greenish hues. The $M^{s.sh}$ Unit is notable for its folded and faulted turbiditic flysch deposits, reflecting a dynamic tectonic setting during its formation.

The unit is represented by 516 mapped polygons within the study area. The individual areas of these outcrops vary greatly, from as small as 0.00017 sq km to as large as 123.49 sq km. Notable large outcrops include OBJECTID_1: 4488 (123.49 sq km), 4486 (79.41 sq km), and 4736 (72.74 sq km). The cumulative area covered by the unit is ~ 822 sq km.

The $M^{s.sh}$ Unit displays a diverse lithological composition, indicative of varying depositional environments and sediment sources influenced by volcanic activity.

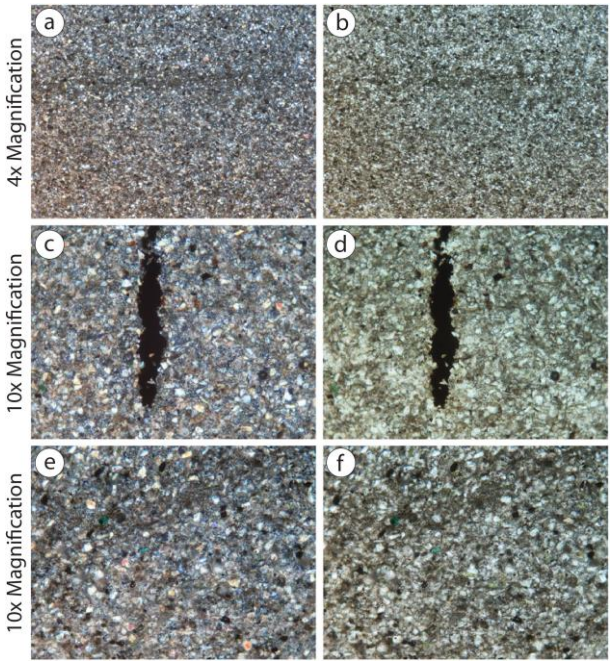

Figure 4-4. Photomicrographs of Sample 24M-25F in XPL (panels a, c, and e) and PPL (panels b, d, and f) at varying magnifications. This sample is identified as sandy-silty limestone, detrital, ferruginous.

4.4 $M^{sh.s}$ Unit (Middle to Late Miocene Shale and Siltstone)

The $M^{sh.s}$ Unit represents a sedimentary sequence deposited during the middle to late Miocene. Like Ms.sh Unit, this unit lies in Peersohrab Unit (Dolati, 2010), but exhibits different characteristics to distinct it from Ms.sh Unit. This unit is characterized by interbedded shales, siltstones, sandstones, and volcaniclastics, reflecting a dynamic depositional environment influenced by both sedimentary and volcanic processes. This report provides a comprehensive analysis of the $M^{sh.s}$ Unit, integrating petrographic and micropaleontological data from various samples to elucidate its lithological characteristics, fossil content, depositional environments, and chronological framework.

The unit is represented by 1305 mapped polygons within the study area. The individual areas of these outcrops vary greatly, from as small as 0.00047 sq km to as large as 256.96 sq km. Notable large outcrops include OBJECTID_1: 5164 (256.96 sq km), 1467 (56.81 sq km), and 5102 (36.22 sq km). The cumulative area covered by the $M^{sh.s}$ Unit is ~ 1263 sq km.

The $M^{sh.s}$ Unit, with a thickness of ~ 200 m, comprises predominantly clastic sedimentary rocks with significant volcanic input. The lithology includes calcareous siltstones, argillaceous limestones, tuffaceous sandstones, volcanic sandstones, and graywackes. The stratigraphy indicates alternating layers of marine sediments and volcanic materials, suggesting episodic volcanic activity during sedimentation.

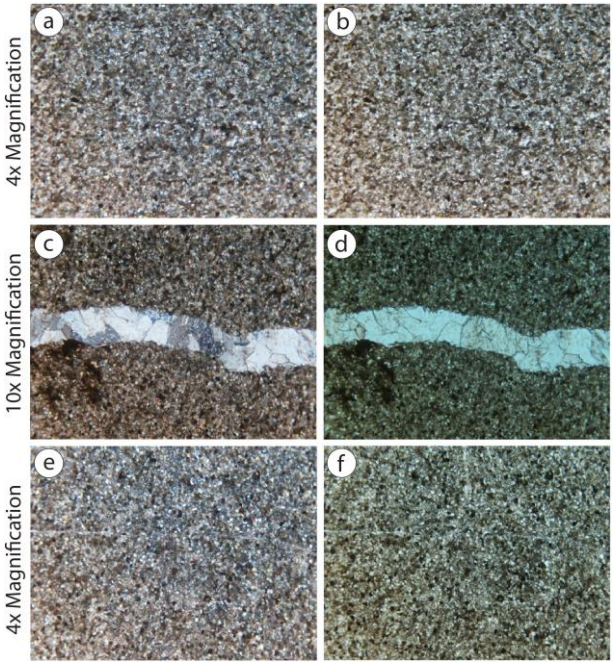

Figure 4-5. Photomicrographs of Sample 24M-23F in XPL (panels a, c, and e) and PPL (panels b, d, and f) at varying magnifications. This sample is identified as calcareous Siltstone to Argillaceous Limestone.

4.4.1 Age and Correlation

The micropaleontological analyses indicate that the $M^{sh.s}$ Unit includes sediments ranging from the early Miocene (Burdigalian) to the late Miocene (Tortonian). While the unit is defined as middle to late Miocene, the presence of early Miocene fossils suggests that it may encompass older strata or that there is a need to reassess the unit's age boundaries.

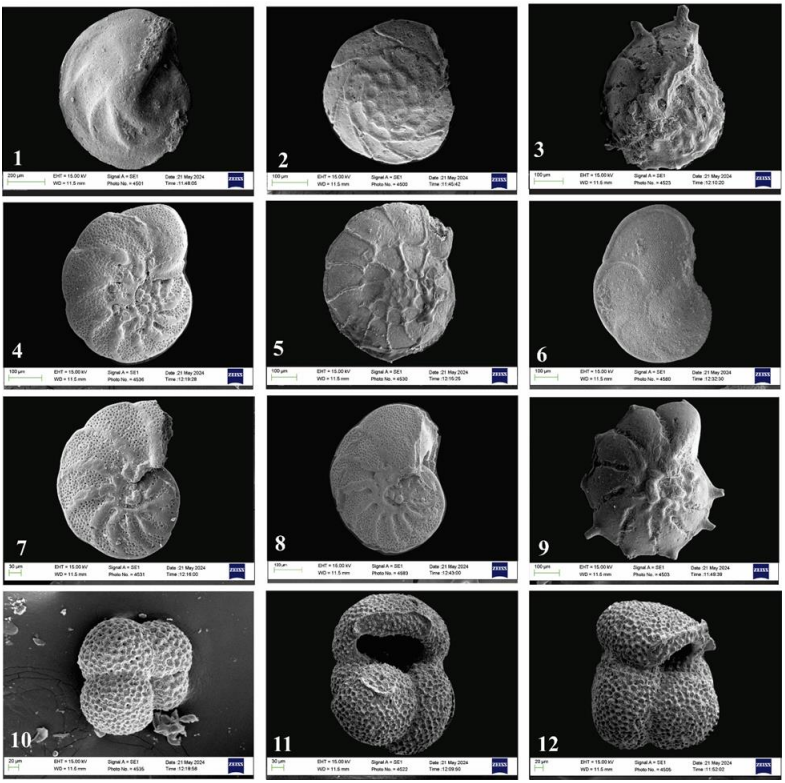

Figure 4-6. Scanning Electron Microscope (SEM) images of micropaleontological species of Sample 24M-04W (Plate 2), showcasing their morphological details. 1) *Lenticulina inornate;* 2) *Ammonia sp. cf. A. asanoi*; 3) *Ammonia beccarii dentata*; 4) *Cibicides sp.*; 5) *Ammonia tochigiensis*; 6) *Globorotalia archeomenardii*; 7) *Nonion costiferum*; 8) *Nonion costiferum*; 9) *Ammonia beccarii dentata*; 10) *Globigernella obesa*; 11) *Globigerinoides subquadratus*; 12) *Globoquadrina sp. cf. G. venezuelana*.

4.5 $M^{s.si}$ Unit

The $M^{s.si}$ is a ~200-m-thick unit, characterized by red-brown, thick-bedded, cleaved, and cliff-forming sandy siltstone to sandstone, bearing bituminous and iron oxide materials. This unit forms prominent cliffs in the study area due to its lithological properties and mechanical strength. The presence of iron oxide contributes to the reddish-brown coloration, while bituminous materials indicate organic content within the sedimentary rocks.

The unit is represented by 947 mapped polygons within the study area. The individual areas of these outcrops vary greatly, from as small as 0.0042 sq km (OBJECTID_1: 6486) to as large as 34.77 sq km (OBJECTID_1: 6885). The cumulative area covered by the $M^{s.si}$ Unit is ~ 710 sq km.

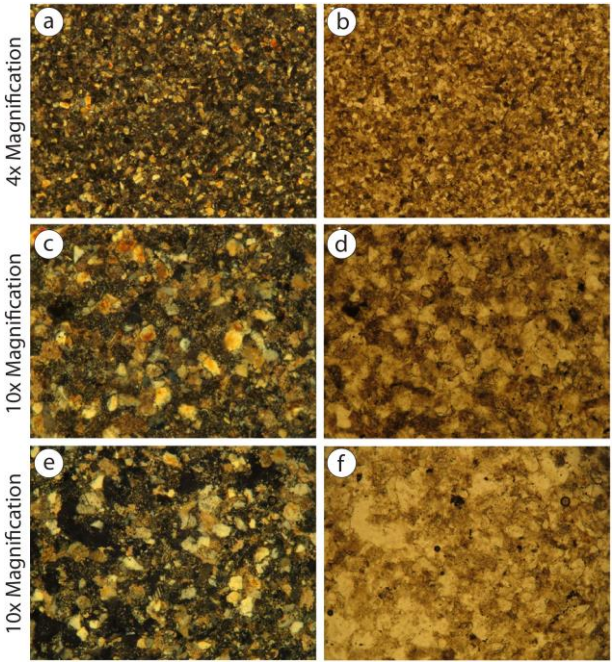

Figure 4-7. Photomicrographs of Sample 24M-51P in XPL (panels a, c, and e) and PPL (panels b, d, and f) at varying magnifications. This sample is identified as hybrid sedimentary–volcanic rock.

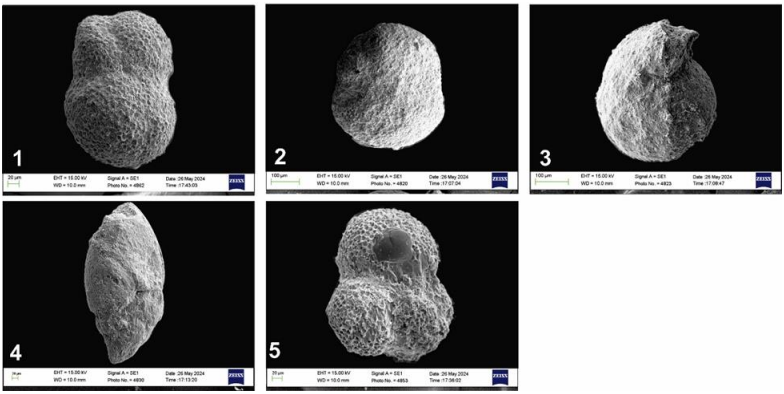

Figure 4-8. SEM images of micropaleontological species of Sample 24M-48W (Plate 17), showcasing their morphological details. 1) *Globigerinoides immaturus*; 2) *Globigerinoides triloba*; 3) *Cibicides sp.*; 4) *Bulimina pyrula*; 5) *Globigerinoides immaturus*.

4.5.1 Age and Correlation

The micropaleontological analyses suggest that the $M^{s.si}$ Unit encompasses sediments from the early Miocene (late Burdigalian) to middle Miocene (early Langhian), consistent with the age defined in the final map legend. However, sample 24M-46W indicates a broader age range extending to the late Miocene (Tortonian), which is not entirely consistent with the unit's defined age. Similarly, the uncertain age of sample 24M-50W suggests possible stratigraphic complexities within the unit.

4.6 $MPl^{m.s}$ Unit

The ~150-m-thick $MPl^{m.s}$ Unit comprises sedimentary rocks predominantly of late Miocene to early Pliocene, characterized by sandstones, siltstones, mudstones, and occasional hybrid rocks exhibiting both sedimentary and volcanic characteristics. These rocks are significant in the geological framework of the study area due to their diverse lithological properties and depositional histories, reflecting a complex interplay between clastic and volcanic inputs.

The unit is represented by 912 mapped polygons within the study area. The individual areas of these outcrops vary greatly, from as small as 0.0006 sq km (OBJECTID_1: 10455) to as large as 24.34 sq km (OBJECTID_1: 992). The cumulative area covered by the MPlm.s Unit is approximately 640 sq km.

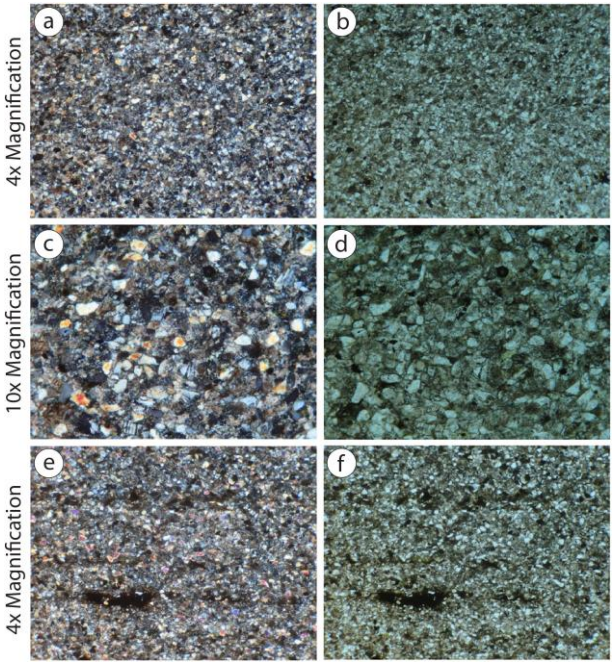

Figure 4-9. Photomicrographs of Sample 24M-21F in XPL (panels a, c, e) and PPL (panels b, d, f) at magnifications of 4x (a, b, e, f) and 10x (c, d). This sample is identified as volcanic sandstone to tuffaceous sandstone.

4.6.1 Age and Correlation

The micropaleontological analyses generally support the late Miocene to early Pliocene of the $MPl^{m.s}$ Unit. However, some samples, such as Sample 24M-21F and Sample 24M-28F, suggest an age of probably Oligocene–Miocene based on lithology and fossil content, which is older than the unit's defined age. Similarly, Sample 24M-54P indicates an early Miocene (Aquitanian–Burdigalian) age. Sample 24M-29W indicates a middle

Miocene (early Langhian) age, which is inconsistent with the unit's defined age, as well. These discrepancies suggest that parts of the unit may include older strata or reworked sediments, highlighting the complexity of the geological history and the need for careful stratigraphic analysis.

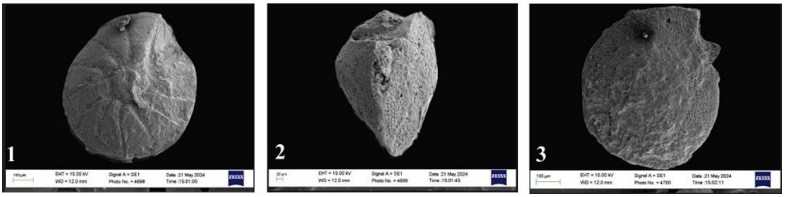

Figure 4-10. SEM images of micropaleontological species of Sample 24M-27W (Plate 11), showcasing their morphological details. 1) *Ammonia gaimardi*; 2) *Heterolepa dutemplei*; 3) *Heterolepa dutemplei*.

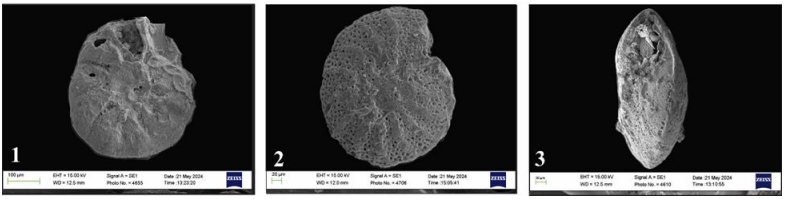

Figure 4-11. SEM images of micropaleontological species of Sample 24M-34W (Plate 13), showcasing their morphological details. 1) *Ammonia umbonate*; 2) *Nonion scapha*; 3) *Nonion sp*.

4.7 $MPl^{m.s.c}$ Unit (Late Miocene–Early Pliocene Sandstone and Microconglomerate)

The $MPl^{m.s.c}$ Unit, with ~ 250 m thickness, represents a late Miocene to early Pliocene geological formation within the study area, characterized by alternating sequences of greenish to light grey, thin to moderately bedded marls (argillaceous rocks), and red-brown, moderately to thick-bedded sandstones and microconglomerates (Figure 4-12). The unit features cleavages and macrofossils, with sandy olistoliths particularly concentrated in the lower part. This sedimentary package reflects a diverse depositional environment influenced by both sedimentary and

tectonic processes, with unit thickness reaching ~ 250 m. The rocks exhibit variations in color and texture between weathered and fresh surfaces, reflecting their compositional diversity and diagenetic history.

The unit is represented by 654 mapped polygons within the study area. The individual areas of these outcrops vary greatly, from as small as 0.0082 sq km (OBJECTID_1: 1310) to as large as 69.45 sq km (OBJECTID_1: 1483). The cumulative area covered by the $MPl^{m.s.c}$ Unit is ~ 410 sq km.

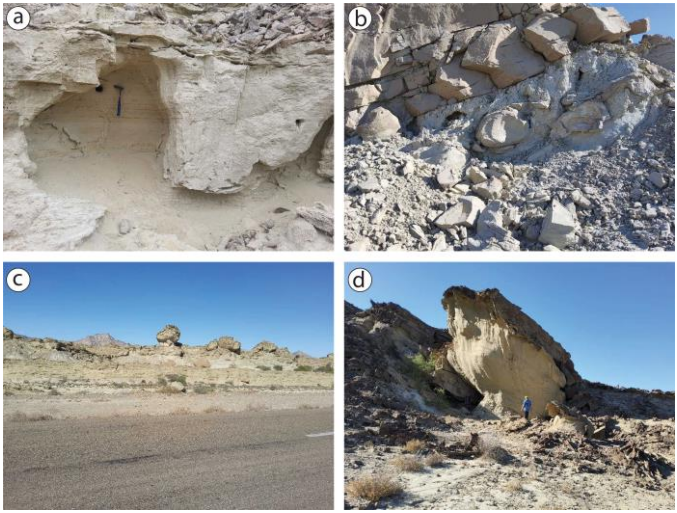

Figure 4-12. a) Outcrop at location P002 showing thinly bedded argillaceous rock layers of the $MPl^{m.s.c}$ Unit's. b) Location P031 displaying large olistolith blocks embedded within the sedimentary sequence. c, d) Prominent hoodoo morphology at location P032 (c) and P033 (d), showcasing the differential weathering and textural contrasts between weathered and fresh surfaces in the MPlm.s.c Unit's sandstone beds.

4.7.1 Age and Correlation

The $MPl^{m.s.c}$ Unit is defined as spanning from the lower Miocene to early Pliocene. The integrated micropaleontological analyses generally support this age assignment, with the majority of samples falling within this range. Samples 24M-10W and 24M-15W contain foraminiferal assemblages consistent with middle Miocene to early Pliocene age, including key index

species such as *Orbulina suturalis* and *Orbulina universa*. However, discrepancies arise with Samples 24M-11W and 24M-39W.

The $MPl^{m.s.c}$ Unit records a complex depositional history involving the interplay of volcanic activity, clastic sedimentation, carbonate production, and marine processes. Environments range from volcaniclastic settings influenced by active volcanism to shallow marine carbonate platforms and mixed clastic-carbonate coastal zones. Diagenetic alterations observed in the rocks, including neomorphism, micritization, and cementation, further reflect post-depositional processes that have modified the original sediments.

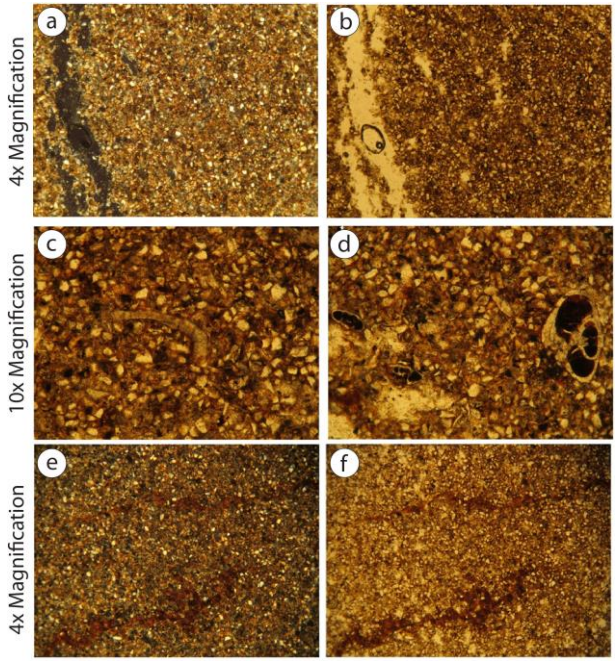

Figure 4-13. Photomicrographs of Sample 24M-8P in XPL (panels a and e) and PPL (panels b, c, d, and f) at varying magnifications. This sample is identified as very fine-grained calcareous sandstone.

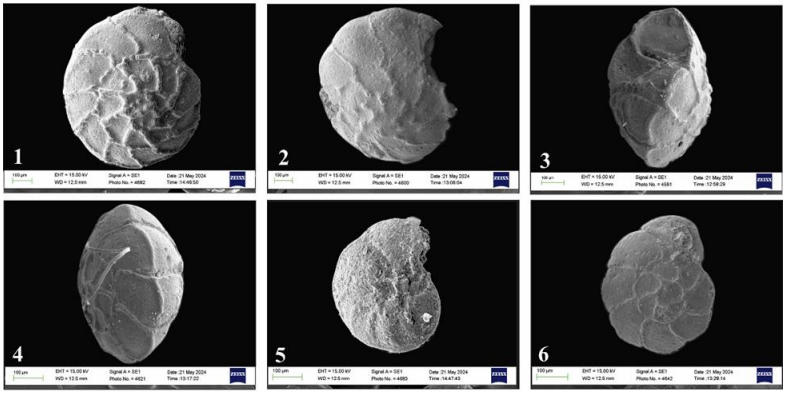

Figure 4-14. SEM images of micropaleontological species of Sample 24M-10W (Plate 4), showcasing their morphological details. 1) *Ammonia tochigiensis*; 2) *Ammonia stachi*; 3) *Ammonia gaimardi*; 4) *Ammonia marhausai*; 5) *Nonion sp.*; 6) *Ammonia annectens*.

4.8 Pl^{si} Unit (Pliocene to Pleistocene Siltstones and Argillic Deposits)

This unit comprises creamy mud, thick-bedded siltstone, and sandy siltstone with greenish to light grey-blue gypseous argillic deposits (Figure 4-15). It represents sedimentary sequences deposited during the Pliocene to Pleistocene period. Detailed petrographic and micropaleontological analyses have been conducted to understand the lithology, depositional environments, and age determinations within this unit. The unit has thickness of ~ 100 m.

The Pl^{si} Unit is represented by 310 mapped polygons within the study area. These polygons range in size from as small as 0.0054 sq km to as large as 94.08 sq km. Notable large outcrops include OBJECTID_1: 244 (94.08 sq km), 2409 (65.40 sq km), and 2366 (53.23 sq km). The cumulative area covered by the Pl^{si} Unit is ~ 399 sq km.

Figure 4-15. Tidal cross-bedding observed in the Pl^{si} Unit at location P014.

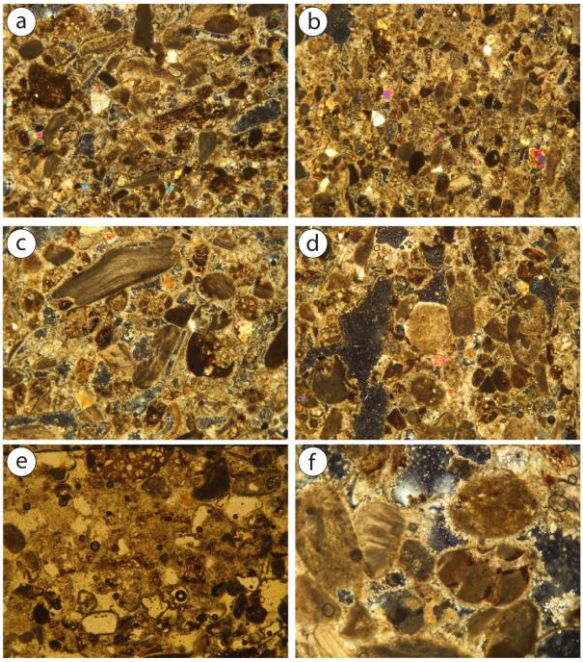

Figure 4-16. Photomicrographs of Sample 24M-1F in XPL (panels a, c, b, d, and f) and PPL (e) at a magnification of 4x. This sample is identified as limestone with intrabioclastic grainstone to rudstone with minor quartz grains microfacies.

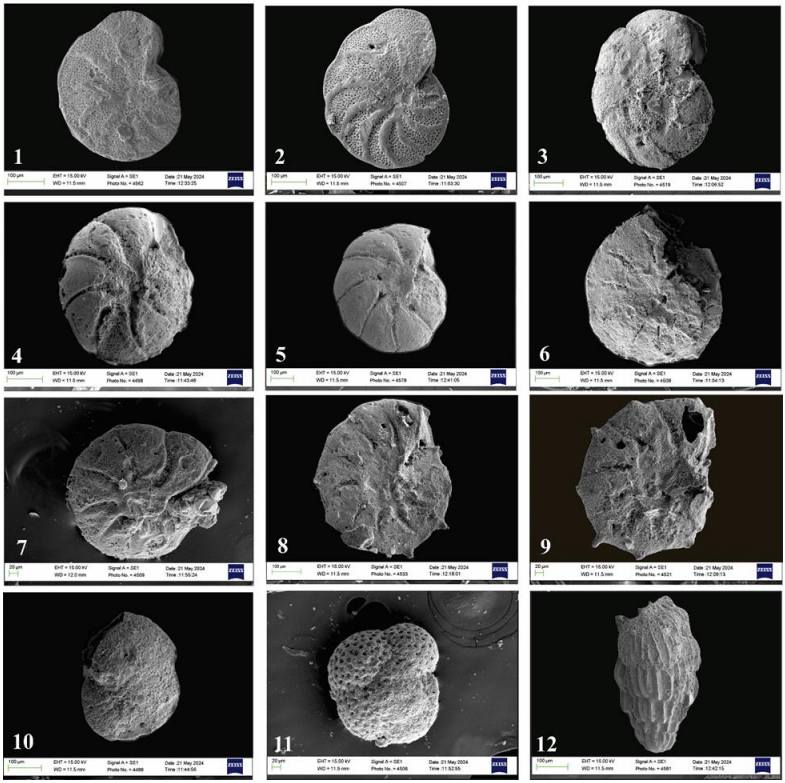

Figure 4-17. SEM images of micropaleontological species of Sample 24M-3W (Plate 1), showcasing their morphological details. 1) *Nonion costiferum*; 2) *Nonion costiferum*; 3) *Ammonia schroeteriana*; 4) *Ammonia sp. cf. A. asanoi*; 5) *Cibicides sp. cf. C. refulgens*; 6) *Ammonia beccarii bagnensis*; 7) *Ammonia beccarii dentata*; 8) *Ammonia beccarii dentata*; 9) *Ammonia beccarii dentata*; 10) *Nonion scapha*; 11) *Globigerinoides immaturus*; 12) *Uvigerina multicostata*.

4.8.1 Age and Correlation

The Pl^{si} Unit is defined as spanning from the Pliocene to Pleistocene. However, the analyses of the samples present discrepancies. Samples 24M-1F, 24M-2F, 24M-35F, and 24M-36F have fossil assemblages indicating an early Miocene (Aquitanian-Burdigalian) age, which is significantly older than the unit's assigned Pliocene to Pleistocene age. Sample 24M-3W suggests an age range of late Miocene to Pliocene,

slightly older than the unit's defined age. These discrepancies suggest that the samples may have been collected from older strata within the mapped extent of the Pl^{si} Unit, or there may be complexities in the stratigraphic relationships, such as unconformities, faulting, or folding that have juxtaposed older rocks against younger units, or reworking of older sediments into younger deposits may have occurred. It can also suggest that there may be inaccuracies in field mapping or unit assignments.

4.9 $Pl^{si.c}$ Unit (Pliocene White to Buff Argillic Deposits and Sandy Siltstones)

The $Pl^{si.c}$ Unit is characterized by white to buff, stratified, thick-bedded, almost horizontal argillic loose deposits interbedded with thin gypsum layers. It includes sandy siltstone to microconglomerate with a silty matrix, indicative of deposition in tidal to supratidal zones. This unit forms distinctive landforms locally referred to as the "Martian Mountains." The measured thickness of this unit is ~ 100 m.

The unit is represented by 444 mapped polygons within the study area. The individual areas of these outcrops vary widely, ranging from as small as 0.0041 sq km to as large as 199.87 sq km. Notable large outcrops include OBJECTID_1: 4180 (199.87 sq km), 4002 (128.70 sq km), and 4168 (118.85 sq km). The cumulative area covered by the $Pl^{si.c}$ Unit is ~ 703 sq km.

4.9.1 Age and Correlation

The $Pl^{si.c}$ Unit is assigned a Pliocene age based on its stratigraphic position and regional correlation with similar deposits. The lack of precise micropaleontological data limits the ability to refine the age within the Pliocene.

4.10 $Pl^{l.si.s}$ Unit (Pliocene Shale and Volcanosedimentary Sandy Tuff)

The $Pl^{l.si.s}$ Unit is characterized by an alternation of grey to brown shales of moderate bedding thickness and thin beds of volcanosedimentary sandy tuff. Towards the upper part of the sequence, the unit is sealed by sandstone layers. This lithological assemblage reflects a complex interplay between sedimentary and volcanic processes during the Pliocene. The measured thickness of the unit is ~ 100 m.

The unit is represented by 321 mapped polygons within the study area. The individual areas of these outcrops vary significantly, from as small as 0.0657 sq km to as large as 25.50 sq km. Notable large outcrops include OBJECTID_1: 2024 (25.50 sq km), 1747 (25.27 sq km), and 1991 (17.57 sq km). The cumulative area covered by the $Pl^{l.si.s}$ Unit is ~ 254 sq km.

The $Pl^{l.si.s}$ Unit predominantly consists of grey to brown shales interbedded with thin layers of sandy tuffs of volcanic origin. The shales exhibit moderate bedding thickness, suggesting relatively consistent depositional conditions over time. These fine-grained sedimentary rocks are indicative of low-energy environments where clay and silt-sized particles settle out of suspension.

The sandy tuff layers represent episodes of volcanic activity, during which pyroclastic materials were deposited within the sedimentary basin. These layers are thin, suggesting that volcanic events were relatively brief or that the influx of volcanic material was limited.

Towards the upper part of the unit, the sequence is sealed by sandstone layers. The sandstones are likely medium to coarse-grained, indicating a shift to higher energy depositional conditions capable of transporting and depositing larger sediment particles. This upward transition reflects a significant change in the depositional environment.

The alternation of shales and sandy tuffs suggests a depositional setting influenced by periodic volcanic activity within a predominantly sedimentary basin. The shales indicate quiet, low-energy conditions,

possibly in a deep marine or lacustrine environment, while the sandy tuffs reflect volcanic eruptions depositing ash and pyroclastic material.

The presence of sandstone sealing the unit implies a shift to higher energy conditions, such as a regression leading to shallower water depths or an increase in sediment supply from terrestrial sources. This could be due to tectonic uplift, climatic changes, or sea-level fluctuations affecting sedimentation patterns.

4.10.1 Age and Correlation

The $Pl^{l.si.s}$ Unit is assigned a Pliocene age based on its stratigraphic position and correlation with regional geological studies, particularly referencing Dolati (2010). The absence of micropaleontological samples limits the ability to refine the age further within the Pliocene. The unit's characteristics are consistent with other Pliocene deposits in the region, supporting this age assignment.

4.11 $PlPe^{c.s.si}$ Unit (Pliocene to Pleistocene Sediments)

The $PlPe^{c.s.si}$ Unit encompasses a significant assemblage of sedimentary rocks deposited during the Pliocene to Pleistocene. This unit is characterized by a diverse lithology, including red-brown, thick-bedded conglomerates and buff to white, thin-bedded siltstones and silty sandstones. The measured thickness of the unit is approximately 150 m. These sediments reflect dynamic depositional environments influenced by climatic fluctuations, tectonic activities, and sea-level changes during the Pliocene to Pleistocene.

The unit is represented by 861 mapped polygons within the study area. The individual areas of these outcrops vary greatly, from as small as 0.1747 sq km to as large as 97.56 sq km. Notable large outcrops include OBJECTID_1: 10001 (97.56 sq km), 9981 (85.81 sq km), and 9582 (65.12 sq km). The cumulative area covered by the PlPec.s.si unit is ~ 950 sq km.

The lithological composition of the $PlPe^{c.s.si}$ Unit is complex, featuring both coarse-grained and fine-grained clastic sediments. The conglomerates

are notable for their red-brown color and thick bedding. They consist of approximately 50% clasts, predominantly sandstone, which are well-rounded to weakly rounded. The clasts vary in size and are poorly sorted (bad sorting), indicating rapid deposition likely associated with high-energy environments such as proximal alluvial fans. The matrix of these conglomerates is composed of buff silty sand, contributing to the heterogeneous and polymictic nature of the rock, which suggests multiple source areas and transport paths. These conglomerates are consolidated, reflecting significant lithification processes.

Interbedded with the conglomerates are thin-bedded siltstones and silty sandstones that are buff to white in color. These fine-grained sediments have an argillic texture, indicating a significant clay component, and are generally unconsolidated, suggesting minimal diagenesis. They were likely deposited in lower-energy settings such as floodplains, overbank areas, or distal alluvial environments, where finer sediments could settle.

The unit also includes unconsolidated cyclic alluvial fan deposits with caliche zones. These deposits contain weakly rounded clasts, reflecting limited transport from their source areas. The cyclic nature of these deposits suggests episodic sedimentation events, possibly linked to climatic fluctuations or tectonic uplift, which periodically increased sediment supply. The presence of caliche zones indicates periods of landscape stability and soil formation under arid to semi-arid conditions, pointing to significant climatic influence on sedimentation processes.

Additionally, fine-grained deposits are found trapped in saddle areas near marine shores. These sediments indicate deposition in low-energy environments, potentially influenced by marine processes or protected settings, and may reflect occasional marine incursions due to sea-level changes during the Pliocene to Pleistocene.

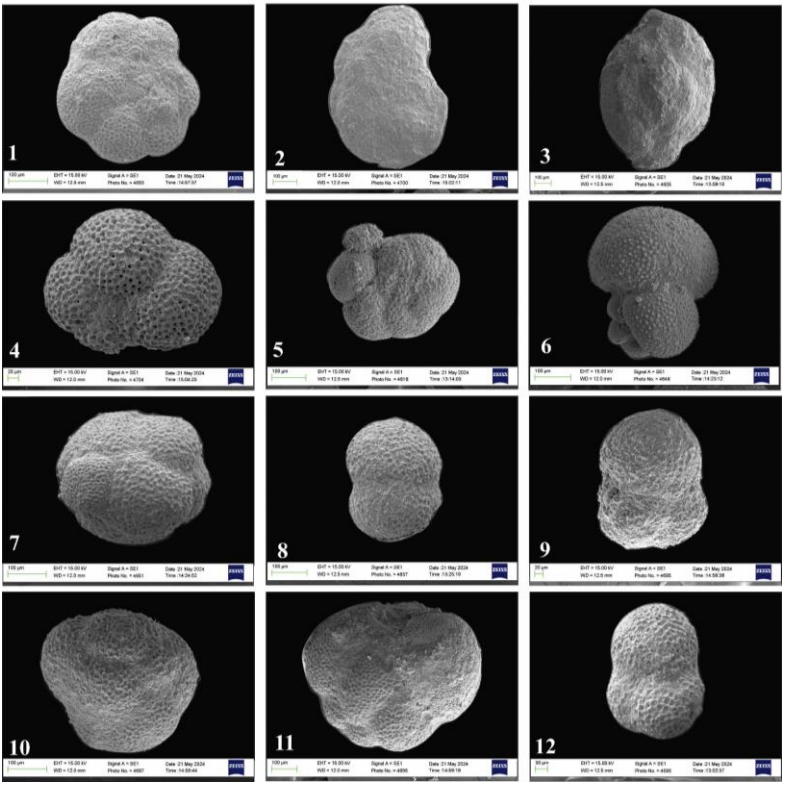

Figure 4-18. SEM images of micropaleontological species of Sample 24M-18W (Plate 7), showcasing their morphological details. 1) *Cibicides sp.*, *Globigerinoides immaturus*; 2) *Cibicides sp.*; 3) *Quinqueloculina sp.*; 4) *Paragloborotalia obesa*; 5) *Globorotalia siakensis*; 6) *Globigerinoides immaturus*; 7) *Catapsydrax dissimilis*; 8) *Globigerinoides immaturus*; 9) *Globigerinoides immaturus*; 10) *Catapsydrax dissimilis*; 11) *Catapsydrax dissimilis*; 12) *Globigerinoides immaturus*.

4.11.1 Age and Correlation

The $PlPe^{c.s.si}$ Unit is assigned an age ranging from the Pliocene to the Pleistocene based on its stratigraphic position and lithological characteristics. However, the micropaleontological analysis of Sample 24M-18W indicates an early Miocene (late Burdigalian), which is

significantly older than the unit's defined age. This inconsistency may be due to:

- Reworking of Older Sediments: Older Miocene sediments could have been eroded and redeposited within the Pliocene to Pleistocene sequences, introducing older microfossils into younger deposits.
- Misidentification of the Unit: The sample may have been collected from a different stratigraphic unit not accurately represented in the map legend.
- Tectonic Activity: Faulting or folding could have juxtaposed older rocks against younger sediments, leading to the inclusion of older material within the unit.

4.12 Q^a Unit (Late Pleistocene to Holocene Mud Flat Deposits)

The Q^a Unit represents fine-grained sedimentary deposits formed during the late Pleistocene to Holocene, with an absolute age of ≤ 21.3 ka BP (e.g., Gharibreza, 2016). This unit is characterized by buff to creamy argillic silty clay deposits that include clasts ranging from 1 to 3 cm in size and are rich in calcite fragments. These sediments are interpreted as mud flat deposits (Figure 4-19a), indicative of low-energy depositional environments associated with fluctuating water levels and climatic conditions (Figure 4-19b). The measured thickness of this unit is ~ 50 m.

The unit is represented by 1,336 mapped polygons within the study area. The individual areas of these outcrops vary greatly, from as small as 0.0329 sq km to as large as 228.37 sq km. Notable large outcrops include OBJECTID_1: 3326 (228.37 sq km), 2691 (182.88 sq km), and 3567 (84.70 sq km). The cumulative area covered by the Q^a Unit is ~ 1061 sq km.

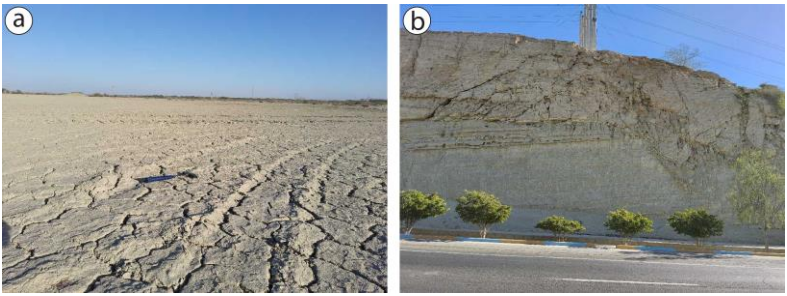

Figure 4-19. a) Mud flat in the Qª Unit at location P020, illustrating typical cracked, fine-grained sediment surfaces characteristic of low-energy depositional environments. b) Outcrop at location P023, displaying paleorelief with younger terrace deposits at the top. The image also highlights syn-sedimentary faults bounded to the erosional surface.

The Qª Unit exhibits distinctive lithological characteristics dominated by fine-grained sediments. The primary lithology consists of buff to creamy argillic silty clay, indicating a high content of clay minerals and fine silt-sized particles. The argillic nature suggests significant weathering and soil-forming processes. Embedded within the fine-grained matrix are clasts measuring between 1 and 3 cm. These clasts are composed of various lithologies but are notably rich in calcite fragments. Their presence indicates intermittent higher-energy events capable of transporting coarser material into the predominantly fine-grained environment.

The abundance of calcite fragments points to a source area rich in carbonate rocks or biogenic contributions from organisms that precipitate calcium carbonate. These fragments could also result from the reworking of older carbonate units exposed in the surrounding terrain. The sediments exhibit poor sorting due to the mixture of fine-grained matrix and coarser clasts. The overall texture is indicative of rapid deposition with minimal reworking, characteristic of mud flat environments where energy conditions can vary. The unit has a measured thickness of ~ 50 meters, reflecting substantial sediment accumulation during the late Pleistocene to Holocene.

4.12.1 Age and Correlation

The absolute age of the Q^a Unit is determined to be ≤ 21.3 ka BP (e.g., Gharibreza, 2016), placing it within the late Pleistocene to Holocene transition. This age determination is based on regional correlations and absolute dating methods, such as radiocarbon dating of organic material within the sediments.

The unit correlates with other late Pleistocene to Holocene fine-grained deposits in the region, commonly associated with mud flat environments formed during periods of climatic fluctuation and changing hydrological conditions. The timing corresponds with the last glacial maximum and subsequent deglaciation phases, which influenced sediment supply and depositional patterns.

4.13 Q^b Unit (Late Holocene Beach Deposits)

The Q^b Unit represents beach deposits formed during the Late Holocene, with an absolute age of ≤ 7.3 ka BP (e.g., Gharibreza, 2016; Normand, 2019). This unit is characterized by rose-gold arkosic sand and silt, featuring wave cross-bedding and caliche formation within the wave zone (Figure 4-20). The calculated thickness of the unit is ~ 50 m, indicating substantial sediment accumulation during this period. These sediments reflect dynamic coastal processes influenced by sea-level fluctuations and climatic conditions in the Holocene.

The unit is represented by 192 mapped polygons within the study area. The individual areas of these outcrops vary greatly, from as small as 0.0691 sq km to as large as 194.02 sq km. Notable large outcrops include OBJECTID_1: 40 (194.02 sq km), 127 (62.56 sq km), and 97 (49.60 sq km). The cumulative area covered by the Q^b Unit is ~ 404 sq km.

The lithological composition of the Q^b Unit is distinctive, dominated by rose-gold colored arkosic sands and silts. The arkosic nature indicates a high feldspar content, suggesting rapid erosion and minimal chemical weathering of granitic source rocks.

Figure 4-20. Beach deposits of the Q^b Unit at location P005.

The sediments exhibit several key features. The rose-gold hue is due to the presence of feldspar and iron oxide minerals. The arkosic sands and silts are rich in angular to sub-angular feldspar grains, along with quartz and mica, indicative of a proximal source area and rapid deposition. Wave cross-bedding is prominently observed within the unit. These structures are formed by the migration of ripples and dunes under the influence of oscillatory wave action in a shallow marine environment. The cross-bedding indicates variable current directions and high-energy conditions typical of beach settings.

Caliche layers are developed within the wave zone. Caliche, a hardened deposit of calcium carbonate, forms in arid to semi-arid climates where evaporation rates are high. Its presence suggests periods of subaerial exposure and pedogenic processes occurring within the coastal environment, possibly during low sea-level stands or tidal fluctuations. The sands are medium to coarse-grained, and the silts are fine-grained. The poor sorting and angularity of the grains reflect rapid deposition and limited transport distance from the source rocks. The unit attains a thickness of about 50 m.

4.13.1 Age and Correlation

The absolute age of the Q^b Unit is determined to be less than or equal to 7.3 ka BP (e.g., Gharibreza, 2016; Normand, 2019), placing it within the late Holocene. This age corresponds with a period of significant post-glacial sea-level rise following the last glacial maximum, leading to coastal transgression and the formation of new beach environments.

The unit correlates with other Holocene beach deposits in the region, which are characterized by similar lithologies and sedimentary structures. The arkosic composition and caliche formation are consistent with sediments deposited during periods of rapid sea-level change and climatic fluctuations in arid to semi-arid settings.

4.14 Q^{fp} Unit (Quaternary Alluvial Fan Deposits)

The Q^{fp} Unit represents Quaternary alluvial fan deposits characterized by an alternation of horizontal white to buff argil and fluvial sediments. With a measured thickness of ~ 50 m, this unit reflects dynamic depositional processes associated with fan environments during the Quaternary period.

The unit is represented by 681 mapped polygons within the study area. The individual areas of these outcrops vary greatly, from as small as 0.0041 sq km to as large as 64.20 sq km. Notable large outcrops include OBJECTID_1: 4426 (64.20 sq km), 8491 (25.97 sq km), and 8503 (19.45 sq km). The cumulative area covered by the Q^{fp} Unit is ~ 385 sq km.

The Q^{fp} Unit exhibits a complex lithology composed of both coarse clastic materials and fine-grained sediments. The unit is characterized by an alternation of horizontal layers of white to buff argil (clay-rich material) and fluvial deposits. Individual layers range from 4 to 6 m in thickness, contributing to the overall substantial thickness of the unit.

Clasts constitute 30–50% of the unit and are predominantly composed of sandstone, calcite, volcanic, and silicic pebbles, generally ranging from 2 to 10 cm in size. These clasts are moderately to weakly rounded and exhibit poor sorting, indicating rapid deposition from high-energy

processes typical of alluvial fan environments. The heterogeneity and size variation of the clasts suggest a diverse source area, including sedimentary, igneous, and metamorphic rocks.

The clasts are embedded within a silty matrix composed of white to buff argil, reflecting periods of lower energy deposition where finer sediments could settle. The alternation between clastic-rich layers and argil layers indicates fluctuating depositional conditions, possibly due to changes in climate, sediment supply, or tectonic activity influencing the energy levels within the depositional environment.

The tabulate (flat-lying) bedding observed in the unit suggests deposition on a relatively stable surface with minimal post-depositional deformation. The overall poor sorting and moderate to weak rounding of the clasts indicate limited transport distance from the source area and rapid deposition, which are characteristic features of proximal alluvial fan deposits.

4.14.1 Age and Correlation

The Q^{fp} Unit is assigned to the Quaternary period based on its stratigraphic position and lithological characteristics. Although specific absolute age determinations are not available for this unit, its features are consistent with Quaternary alluvial fan deposits found in similar geological settings.

The presence of volcanic and silicic pebbles among the clasts suggests a connection to Quaternary volcanic activity in the region. The poor sorting, heterogeneity, and rapid deposition are indicative of depositional processes active during the Quaternary, a period marked by significant climatic fluctuations and tectonic activity that influenced erosion and sedimentation patterns.

Correlation with other Quaternary alluvial fan deposits in adjacent areas supports the assignment of this unit to the Quaternary period. The lack of micropaleontological data limits the precision of age determination, but the geological context provides a reasonable basis for this correlation.

4.15 Q^{sd} Unit (Holocene Sand Dunes)

The Q^{sd} Unit represents aeolian sand dune deposits (Figure 4-21) formed during the Holocene. These deposits are characterized by golden to light brown wind-blown sands, reflecting dynamic desert environments influenced by climatic conditions prevalent in the Holocene. The unit has a calculated thickness of ~ 50 m, indicating substantial sediment accumulation due to persistent wind activity and sediment supply.

The unit is represented by 72 mapped polygons within the study area. The individual areas of these outcrops vary greatly, from as small as 0.0529 sq km to as large as 19.33 sq km. Notable large outcrops include OBJECTID_1: 10404 (19.33 sq km), 10005 (7.77 sq km), and 10037 (7.45 sq km). The cumulative area covered by the Q^{sd} Unit is ~ 65 sq km.

Figure 4-21. Holocene sand dunes (Q^{sd}) at location P013.

The lithology of the Q^{sd} Unit is dominated by unconsolidated, fine to medium-grained sands with a golden to light brown coloration. The sands are primarily composed of quartz grains, with minor contributions from feldspar and heavy minerals. This composition reflects the mineralogy of the source rocks and the effects of mechanical weathering and sorting by wind action.

4.15.1 Age and Correlation

The Q^{sd} Unit is assigned to the Holocene based on its stratigraphic position, depositional characteristics, and correlation with regional aeolian deposits. Sand dune formation is typically associated with arid to semi-arid climatic conditions that prevailed during certain periods of the Holocene.

Although specific absolute age determinations are not available for this unit, its features are consistent with Holocene aeolian deposits found in similar environmental settings. The unit overlies older Quaternary deposits, supporting its assignment to the Holocene. Correlation with nearby well-dated dune fields further substantiates this temporal placement.

4.16 Q^{al} Unit (Holocene Alluvial Deposits)

The Q^{al} Unit represents recent alluvial deposits formed during the Holocene. These unconsolidated sediments have accumulated in river channels, floodplains, and meander belts, reflecting active fluvial processes that continue to shape the landscape. The unit is characterized by alluvial materials interspersed with fragmented outcrops of older geological units found on terrace risers and occasionally within channels and meanders. The calculated thickness of the unit is ~ 50 m.

The unit is represented by 1031 mapped polygons within the study area. The individual areas of these outcrops vary greatly, from as small as 0.07 sq km to as large as 139.63 sq km. Notable large outcrops include OBJECTID_1: 7766 (139.63 sq km), 7695 (42.84 sq km), and 7730 (28.51 sq km). The cumulative area covered by the Q^{al} Unit is ~ 692.39 sq km.

The lithological composition of the Q^{al} Unit is diverse, comprising a mixture of clastic sediments derived from the erosion of upstream rock formations and transported by river systems. The alluvial deposits consist of a heterogeneous mix of clay, silt, sand, gravel, and occasional cobbles. This range of grain sizes reflects the variable energy conditions within the fluvial environment and the diverse geology of the drainage basin.

Embedded within the alluvial sediments are fragments of older geological units. These outcrops appear on the risers of terraces and sometimes within the middle of channels and meanders. They represent remnants of pre-existing formations that have been partially eroded and incorporated into the younger alluvial deposits. The sediments exhibit variable sorting and rounding. Coarser materials like gravel and cobbles are typically sub-angular to sub-rounded, indicating limited transport distance. Fine-grained sediments like silt and clay are well-sorted, having been transported in suspension during lower energy conditions. The sediments display a range of colors from light brown to gray, influenced by the mineral composition and the presence of organic material.

4.16.1 Age and Correlation

The Q^{al} Unit is assigned to the Holocene epoch based on its stratigraphic position, active depositional nature, and lack of consolidation. Alluvial deposits of this kind are characteristic of modern river systems and are continually being reworked and redeposited. The presence of unconsolidated sediments and ongoing fluvial processes supports the assignment of a recent age.

Correlation with other Holocene alluvial deposits in the region confirms the unit's age and depositional environment. The fragmented outcrops of older units within the alluvium indicate active erosion and reworking of pre-existing geological formations, a process consistent with Holocene fluvial dynamics.

5 Structural Analyses

This section provides an in-depth analysis of the structural features observed within the mapped area, focusing on the dominant faults and folds that shape the region's geology. The structural framework of the study area reflects the complex tectonic history associated with the Makran accretionary prism and its interactions with the surrounding plates. This chapter discusses the main structural features, including faults and folds, with particular emphasis on their orientation, geometry, and tectonic significance.

In addition to the analysis of faults and folds, structural balanced sections are employed to visualize and interpret the subsurface geometry of these features. These balanced sections, constructed using surface geological data, offer insights into the tectonic evolution of the region and provide a framework for understanding the complex interactions between faults, folds, and stratigraphic units. The balanced sections are a critical tool for reconstructing the deformation history and will be further explored in subsequent sections.

5.1 Folds

The SUTGMM AOI reveals a complex system of folds, including a mix of anticlines and synclines. These folds, developed under compressional tectonic regimes, show varying structural characteristics, such as plunging, overturned, and continuous fold axes. This analysis integrates both the fold map and table, providing a detailed discussion of their distribution, geometry, and tectonic implications.

5.1.1 Anticlines

In the AOI, several prominent anticlines have been identified (Figure 5-1), ranging from simple plunging structures to more complex overturned forms. The varying lengths and orientations of these anticlines reflect a dynamic deformation environment, where different stress regimes and tectonic processes shaped the region.

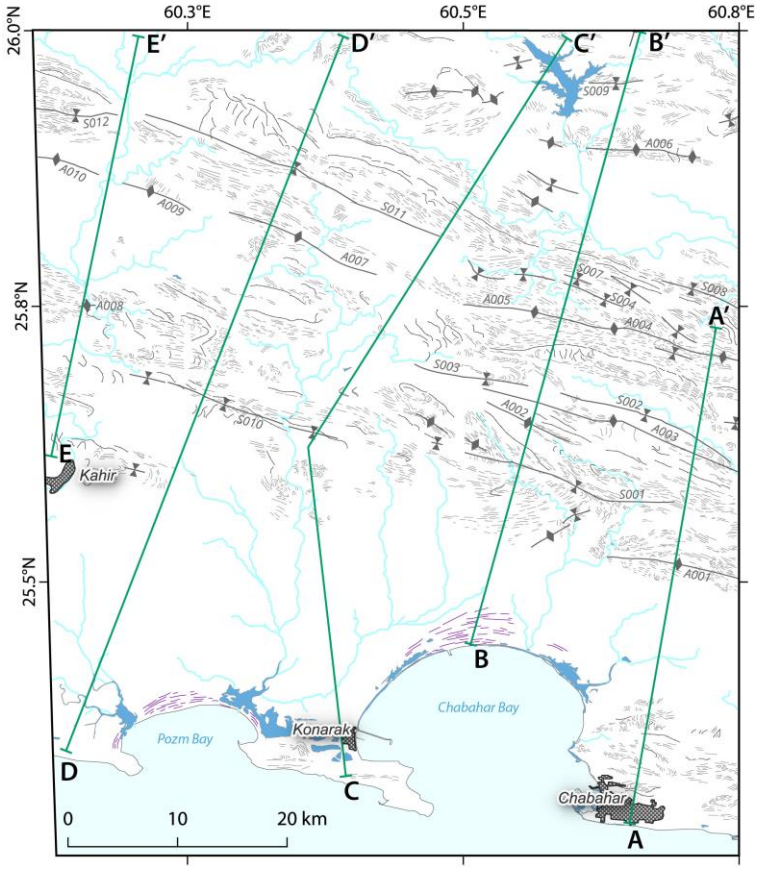

Figure 5-1. Fold map depicting anticlines and synclines within the SUTGMM AOI. The green lines (AA' to EE') represent transect lines used for cross-section construction.

5.1.2 Synclines

Similar to the anticlines, several prominent anticlines have been identified in the AOI, ranging from simple plunging structures to more complex overturned forms. The varying lengths and orientations of these synclines reflect a dynamic deformation environment, where different stress regimes and tectonic processes shaped the region.

5.2 Faults

The faults identified and mapped within the SUTGMM AOI (Figure 5-2) illustrate a complex tectonic regime dominated by active deformation. The study area is located in a tectonically active region, which features a complex network of faults including strike-slip, normal, and reverse faults. These faults were mapped and classified as follows: Strike-slip right-lateral, strike-slip left-lateral, reverse faults, and normal faults (Figure 5-2 and Table 5-1). The distribution of faults is spatially varied, with several zones exhibiting higher concentrations of tectonic activity.

5.2.1 Fault Mechanism Classification and Trends

The faults in the AOI are predominantly of strike-slip type, with left-lateral strike-slip being the most prevalent. Normal and reverse faults are also observed but are less frequent. Fault mechanisms are summarized as follows:

- Strike-slip faults (left-lateral and right-lateral) dominate the region, with trends primarily oriented NE-SW and NW-SE. These faults are typically associated with horizontal movement along fault planes.
- Reverse faults exhibit a more N-S or NE-SW orientation and are generally associated with compressional tectonics. These faults are less frequent but are significant in localized areas of the AOI.
- Normal faults are concentrated near the coastal areas, showing a N-S trend. These faults indicate extensional tectonics, which is

likely related to the regional crustal thinning or gravitational collapse.

The faults exhibit varying lengths and sinuosity, reflecting the tectonic complexity of the region. Strike-slip faults tend to have longer extents, while reverse and normal faults are generally shorter but more localized.

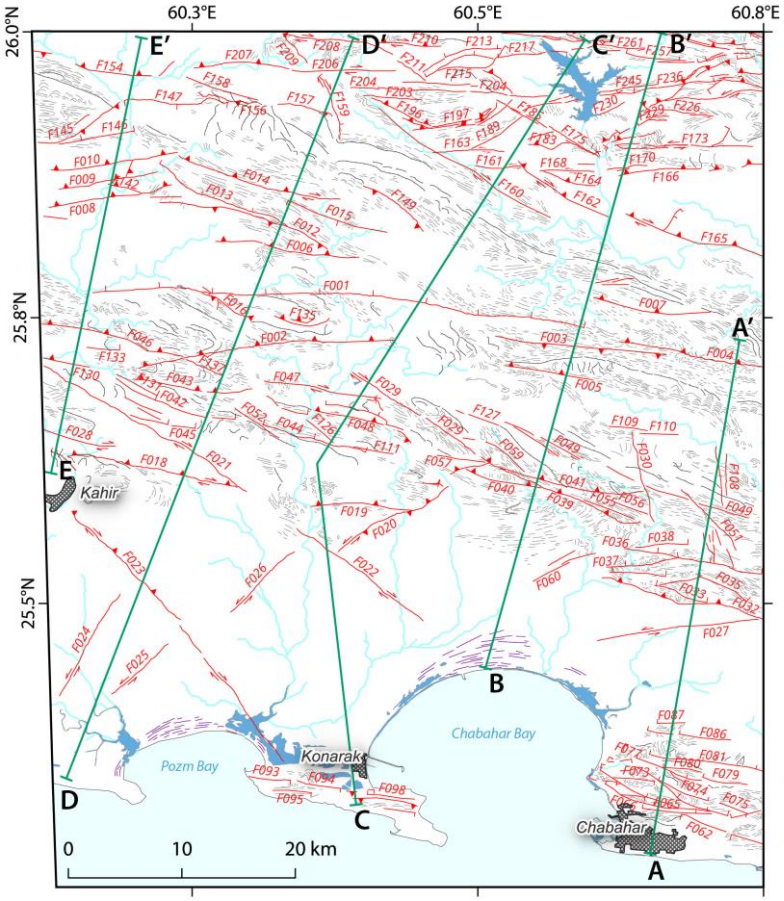

Figure 5-2. Fault map of the SUTGMM AOI. The green lines (AA' to EE') represent transect lines used for cross-section construction.

5.2.2 Geographic Distribution and Concentration of Faults

The spatial distribution of faults is not uniform across the AOI. Several zones can be defined based on the concentration and orientation of faults, with key faulting trends and mechanisms in each zone:

5.2.2.1 Central Zone

The Central Zone, is characterized by a diverse distribution of normal (Figure 5-3), strike-slip and reverse faults. The most prominent fault in this zone is F001, with a length of ~44 km, representing the longest fault in the AOI. Additional significant faults include F002 (~ 23 km), F021 (~ 22 km), F004 (~ 17 km), and F018 (~ 16 km). The faults in this zone generally trend NW-SE.

Figure 5-3. Normal faulting in the $Pl^{l.si.s}$ Unit at location P061 along Fault F122.

5.2.2.2 Northwestern Zone

The Northwestern Zone features a high concentration of strike-slip faults, particularly left-lateral faults. The dominant fault in this zone is F165 (~ 27 km), followed by F160 (~ 19 km) and F162 (~ 10 km). The main faults in the southwestern parts of this zone predominantly trend NE-SW, consistent with a left-lateral strike-slip mechanism. The northwestern

parts are mainly consistent with partially E-W trend of faults accommodating left-lateral component. This zone is tectonically active, with a dense network of strike-slip faults indicating significant horizontal displacement in response to regional shear forces.

5.2.2.3 Northeastern Zone

The Northeastern Zone is characterized by a more complex interplay of faults, with significant contributions from both strike-slip and reverse faulting. The longest faults in this zone include F013, F008, F009, F010, and F014, each of which follows a general NE-SW or N-S trend with an average length of ~ 10-15 km. This region appears to be influenced by both compressional forces (responsible for reverse faulting) and horizontal shear (strike-slip). The reverse faults in this zone suggest localized compression, which may be related to tectonic collision zones in the broader regional context.

5.2.2.4 Southwestern Zone

The Southwestern Zone has fewer main faults, but it is still an area of tectonic significance. The largest faults in this region include F023 (~ 30 km), which has two different segments. The NW segment has a reverse mechanism with a right-lateral component, while the SE segment is mainly moving right-laterally. Unlike F0223, the other faults in this zone have a NE-SW trend. F024 (~ 11 km), F025 (~ 7 km), and F026 (~ 8 km) are strike-slip left-lateral faults in this zone. The faults in this zone are primarily strike-slip, with both left-lateral and right-lateral motion observed. This region is influenced by the convergence between tectonic plates, which generates the shear necessary for strike-slip faulting.

5.2.2.5 Southeastern Zone

The Southeastern Zone, which includes areas around Konarak and Chabahar Bay, is characterized by normal and faults with strike-slip component. The faults in this zone generally trend WNW-ESE to E-W, with normal faults dominating the coastal areas. This suggests both

extensional and strike-slip tectonic forces, possibly linked to the regional tectonic setting and active margin processes near the coast.

Table 5-1. Geometrical parameters of some of the faults measured in the field surveys.

Fault Name	Latitude (° N)	Longitude (° E)	Strike (°)	Dip (°)	Rake Strike (°)	Rake Direction (°)	Mechanism
F107	25.765	60.272	260	85	-	-	RRL
F139	25.774	60.263	32	65	-	-	RLN
F016	25.753	60.289	205	74	40	15	RRL
F070	25.342	60.625	5	50	3	114	LL
F172	25.836	60.670	292	60	20	208	NLL
F180	25.894	60.606	250	60	-	-	N
F181	25.895	60.604	178	90	30	30	NLL
F177	25.899	60.600	115	85	10	285	LL
F178	25.898	60.611	320	55	20	228	LL
F179	25.898	60.613	298	70	-	-	N
F222	25.909	60.620	340	35	-	-	LLN
F224	25.911	60.624	310	65	75	320	N
F231	25.928	60.647	152	75	25	258	LLN
F232	25.932	60.649	30	50	37	232	RRL
F265	25.990	60.610	140	60	30	218	NLL
F264	25.989	60.603	140	70	60	85	N
F266	25.999	60.584	160	75	20	70	LLN
F263	25.998	60.579	45	50	45	315	N
F235	25.946	60.626	10	40	45	20	N
F246	25.949	60.621	255	65	-	-	N
F047	25.681	60.407	5	60	27	257	LL
F123	25.678	60.409	340	50	40	42	NRL
F124	25.674	60.414	70	55	45	28	NRL
F122	25.663	60.415	210	50	-	-	NLL
F048	25.655	60.427	20	40	-	-	NLL
F020	25.605	60.466	130	85	-	-	LLR
F142	25.863	60.195	30	40	-	-	R
F143	25.887	60.198	290	73	-	-	RLL
F146	25.914	60.199	185	55	-	-	N
F091	25.375	60.628	120	60	-	-	NLL
F089	25.364	60.614	120	50	-	-	NLL
F088	25.357	60.608	100	75	10	10	LLN
F134	25.629	60.136	40	65	-	-	NRL

5.2.3 Fault Concentration Zones

Several zones exhibit high concentrations of faults, with particularly intense faulting activity in the Northwestern, Northeastern, and Central zones:

- The Northwestern Zone is densely faulted with a predominance of strike-slip faults, indicating significant lateral tectonic movement.
- The Central Zone has a mix of fault types but shows a clear concentration of normal faults along the coastline, suggesting regional extensional forces.
- The Northeastern Zone is a tectonic transition zone where reverse and strike-slip faults intersect, indicating both compressional and shear forces acting on the region.

The distribution and orientation of faults in the AOI reflect the complex tectonic processes governing the region. The predominance of strike-slip faulting, suggests that the region is experiencing significant horizontal shearing forces, likely related to the larger-scale tectonic interactions between the adjacent plates. The presence of normal faults near the coast suggests local extensional processes, which may be linked to crustal thinning or the gravitational collapse of uplifted regions.

5.3 Structural Balanced Sections

The construction of structural balanced sections in this study was carried out using *Move 2D* software, an advanced structural geology modeling tool, to integrate surface geological data from mapped units, faults, folds, and bedding orientations derived from field surveys and a prepared geological map. This comprehensive approach allowed for the generation of accurate, balanced sections that reflect the complex geological structures of the area. The process included data preparation, setting up the cross-section lines, building the geological model, performing geometric balancing, and final visualization. Additionally, detailed lithological and mechanical properties were incorporated to refine the model, ensuring that the sections accurately represented both surface

and subsurface geology. By employing balanced sections, we ensure that the interpretations are geometrically valid and consistent with physical balancing principles, which is essential for understanding the true nature of the structural framework.

The balanced sections can also serve as a predictive tool for subsurface conditions, providing valuable information for regional tectonic studies, and seismic hazard assessment. By restoring the geological units to their pre-deformation state, we gain insights into the original depositional environments and the subsequent tectonic processes that shaped the region. This restoration not only helps in estimating the amount of crustal shortening but also aids in identifying potential zones of structural weakness, which are crucial for assessing seismic risk in this tectonically active region.

The structural balanced sections on the GeoNexus map cover five key transects (AA', BB', CC', DD', and EE') across the SUTGMM AOI, from the southern coastal areas to the northern limit of the AOI. Each transect captures important structural features such as faults and folds that characterize the Makran accretionary prism. This variability helps us understand the distribution of tectonic stress and the mechanical properties of the sedimentary units.

5.3.1 Data Preparation and Input

5.3.1.1 GeoNexus Map and Mapped Units

The GeoNexus map (SUTGMM) was constructed from extensive field mapping, where lithological boundaries, stratigraphic units, and structural features were identified. Each unit's spatial extent, lithological composition, and surface fault traces were digitized into GIS software and imported into *Move 2D* for structural balanced section construction. The map provided a base layer that helped ensure the geological features in the balanced sections were consistent with field observations.

For each lithological unit (Table 5-2), the geological contacts and unit thicknesses were carefully traced based on the field survey, with

additional validation using satellite imagery where available. This base information ensured that each stratigraphic layer in the sections were accurately placed in terms of its spatial extent and thickness.

5.3.1.2 Faults and Fold Geometries

Detailed structural data, including surface fault traces and fold axes, were mapped in the field and digitized for integration into *Move 2D*. This data formed the framework for interpreting subsurface fault geometries and fold structures. Each fault was mapped along its surface expression, and its geometry (e.g., strike, dip and rake) was constrained using field measurements of fault planes, such as fault slickensides or fault breccias, where available. These surface expressions were then projected to depth using fault-bend fold models and *Move 2D*'s structural simulation capabilities. For folds, axial traces and hinge lines were digitized and extrapolated using geometric models to replicate their subsurface geometry.

5.3.1.3 Bedding Data:

Bedding orientation data (strike and dip) were collected from multiple field stations (Figure 5-4) to guide the placement and orientation of stratigraphic units within the balanced sections. These measurements were essential for determining the true dip of the layers and for simulating folding in areas where deformation had significantly affected the original bedding geometry. Strike and dip data from multiple locations were averaged or interpolated, depending on the complexity of the region, to ensure that bedding planes in the model followed realistic geological patterns.

5.3.2 Data Integration and Input

To enhance the model's realism, a detailed dataset containing mechanical and lithological properties of the rock units was imported into *Move 2D* (Table 5-3). This dataset provided critical information on lithology, compaction, porosity, and mechanical behavior, which were used to refine the subsurface model and ensure that the modeled units behaved

realistically under tectonic stresses. The following key parameters from the dataset were integrated into the model:

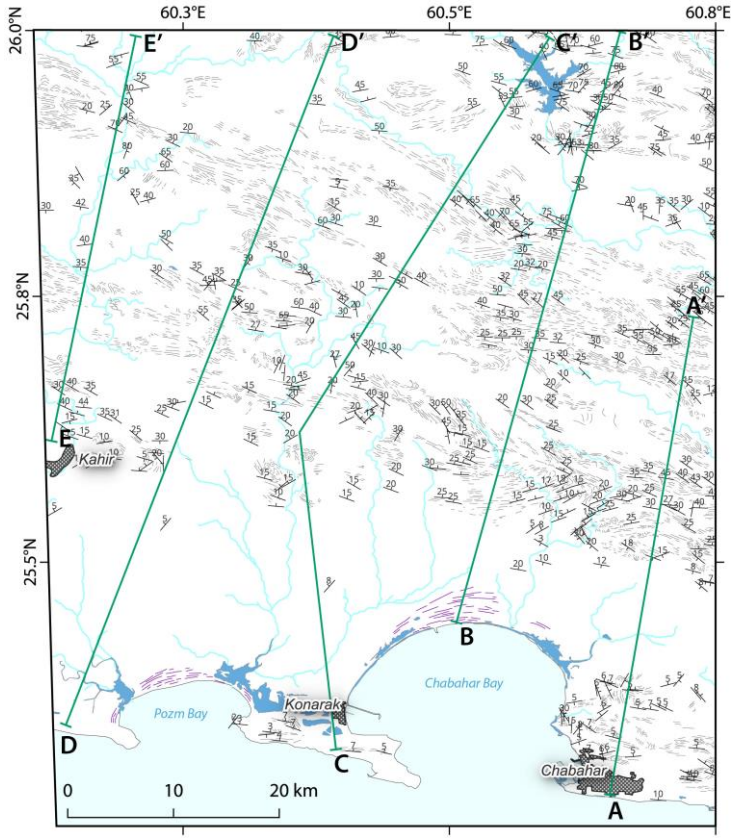

Figure 5-4. Map showing bedding orientations derived from field surveys within the SUTGMM AOI. Bedding dip angles (in degrees) are marked, and the strike symbols indicate the direction of bedding planes. The green lines (AA' to EE') represent transect lines used for balanced sections construction.

5.3.2.1 Rock Type and Lithological Composition

Each stratigraphic layer was assigned a specific lithological composition, defined in Table 5-3 by percentages of sandstone, shale, and limestone. These percentages were used to represent the relative abundance of

each rock type within the model. For example, units with a higher sandstone content were assumed to be more rigid, while those with higher shale content were modeled as more ductile. This lithological variability was critical for simulating fault and fold behavior accurately. The proportions of lithologies influenced the mechanical behavior of each unit under compression and extension, which was essential for constructing realistic deformation features in the sections.

5.3.2.2 Compaction and Porosity

Table 5-3 provides values for Porosity and Depth Coefficient. These parameters were crucial for modeling sedimentary layers, as compaction significantly affects their thickness and mechanical properties with increasing burial depth. In *Move 2D*, these values were used to apply a compaction model that simulated how porosity decreases with depth, causing layers to thin. The porosity data were particularly important for reconstructing sedimentary basins, where variations in compaction control the thickness of stratigraphic units and influence the overall geometry of the cross-section.

5.3.2.3 Mechanical Properties

The Grain Size, Density, Young's Modulus, and Poisson's Ratio columns were input into *Move 2D* to define the mechanical behavior of each lithological unit. Young's Modulus, which measures the stiffness of a material, was especially critical for modeling the elastic response of rocks during deformation. Higher values of Young's Modulus indicated more resistant units, which influenced the way faults propagated through the subsurface. Similarly, Poisson's Ratio, which describes the degree of lateral expansion when a material is compressed, provided insights into how different units would respond to tectonic stresses. These mechanical properties ensured that the simulated geological structures (e.g., faults and folds) reflected the true physical behavior of the units under stress. Units with higher Poisson's Ratios, for instance, were more prone to ductile deformation, influencing fold geometry and fault behavior.

5.3.2.4 Time/Depth Conversion

Table 5-3 included parameters for Time/Depth Conversion, particularly the velocity parameter (V_0), used to convert seismic time data into depth measurements. This conversion was necessary for translating seismic horizons from time-domain interpretations into depth-domain geological cross-sections, providing accurate subsurface depth estimates. The time-depth conversion allowed for the integration of seismic data into the model, aligning the interpreted seismic stratigraphy with the geological cross-section.

5.3.3 Setting Up Section Lines

Cross-section lines were carefully placed across the AOI, perpendicular to major geological structures (e.g., faults, folds) to ensure an accurate representation of the subsurface. The cross-section lines were selected based on key outcrop locations and structural features identified during fieldwork. The perpendicular orientation to the regional structural trend was critical for capturing the true geometry of faults and folds, ensuring that any interpreted deformation was consistent with observed surface structures. The cross-section lines also took into account changes in lithology and thickness, ensuring that representative sections of the study area were captured.

5.3.4 Building the Cross-Section

5.3.4.1 Surface Line Tracing

The surface topography was defined using SRTM 30m (Farr et al., 2007) Digital Elevation Model (DEM), which was imported into Move 2D. Alternatively, field observations were used to manually trace the topographic profiles along the cross-section lines. The surface profiles provided the upper boundary for the sections and ensured that geological units matched the topographic constraints of the region.

5.3.4.2 Fault and Horizon Construction

Fault traces and horizon markers (based on lithological unit boundaries) were projected into the sections. Fault planes were extended to depth using structural modeling tools within *Move 2D*, guided by field measurements of fault dip and strike. The integration of mechanical properties from Table 5-3 (e.g., Young's Modulus, density) helped refine the fault geometries, ensuring that more competent units (e.g., sandstone-rich layers) exhibited steeper fault angles, while less competent units (e.g., shale-rich layers) had lower-angle faults. Horizon markers were also constructed based on the mapped stratigraphy, with adjustments made for compaction and porosity changes due to burial depth.

5.3.4.3 Folding Models

Folded strata were modeled using parallel and similar fold geometries, which were extrapolated from field observations. The use of the lithological and mechanical properties (e.g., Poisson's Ratio, grain size; Table 5-3) helped constrain fold geometry by controlling the behavior of different units during folding. For example, thicker or more rigid layers (higher Young's Modulus) resisted deformation and formed broader folds, while more ductile layers (lower Poisson's Ratio) produced tighter folds.

5.3.5 Geometric and Kinematic Balancing

Once the cross-section was constructed, geometric balancing was performed to ensure that the modeled structures (e.g., folds and faults) were geometrically and kinematically consistent. This involved retro-deforming the cross-section to a pre-deformation state using fault-bend fold models. The balancing process verified that the geological structures could have realistically formed from an initial, undeformed configuration. The mechanical properties input from Table 5-3, particularly Young's Modulus and Poisson's Ratio, were critical during this step, as they dictated how each unit responded to tectonic forces. Additionally,

kinematic restoration was applied to validate the modeled deformation, ensuring that the observed geological structures could evolve from realistic deformation processes.

Table 5-2. Geounits inputparameters for *Move 2D* for structural balanced sections of the SUTGMM project.

Horizon	**Colour**	**Rock Type**	**Age** (Ma)	**Thickness** (m)
Text	Color	Text	Real	Real
#0000FF	#0000CD	#00009B	#000069	#FFFF00
n/a	n/a	n/a	n/a	Metres
dimensionless	dimensionless	dimensionless	dimensionless	dimension
$MPl^{m.s}$	#e9ffbe	Default	5.5	150
$MPl^{m.s.c}$	#e3ff80	Default	5	250
Ml^{w}	#3f36ba	Default	11	10
$M^{s.sh}$	#ffff00	Default	12	200
$M^{s.si}$	#fffbe	Default	10	200
$M^{sh.s}$	#ffff73	Default	11	200
$OlM^{s.sh.c}$	#ffa77f	Default	13	250
$OlM^{sh.s}$	#ffaa00	Default	15	350
$PlPe^{c.s.si}$	#00ffe4	Default	3	150
$Pl^{l.si.s}$	#e6e600	Default	4	100
Pl^{si}	#f5ca7a	Default	4	100
$Pl^{si.c}$	#ffbebe	Default	4	100
Q^{a}	#eef1a0	Default	1	50
Q^{al}	#ffffff	Default	1	50
Q^{b}	#ffd37f	Default	1	50
Q^{fp}	#ffd9cc	Default	1	50
Q^{sd}	#ffffff	Default	1	50
Water	#66ccff	Default	0	10
vegetation	#ff00ff	Default	0	10

Table 5-3. Mechanical and lithological input parameters used in *Move 2D* for structural balanced sections of the SUTGMM project.

Name	**Name**	**Elements**	**Elements**	**Elements**	**Compaction**	**Compaction**	**Compaction**	**Time/Depth Conversion**	**Time/Depth Conversion**	**Other**	**Other**	**Other**	**Other**
Text	Integer	Real	Real	Real	Real	Real	Text	Real	Real	Real	Real	Real	Real
Rock Type	RockPropertyID	Sandstone (%)	Shale (%)	Limestone (%)	Porosity	Depth Coefficient	Compaction Curve	v_0	k	Grain Size	Density	Young Modulus	Poisson Ratio
#00CD00	#009B00	#9B0000	#690000	#00FF00	#FFFF00	#FFCD00	#FF9B00	#FF00FF	#FF00CD	#FF0069	#FFFFFF	#CDFFFF	#9BFFFF
n/a	n/a	Percent	Percent	Percent	Fraction	1/Kilometre	n/a	Metre/Second	n/a	Millimetre	Gram/Cubic Centimetre	Megapascal	n/a
dimensionless	dimensionless	percent	percent	percent	fraction	depth coefficient	dimensionless	velocity	dimensionless	physical size	density	pressure	dimensionless
Sandstone	0	100	0	0	0.49	0.27	Default	3500	0.5	0.375	2500	15000	0.295
Shale	1	0	100	0	0.63	0.52	Default	2500	0.5	0.047	2720	32500	0.3
Limestone	2	0	0	100	0.41	0.4	Default	2600	0.5	0.005	2710	45000	0.215
Default	3				0.56	0.39	Default	2200	0.5	0.211	2680	23750	0.3
ShalySand	4				0.56	0.39	Default	2200	0.5	0.211	2680	23750	0.3
Salt	5				0	0	None	4481	0.5	0	2200	5810	0.4
Chalk	6				0.7	0.71	Default	4481	0.5	0	2200	5810	0.4

5.3.6 Refining and Validating the Balanced Sections

The balanced sections were iteratively refined by comparing them to both field data and geological interpretations. Adjustments were made to fault angles, fold geometries, and layer thicknesses as necessary. The porosity and compaction data were particularly useful for refining the thickness of sedimentary layers, as burial and compaction can significantly reduce layer thickness over time. The final balanced sections were validated by ensuring that the modeled structures were consistent with surface observations and the regional tectonic framework.

5.3.7 Final Visualization and Output

Once finalized, the balanced sections were exported from *Move 2D* in various formats, including high-resolution images and vector files for further analysis and inclusion in the final GeoNexus maps and the report. The final balanced sections incorporated not only the surface geology but also the detailed mechanical and lithological properties from the data table, ensuring a comprehensive representation of the subsurface geology. These balanced sections provided key insights into the structural complexities of the region, including the relationships between fault geometries, fold structures, and lithological boundaries.

5.4 Mud Volcanoes

Mud volcanoes are formed through the expulsion of mud, water, and gases from depth, often facilitated by tectonic pressures and fluid overpressure within subsurface layers. The mud volcano activity can cause deformation of surrounding and overlying strata, resulting in uplifted zones, fractures, and occasionally large-scale displacement of surface layers. These features can be indicators of subsurface hydrocarbon migration and fluid overpressure zones, as well as evidence of deeper tectonic stresses (Dimitrov, 2002; Kopf, 2002).

Mud volcanoes represent a significant structural feature within the study area, where both active and inactive mud volcanoes were identified and

documented, each showing unique structural characteristics that contribute to the broader understanding of deformation patterns and fluid migration pathways.

5.4.1 Inactive Mud Volcano

At location P009, an old, inactive mud volcano was mapped and observed (Figure 5-5). This feature, while no longer actively extruding material, displays significant structural displacement. The old, passive vent of the mud volcano is clearly visible, disrupting the upper horizons and causing noticeable offsets in the stratigraphic layers. This displacement suggests a history of overpressured fluid expulsion, which has since subsided, leaving a preserved structure that now serves as a record of past activity.

The stratigraphic displacement in this inactive mud volcano allows for an assessment of historical tectonic and fluid movement processes within the area. The observed offset within the upper horizons provides clues to the pressures and geological forces that contributed to the mud volcano's formation and eventual inactivity. The structural analysis of this feature aids in understanding the migration pathways of fluids and potential hydrocarbon indicators (e.g., Kopf, 2002) within the study area.

Figure 5-5. Inactive mud volcano at location P009. The passive vent of the volcano has deformed and displaced the upper stratigraphic horizons.

5.4.2 Active Mud Volcano

An active mud volcano was documented at location P1084 (Figure 5-6). Unlike the inactive volcano (Figure 5-5), this feature shows ongoing activity with fresh mud and gas emissions. Active mud volcanoes are indicative of current subsurface overpressure conditions, where fluids and gases are still being forced upwards. Such activity can reflect ongoing tectonic stress and may highlight zones of weakness within the underlying stratigraphy.

The contrast between the active and inactive mud volcanoes mapped in the SUTGMM project highlights the temporal evolution of these features. By analyzing these mud volcanoes, we gain a better understanding of the tectonic and fluid dynamics at play in this region, as well as the implications for hydrocarbon migration and pressure regimes within subsurface layers.

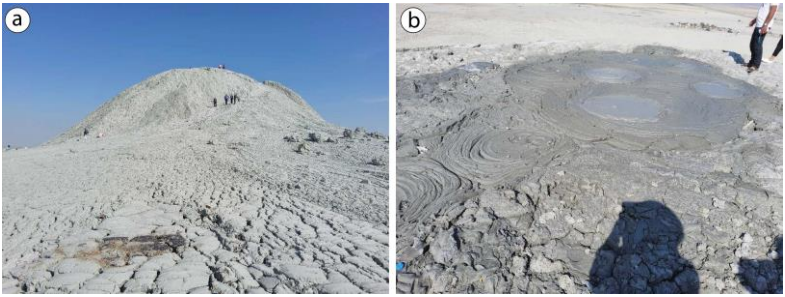

Figure 5-6. Active mud volcano at location P1084. a) The elevated structure with fresh mud channels indicates ongoing fluid and gas emissions, suggesting active subsurface overpressure. b) Close-up of bubbling mud pools on the surface of the active mud volcano, demonstrating current activity and fluid migration from depth.

6 Summary and Conclusions

6.1 Summary

6.1.1 Integration of Technologies

This project marks a significant leap forward in the field of geological mapping, offering a new standard for accuracy and efficiency through the seamless integration of modern technologies. The combination of cloud computing, machine learning, remote sensing, and object-based image analysis (OBIA) enabled the SUTGMM project to produce high-resolution, reliable geological maps for the Makran region. This technology-driven approach not only enhances the level of detail in the mapping process but also sets the foundation for new methodologies that can be applied to other geologically complex areas globally. The integration of diverse data sources, including Sentinel-1, Sentinel-2, ASTER, Landsat-8, and SRTM DEM, provided a multifaceted view of the region's geological features, allowing for more nuanced and accurate classification.

6.1.2 Methodological Innovation

A major methodological advancement in this project is the shift from traditional pixel-based analysis to the more sophisticated object-based image analysis (OBIA). This transition allowed for better segmentation of the landscape based on the contextual and spatial properties of geological formations, aligning the classification process more closely with the way geologists interpret terrestrial features. The use of multiple datasets spanning various resolutions and spectral ranges provided an in-depth look at the region's geology, leading to a more precise and comprehensive understanding of geological structures and stratigraphy.

This innovative workflow significantly reduces both the time and the number of personnel required for large-scale mapping projects.

6.1.3 Computational Efficiency

The project's reliance on *Google Earth Engine* enabled the management and processing of vast volumes of data, overcoming traditional limitations in computational power and accessibility. Cloud computing allowed for the concurrent processing of multi-source remote sensing data, which significantly improved the scalability of the project. This enhanced computational efficiency, combined with the use of machine learning algorithms, such as Random Forest (RF), allowed the project to handle complex datasets and execute sophisticated workflows at various spatial scales with ease. This breakthrough demonstrates how cloud-based platforms can streamline and expedite geological mapping projects that traditionally required extensive manual labor and on-site computation.

6.1.4 Accuracy and Reliability

The application of the Random Forest algorithm yielded an accuracy rate of 85%, with a Kappa coefficient of 0.84, demonstrating the robustness of machine learning models in geological classification. These high accuracy levels validate the effectiveness of machine learning approaches in geosciences, especially when combined with field verification techniques. The achieved accuracy further underscores the potential of integrating artificial intelligence (AI) in future geological research, offering a reliable and scalable method for complex geological areas such as the Makran region. This approach can serve as a template for future studies that seek to enhance both the accuracy and efficiency of geological classification processes.

6.1.5 Scalability and Broader Applications

This project acted as a pilot for a new generation of geological mapping methods, providing a blueprint for applying server-based geological mapping to other geologically complex regions across Iran and beyond.

The scalability of the SUTGMM workflow demonstrates its potential to revolutionize geological mapping, particularly in regions where traditional methods struggle to capture the intricacies of the terrain. The success in the Makran region showcases the method's adaptability and scalability, offering promising prospects for broader implementation in regional and global geological surveys.

6.1.6 Interdisciplinary Collaboration

The success of this project highlights the importance of interdisciplinary collaboration. Experts from various fields—including geology, remote sensing, computer science, and data engineering—worked together to develop a comprehensive and innovative geological mapping solution. The combination of geological expertise with modern computational techniques demonstrates the transformative power of interdisciplinary efforts. Moving forward, continued collaboration between these disciplines will be critical in refining and expanding the applicability of these methods in geological research and environmental monitoring.

6.1.7 Geological Significance

The detailed geological analysis produced through the SUTGMM project offers a comprehensive understanding of the sedimentary dynamics, stratigraphic sequences, and tectonic features of the Makran region. By documenting and analyzing geological units in great detail, this report contributes to the broader scientific knowledge base of the region. It enhances our understanding of how regional geodynamics have shaped the landscape over millions of years. Furthermore, the integration of additional petrological and fossil data will provide a more nuanced interpretation of these processes, supporting future research efforts and resource management decisions.

6.1.8 Optimized GeoNexus Workflow and Protocol

The GeoNexus workflow and protocol (Figure 3-15) developed through the SUTGMM project represent a monumental step forward in cost-

effective, large-scale geological mapping. The workflow and protocol demonstrate the transformative potential of combining advanced, modern geospatial technologies, machine learning, and cloud-based computing to streamline the geological mapping process.

One of the most striking achievements of the GeoNexus Protocol is its ability to deliver high-quality geological maps at a fraction of the cost traditionally required for such projects, which results in a cost reduction of nearly 80% and highlights the potential of this approach to transform geological mapping in regions where financial resources are limited.

Furthermore, the time and personnel required for large-scale mapping have been significantly optimized. Traditionally, mapping an area of 30k sq km (scale 1:50,000) would require 15 teams working for 3 years, or alternatively, 1 team working for 15 years. With the GeoNexus workflow, the same task can be completed by 1 team in just 1 year. This dramatic reduction in both time and manpower demonstrates the immense scalability and efficiency of the GeoNexus protocol, making it a viable solution for geological mapping projects of any scale.

6.2 Recommendations

1. Algorithm Development: The methodology developed in this project should be tested in other geologically complex regions to assess its adaptability and robustness. Implementing this standardized workflow in various terrains could lead to a unified approach for geological mapping across diverse geological contexts.
2. Algorithm Refinement: Although the Random Forest algorithm achieved high accuracy, future research should explore other machine learning and deep learning algorithms (e.g., convolutional neural networks) to further enhance accuracy and reliability. Continual refinement of these algorithms is necessary to stay at the forefront of technological advancements in geological mapping.
3. Enhancing Data Resources: Integrating additional types of data—such as hyperspectral images, advanced radar processing, and

ground-based spectroscopy—will provide further opportunities for refining geological classifications. These data sources can help improve model performance and enable more detailed interpretations of subsurface structures.

4. User-Friendly Software Development: Developing user-friendly interfaces for this workflow can democratize access to advanced technologies for geologists without extensive programming experience. Such tools will accelerate the adoption of these methods by the broader geological community, especially for non-specialist users.

5. Field Validation: Expanding field implementations to further verify and refine the results will enhance the overall reliability of the generated maps. Ground-truthing remains an essential step for ensuring that the outputs match real-world geological features, thus improving confidence in the classification system.

6. Collaboration with Geological Institutions: Collaborating with national and international geological organizations will enable the scaling of this methodology to update existing geological maps and implement it on a larger scale. These collaborations will facilitate the exchange of knowledge and resources, fostering advancements in geological research.

7. Environmental Applications: This methodology has the potential for applications beyond geology, including environmental monitoring. The integration of remote sensing data with geospatial analysis can be employed for land-use change detection, vegetation cover analysis, and studying the impacts of climate change on geological formations.

8. 3D Geological Modeling: Future research should investigate the integration of the SUTGMM workflow with 3D geological modeling techniques to produce three-dimensional representations of subsurface geology. This could offer a more comprehensive

understanding of geological structures, aiding in exploration and resource management.

6.3 Outlook

In the current phase of the project, sheets Gor, Kahir, and Gurdim are only partially mapped, covering the eastern portions of their frames (Figure 4-2). The SUTGMM project aims to complete these sheets by mapping the missing western areas, thus providing a comprehensive geological framework across the entire study area and achieving a fully integrated set of detailed geological sheets for the region.

6.4 Conclusions

The SUTGMM project represents a significant advancement in geological mapping and analysis, opening new avenues for exploring and understanding complex geological regions. By harnessing the power of modern technologies—such as OBIA, machine learning, and cloud computing—this project not only delivered high-resolution geological maps but also set a precedent for how future geological studies can be conducted with greater accuracy and efficiency. The success of this approach in the GeoNexus/SUTGMM project demonstrates its potential for widespread application, paving the way for more effective geological analyses in regions that were previously difficult to map.

As the methodology continues to evolve through algorithm refinement and field validation, it holds the promise of becoming a cornerstone in the next generation of geological mapping, both in Iran and globally. With these technological advances, geoscientists are better equipped to meet the challenges of modern geological research, enhancing our ability to manage natural resources and mitigate geological hazards.

References

Alinaghi, A., Koulakov, I., Thybo, H., 2007. Seismic tomographic imaging of P - and S -waves velocity perturbations in the upper mantle beneath Iran. Geophysical Journal International 169, 1089–1102. https://doi.org/10.1111/j.1365-246X.2007.03317.x

Alpaydin, E., 2020. Introduction to machine learning, 4th ed, Adaptive computation and machine learning series. The MIT Press, Cambridge, Massachusetts.

Alvarez, W., Engelder, T., Geiser, P.A., 1978. Classification of solution cleavage in pelagic limestones. Geology 6, 263. https://doi.org/10.1130/0091-7613(1978)6<263:COSCIP>2.0.CO;2

Amani, M., Ghorbanian, A., Ahmadi, S.A., Kakooei, M., Moghimi, A., Mirmazloumi, S.M., Moghaddam, S.H.A., Mahdavi, S., Ghahremanloo, M., Parsian, S., Wu, Q., Brisco, B., 2020. Google Earth Engine Cloud Computing Platform for Remote Sensing Big Data Applications: A Comprehensive Review. IEEE Journal of Selected Topics in Applied Earth Observations and Remote Sensing 13, 5326–5350. https://doi.org/10.1109/JSTARS.2020.3021052

Arthurton, R.S., Farah, A., Ahmed, W., 1982. The Late Cretaceous-Cenozoic history of western Baluchistan Pakistan—the northern margin of the Makran subduction complex. Geological Society, London, Special Publications 10, 373–385. https://doi.org/10.1144/GSL.SP.1982.010.01.25

Baatz, M., Schäpe, A., 2000. Multiresolution segmentation: An optimization approach for high quality multi-scale image segmentation. Presented at the Angewandte Geographische Informationsverarbeitung XII, pp. 12–23.

Back, S., Morley, C.K., 2016. Growth faults above shale – Seismic-scale outcrop analogues from the Makran foreland, SW Pakistan. Marine and Petroleum Geology 70, 144–162. https://doi.org/10.1016/j.marpetgeo.2015.11.008

Bahdanau, D., Cho, K., Bengio, Y., 2016. Neural Machine Translation by Jointly Learning to Align and Translate. https://doi.org/10.48550/arXiv.1409.0473

Berberian, F., Muir, I.D., Pankhurst, R.J., Berberian, M., 1982. Late Cretaceous and early Miocene Andean-type plutonic activity in northern Makran and Central Iran. Journal of the Geological Society 139, 605–614. https://doi.org/10.1144/gsjgs.139.5.0605

Bijwaard, H., Spakman, W., Engdahl, E.R., 1998. Closing the gap between regional and global travel time tomography. Journal of Geophysical Research: Solid Earth 103, 30055–30078. https://doi.org/10.1029/98JB02467

Bird, P., Toksöz, M.N., Sleep, N.H., 1975. Thermal and mechanical models of continent-continent convergence zones. J. Geophys. Res. 80, 4405–4416. https://doi.org/10.1029/JB080i032p04405

Blaschke, T., 2010. Object based image analysis for remote sensing. ISPRS Journal of Photogrammetry and Remote Sensing 65, 2–16. https://doi.org/10.1016/j.isprsjprs.2009.06.004

Blaschke, T., Hay, G.J., Kelly, M., Lang, S., Hofmann, P., Addink, E., Queiroz Feitosa, R., Van Der Meer, F., Van Der Werff, H., Van Coillie, F., Tiede, D., 2014. Geographic Object-Based Image Analysis – Towards a new paradigm. ISPRS Journal of Photogrammetry and Remote Sensing 87, 180–191. https://doi.org/10.1016/j.isprsjprs.2013.09.014

Breiman, L., 2001. Random Forests. Machine Learning 45, 5–32. https://doi.org/10.1023/A:1010933404324

Breiman, L., 1996. Bagging predictors. Machine Learning 24, 123–140. https://doi.org/10.1007/BF00058655

Burg, J., Bernoulli, D., Smit, J., Dolati, A., Bahroudi, A., 2008. A giant catastrophic mud-and-debris flow in the Miocene Makran. Terra Nova 20, 188–193. https://doi.org/10.1111/j.1365-3121.2008.00804.x

Burg, J.-P., 2018. Geology of the onshore Makran accretionary wedge: Synthesis and tectonic interpretation. Earth-Science Reviews 185, 1210–1231. https://doi.org/10.1016/j.earscirev.2018.09.011

Byrne, D.E., Sykes, L.R., Davis, D.M., 1992. Great thrust earthquakes and aseismic slip along the plate boundary of the Makran Subduction Zone. Journal of Geophysical Research: Solid Earth 97, 449–478. https://doi.org/10.1029/91JB02165

Chandra, U., 1984. Focal mechanism solutions for earthquakes in Iran. Physics of the Earth and Planetary Interiors 34, 9–16. https://doi.org/10.1016/0031-9201(84)90080-3

DeMets, C., Gordon, R.G., Argus, D.F., 2010. Geologically current plate motions. Geophysical Journal International 181, 1–80. https://doi.org/10.1111/j.1365-246X.2009.04491.x

Dercourt, J., Zonenshain, L.P., Ricou, L.-E., Kazmin, V.G., Le Pichon, X., Knipper, A.L., Grandjacquet, C., Sbortshikov, I.M., Geyssant, J., Lepvrier, C., Pechersky, D.H., Boulin, J., Sibuet, J.-C., Savostin, L.A., Sorokhtin, O., Westphal, M., Bazhenov, M.L., Lauer, J.P., Biju-Duval, B., 1986. Geological evolution of the tethys belt from the atlantic to the pamirs since the LIAS. Tectonophysics 123, 241–315. https://doi.org/10.1016/0040-1951(86)90199-X

Dimitrov, L.I., 2002. Mud volcanoes—the most important pathway for degassing deeply buried sediments. Earth-Science Reviews 59, 49–76. https://doi.org/10.1016/S0012-8252(02)00069-7

Dolati, A., 2010. Stratigraphy, structural geology and low-temperature thermochronology across the Makran accretionary wedge in Iran. ETH Zürich, Switzerland.

Drăguț, L., Csillik, O., Eisank, C., Tiede, D., 2014. Automated parameterisation for multi-scale image segmentation on multiple layers. ISPRS Journal of Photogrammetry and Remote Sensing 88, 119–127. https://doi.org/10.1016/j.isprsjprs.2013.11.018

Ellouz-Zimmermann, N., Deville, E., Müller, C., Lallemant, S., Subhani, A.B., Tabreez, A.R., 2007. Impact of Sedimentation on Convergent Margin Tectonics: Example of the Makran Accretionary Prism (Pakistan), in: Lacombe, O., Roure, F., Lavé, J., Vergés, J. (Eds.), Thrust Belts and Foreland Basins, Frontiers in Earth Sciences. Springer Berlin Heidelberg, Berlin, Heidelberg, pp. 327–350. https://doi.org/10.1007/978-3-540-69426-7_17

Engdahl, E.R., Jackson, J.A., Myers, S.C., Bergman, E.A., Priestley, K., 2006. Relocation and assessment of seismicity in the Iran region. Geophysical Journal International 167, 761–778. https://doi.org/10.1111/j.1365-246X.2006.03127.x

Falcon, N.L., 1974. Southern Iran: Zagros Mountains. Geological Society, London, Special Publications 4, 199–211. https://doi.org/10.1144/GSL.SP.2005.004.01.11

Farhoudi, G., Karig, D.E., 1977. Makran of Iran and Pakistan as an active arc system. Geology 5, 664. https://doi.org/10.1130/0091-7613(1977)5<664:MOIAPA>2.0.CO;2

Farr, T.G., Rosen, P.A., Caro, E., Crippen, R., Duren, R., Hensley, S., Kobrick, M., Paller, M., Rodriguez, E., Roth, L., Seal, D., Shaffer, S., Shimada, J., Umland, J., Werner, M., Oskin, M., Burbank, D., Alsdorf, D., 2007. The Shuttle Radar Topography Mission. Rev. Geophys. 45, RG2004. https://doi.org/10.1029/2005RG000183

Fathian, A., 2022. Active tectonics of the Zagros front (PhD thesis). RWTH Aachen University, Aachen, Germany.

GEBCO Compilation Group, 2023. GEBCO 2023 Global Bathymetry and Topography. https://doi.org/10.5069/G9D21VTT

Gharibreza, M., 2016. Evolutionary trend of paleoshorelines in the Coastal Makran zone (southeast Iran) since the mid-Holocene. Quaternary International 392, 203–212. https://doi.org/10.1016/j.quaint.2015.06.030

Goetz, A.F.H., Rock, B.N., Rowan, L.C., 1983. Remote sensing for exploration; an overview. Economic Geology 78, 573–590. https://doi.org/10.2113/gsecongeo.78.4.573

Gorelick, N., Hancher, M., Dixon, M., Ilyushchenko, S., Thau, D., Moore, R., 2017. Google Earth Engine: Planetary-scale geospatial analysis for everyone. Remote Sensing of Environment 202, 18–27. https://doi.org/10.1016/j.rse.2017.06.031

Grando, G., McClay, K., 2007. Morphotectonics domains and structural styles in the Makran accretionary prism, offshore Iran. Sedimentary Geology 196, 157–179. https://doi.org/10.1016/j.sedgeo.2006.05.030

Hafkenscheid, E., Wortel, M.J.R., Spakman, W., 2006. Subduction history of the Tethyan region derived from seismic tomography and tectonic reconstructions. Journal of Geophysical Research: Solid Earth 111. https://doi.org/10.1029/2005JB003791

Haghipour, N., Burg, J.-P., 2014. Geomorphological analysis of the drainage system on the growing Makran accretionary wedge. Geomorphology 209, 111–132. https://doi.org/10.1016/j.geomorph.2013.11.030

Harms, J.C., Cappel, H.N., Francis, D.C., 1984. The Makran coast of Pakistan: its stratigraphy and hydrocarbon potential. Marine geology and oceanography of Arabian Sea and coastal Pakistan 3.

Hatzfeld, D., Molnar, P., 2010. Comparisons of the kinematics and deep structures of the Zagros and Himalaya and of the Iranian and Tibetan plateaus and geodynamic implications. Reviews of Geophysics 48, RG2005. https://doi.org/10.1029/2009RG000304

He, P., Wen, Y., Xu, C., Chen, Y., 2019. Complete three-dimensional near-field surface displacements from imaging geodesy techniques applied to the 2016 Kumamoto earthquake. Remote Sensing of Environment 232, 111321. https://doi.org/10.1016/j.rse.2019.111321

Heidarzadeh, M., Pirooz, M.D., Zaker, N.H., Yalciner, A.C., Mokhtari, M., Esmaeily, A., 2008. Historical tsunami in the Makran subduction zone off the southern coasts of Iran and Pakistan and results of numerical modeling. Ocean Engineering 35, 774–786. https://doi.org/10.1016/j.oceaneng.2008.01.017

Jackson, J., McKenzie, D., 1984. Active tectonics of the Alpine-Himalayan Belt between western Turkey and Pakistan. Geophysical Journal International 77, 185–264. https://doi.org/10.1111/j.1365-246X.1984.tb01931.x

Jacob, K.H., Quitmeyer, R., Farah, A., DeJong, K.A., 1979. The Makran region of Pakistan and Iran: trench-arc system with active plate subduction. Quittmeyer, Richard Charles 73.

Jensen, J.R., 2016. Introductory digital image processing: a remote sensing perspective, 4th ed, Pearson series in geographic information science. Pearson Education, Glenview, Ill.

Jordan, M.I., Mitchell, T.M., 2015. Machine learning: Trends, perspectives, and prospects. Science 349, 255–260. https://doi.org/10.1126/science.aaa8415

Kaveh-Firouz, A., Mohammadi, A., Görüm, T., Sarıkaya, M.A., Alizadeh, H., Akbaş, A., Mirarabi, A., 2023. Main drivers of drainage pattern development in onshore Makran Accretionary Wedge, SE Iran. International Journal of Earth Sciences 112, 539–559. https://doi.org/10.1007/s00531-022-02270-6

Kelleher, J.D., Tierney, B., 2018. Data science, The MIT Press essential knowledge series. The MIT Press, Cambridge, Massachusetts.

Kent, R.G., 1953. Old Persian: Grammar, Texts, Lexicon. American Oriental Society, New Haven.

Khan, M.A., Raza, H.A., Alam, S., 1991. Petroleum geology of the Makran region: implications for hydrocarbon occurrence in cool basins. Journal of Petroleum Geology 14, 5–18. https://doi.org/10.1111/j.1747-5457.1991.tb00295.x

Khorrami, F., Vernant, P., Masson, F., Nilfouroushan, F., Mousavi, Z., Nankali, H., Saadat, S.A., Walpersdorf, A., Hosseini, S., Tavakoli, P., Aghamohammadi, A., Alijanzade, M., 2019. An up-to-date crustal deformation map of Iran using integrated campaign-mode and permanent GPS velocities. Geophysical Journal International 217, 832–843. https://doi.org/10.1093/gji/ggz045

Kopf, A.J., 2002. SIGNIFICANCE OF MUD VOLCANISM. Reviews of Geophysics 40. https://doi.org/10.1029/2000RG000093

Kopp, C., Fruehn, J., Flueh, E.R., Reichert, C., Kukowski, N., Bialas, J., Klaeschen, D., 2000. Structure of the Makran subduction zone from wide-angle and reflection seismic data. Tectonophysics 329, 171–191. https://doi.org/10.1016/S0040-1951(00)00195-5

Krizhevsky, A., Sutskever, I., Hinton, G.E., 2017. ImageNet classification with deep convolutional neural networks. Commun. ACM 60, 84–90. https://doi.org/10.1145/3065386

Kukowski, N., Lallemand, S.E., Malavieille, J., Gutscher, M.-A., Reston, T.J., 2002. Mechanical decoupling and basal duplex formation observed in sandbox experiments with application to the Western Mediterranean Ridge accretionary complex. Marine Geology 186, 29–42. https://doi.org/10.1016/S0025-3227(02)00171-8

Lambeck, K., 1996. Shoreline reconstructions for the Persian Gulf since the last glacial maximum. Earth and Planetary Science Letters 142, 43–57. https://doi.org/10.1016/0012-821X(96)00069-6

LeCun, Y., Bengio, Y., Hinton, G., 2015. Deep learning. Nature 521, 436–444. https://doi.org/10.1038/nature14539

LeCun, Y., Bottou, L., Bengio, Y., Haffner, P., 1998. Gradient-based learning applied to document recognition. Proceedings of the IEEE 86, 2278–2324. https://doi.org/10.1109/5.726791

Liaw, A., Wiener, M., 2002. Classification and regression by randomForest. R news 2/3.

Lillesand, T.M., Kiefer, R.W., Chipman, J.W., 2015. Remote sensing and image interpretation, 7th ed. John Wiley & Sons, Inc, Hoboken, N.J.

Lu, D., Weng, Q., 2007. A survey of image classification methods and techniques for improving classification performance. International Journal of Remote Sensing 28, 823–870. https://doi.org/10.1080/01431160600746456

Mayrhofer, M., 1978. Handbuch des Altpersischen. Wiesbaden: Harrassowitz.

McCall, G.J.H., 1985. Area report, East Iran Project-Area No: 1 (North Makran & South Baluchestan) (No. Report No.57). Geological Survey of Iran, Tehran.

McCall, G.J.H., 1983. Mélanges of the Makran, southeastern Iran. Hutchinson Ross Publishing Company, Ophiolitic and related mélanges 66, 292–299.

McCall, G.J.H., Kidd, R.G.W., 1982. The Makran, Southeastern Iran: the anatomy of a convergent plate margin active from Cretaceous to Present. Geological Society, London, Special Publications 10, 387–397. https://doi.org/10.1144/GSL.SP.1982.010.01.26

McClay, K.R., 1992. Thrust tectonics. Champan & Hall, London New York Tokyo [etc.].

Molnar, P., Stock, J.M., 2009. Slowing of India's convergence with Eurasia since 20 Ma and its implications for Tibetan mantle dynamics. Tectonics 28, 2008TC002271. https://doi.org/10.1029/2008TC002271

Nazari, H., 2024. The Server based unified thematic Geological mapping,. Presented at the GEOKURDISTAN VI, 5-7 November 2024, Sulaimani, Kurdistan Region, Iraq.

Nazari, H., Karami, J., Arefipour, S., 2024a. SUTGM PROGRAMME: A New Protocol for Server-Based Unified Thematic Geological Mapping (GeoNexus), UCCGHA 027. UNESCO Chair on Coastal Geo-Hazards Analysis.

Nazari, H., Karami, J., Arefipour, S., 2024b. Geological Mapping in the Era of AI: Leveraging Innovation for Precision and Speed. Presented at the Mediterranean Geoscience Union (MedGU), 25-28 Nov. 2024, Barcelona, Spain.

Nazari, H., Karami, J., Arefipour, S., 2023a. The Server based unified thematic Geological mapping in cloud computing, approach: Deep Machin Learning. Presented at the Regional symposium on Geospatial Information Exchange and Research (GIER), 07-08 March, Muscat, Oman.

Nazari, H., Karami, J., Arefipour, S., 2022. The Server based unified thematic Geological mapping in cloud computing,. Presented at the AAPG Europe Regional Conference: Revitalizing Old Fields and Energy Transition in Mature Basins, 3-4 May 2022, Budapest, Hungary.

Nazari, H., Karami, J., Arefipour, S., Aghaali, E., 2023b. Using artificial intelligence and Machine learning in the mapping of quaternary units. Quaternary of Iran 8, 379–403.

Normand, R., 2019. Geomorphological, sedimentological and structural signals of deformation in a silent subduction zone: an investigation of the Makran (Iran). Université de Genève. https://doi.org/10.13097/ARCHIVE-OUVERTE/UNIGE:117482

Page, W.D., Alt, J.N., Cluff, L.S., Plafker, G., 1979. Evidence for the recurrence of large-magnitude earthquakes along the Makran coast of Iran and Pakistan. Tectonophysics 52, 533–547. https://doi.org/10.1016/0040-1951(79)90269-5

Paul, J., Bürgmann, R., Gaur, V.K., Bilham, R., Larson, K.M., Ananda, M.B., Jade, S., Mukal, M., Anupama, T.S., Satyal, G., Kumar, D., 2001. The motion and active deformation of India. Geophysical Research Letters 28, 647–650. https://doi.org/10.1029/2000GL011832

Platt, J.P., Leggett, J.K., Young, J., Raza, H., Alam, S., 1985. Large-scale sediment underplating in the Makran accretionary prism, southwest Pakistan. Geol 13, 507. https://doi.org/10.1130/0091-7613(1985)13<507:LSUITM>2.0.CO;2

Powell, C.McA., 1979. A morphological classification of rock cleavage. Tectonophysics 58, 21–34. https://doi.org/10.1016/0040-1951(79)90320-2

Quittmeyer, R.C., Kafka, A.L., Armbruster, J.G., 1984. Focal mechanisms and depths of earthquakes in central Pakistan: A tectonic interpretation. Journal of Geophysical Research: Solid Earth 89, 2459–2470. https://doi.org/10.1029/JB089iB04p02459

Richards, J.A., 2013. Remote Sensing Digital Image Analysis: An Introduction, 5th ed. Springer, Berlin.

Sabins, F.F.J., Ellis, J.M., 2020. Remote sensing: Principles, Interpretation, and Applications, 4th ed. Waveland Press, Inc, Long Grove (Illinois).

Schmidhuber, J., 2015. Deep learning in neural networks: An overview. Neural Networks 61, 85–117. https://doi.org/10.1016/j.neunet.2014.09.003

Schmitt, R., 1991. The Bisitun Inscriptions of Darius the Great: Old Persian Text, Corpus Inscriptionum Iranicarum I, 1, Texts I. London.

Shah-Hosseini, M., Ghanavati, E., Morhange, C., Naderi Beni, A., Lahijani, H.A., Hamzeh, M.A., 2018. The evolution of Chabahar beach ridge system in SE Iran in response to Holocene relative sea level changes. Geomorphology 318, 139–147. https://doi.org/10.1016/j.geomorph.2018.06.009

Simonyan, K., Zisserman, A., 2014. Very Deep Convolutional Networks for Large-Scale Image Recognition. https://doi.org/10.48550/ARXIV.1409.1556

Smith, G., McNeill, L., Henstock, T.J., Bull, J., 2012. The structure and fault activity of the Makran accretionary prism. Journal of Geophysical Research: Solid Earth 117. https://doi.org/10.1029/2012JB009312

Snead, R.J., 1993. Uplifted marine terraces along the Makran coast of Pakistan and Iran, in: Himalaya to the Sea. Routledge, London, pp. 327–362.

Stöcklin, J., 1968. Structural history and tectonics of Iran: a review. American Association of Petroleum Geologists Bulletin 52, 1229–1258.

Stoneley, R., 1974. Evolution of the Continental Margins Bounding a Former Southern Tethys. The Geology of Continental Margins.

Sutskever, I., Vinyals, O., Le, Q.V., 2014. Sequence to Sequence Learning with Neural Networks. https://doi.org/10.48550/ARXIV.1409.3215

Vernant, Ph., Nilforoushan, F., Hatzfeld, D., Abbassi, M.R., Vigny, C., Masson, F., Nankali, H., Martinod, J., Ashtiani, A., Bayer, R., Tavakoli, F., Chéry, J., 2004. Present-day crustal deformation and plate kinematics in the Middle East constrained by GPS measurements in Iran and northern Oman. Geophysical Journal International 157, 381–398. https://doi.org/10.1111/j.1365-246X.2004.02222.x

Vita-Finzi, C., 1987. ^{14}C deformation chronologies in coastal Iran, Greece and Jordan. JGS 144, 553–560. https://doi.org/10.1144/gsjgs.144.4.0553

Vita-Finzi, C., 1979. Contributions to the Quaternary geology of southern Iran. Geological and Mineral Survey of Iran 47, 30–47.

Von Rad, U., Berner, U., Delisle, G., Doose-Rolinski, H., Fechner, N., Linke, P., Lückge, A., Roeser, H.A., Schmaljohann, R., Wiedicke, M., Parties, S. 122/130 S., Block, M., Damm, V., Erbacher, J., Fritsch, J., Harazim, B., Poggenburg, J., Scheeder, G., Schreckenberger, B., Von Mirbach, N., Drews, M., Walter, S., Ali Khan, A., Inam, A., Tahir, M., Tabrez, A.R., Cheema, A.H., Pervaz, M., Ashraf, M., 2000. Gas and fluid venting at the Makran accretionary wedge off Pakistan. Geo-Marine Letters 20, 10–19. https://doi.org/10.1007/s003670000033

White, R.S., Klitgord, K., 1976. Sediment deformation and plate tectonics in the Gulf of Oman. Earth and Planetary Science Letters 32, 199–209. https://doi.org/10.1016/0012-821X(76)90059-5

White, R.S., Louden, K.E., 1982. The Makran continental margin: structure of a thickly sedimented convergent plate boundary: convergent margins: field investigations of margin structure and stratigraphy. AAPG, Studies in Continental Margin Geology 499–518.

Zhou, Z.-H., 2012. Ensemble methods: foundations and algorithms, Online-Ausg. ed, Chapman & Hall. Taylor & Francis, Boca Raton, FL.

Abstract

This report presents the findings of the Server-Based Unified Thematic Geological Mapping of Makran (SUTGMM) project, a groundbreaking geospatial study conducted at a 1:50,000 scale in southeastern Iran. The Makran region, positioned along the northern margin of the Oman Sea, is a key geological area shaped by the complex collision of the Arabian and Eurasian plates. The project offers a detailed analysis of the region's diverse geological formations, including volcanic sequences, sedimentary basins, and Quaternary deposits, which reveal the area's dynamic geologic history. Utilizing state-of-the-art technologies such as cloud computing, machine learning, and object-based image analysis (OBIA), the SUTGMM project integrates data from Sentinel-1, Sentinel-2, Landsat-8, and ASTER, alongside digital elevation models (DEMs). Processed via *Google Earth Engine*, this innovative approach enabled the production of a unified geological map with 85% accuracy, providing new insights into the region's stratigraphy and tectonic processes. The final output includes geological maps, covering key areas of Makran, supported by the GeoNexus geodatabase. This geodatabase consolidates multi-source data, field surveys, and advanced algorithms to produce highly detailed and accurate geological interpretations. The GeoNexus/SUTGMM project represents a cost reduction of 80% compared to traditional methods and achieves a more than 90% reduction in time and personnel, making it a highly efficient and cost-effective, yet precise and comprehensive solution for large-scale geological mapping. The SUTGMM project represents a significant advancement in cost-effective geological mapping, reducing both time and resources traditionally required for such large-scale studies, while improving precision and comprehensiveness.

Abstract

The Server-Based Unified Thematic Geological Mapping of Makran (SUTGMM) is a comprehensive geospatial study conducted at a scale of 1:50,000, focusing on the Makran region, located in southeastern Iran along the northern margin of the Oman Sea. This region is characterized by diverse geological formations resulting from the collision of the Arabian and Eurasian plates, including volcanic and sedimentary sequences, turbidite basins, and Quaternary deposits. Makran's rich geological heritage, coupled with its historical importance, makes it a prime subject for advanced geoscientific research and mapping.

Utilizing a novel approach combining cloud computing, machine learning, and object-based image analysis, the project leverages the power of Google Earth Engine for the processing and analysis of large datasets. The random forest algorithm, used for geological classification, has enabled the creation of a unified geological map with an accuracy of 85%, highlighting the effectiveness of this integrated approach.

This project has provided valuable insights into the complex geological context of the Makran region. The geological units mapped in SUTGMM represent a time range from the Oligocene to the Quaternary period. This includes older formations from the Oligocene and Miocene, as well as more recent Pleistocene and Quaternary deposits. The units highlight the region's complex geodynamic evolution, influenced by both tectonic activity and sedimentary processes.

The GeoNexus geodatabase, as the final product of the SUTGMM project, represents a major advancement in geological mapping by using cloud computing, machine learning, field surveys, and multi-source data integration to enhance the accuracy, efficiency, and comprehensiveness of geological outputs. Ultimately, the findings from this study are expected to support sustainable development efforts and foster a deeper understanding of the Makran region's geodynamic processes.

ISBN : 978-622-8423-35-7

9 786228 423357

2025